Dissertation
submitted to the
Combined Faculties for the Natural Sciences and for Mathematics
of the Ruperto-Carola-University of Heidelberg, Germany
for the degree of
Doctor of Natural Sciences

presented by
M.Sc Physics Marie-Hélène Nicol
born in Chambly,Québec,Canada
Oral examination: May 12th 2009

Investigation of the stellar population in galaxies since z=2 by NIR photometry

Referees:Dr. Prof. Klaus Meisenheimer

Dr. Prof. Burkhard Fuchs

Untersuchung der Sternpopulation in Galaxien seit z = 2 mittels Nahinfrarotphotometrie

Diese Studie untersucht die Galaxienevolution innerhalb der letzten 10 Milliarden Jahre. Um Zugang zum Universum bei hohen Rotverschiebungen zu erhalten, wurden Nahinfrarotbeobachtungen im Rahmen der Himmelsdurchmusterung COMBO-17+4 (Classifying Objects by Medium-Band Observations) durchgeführt. Photometrische Rotverschiebungen, Ruheband-Spektralverteilungen und Massen wurden für 14286 Galaxien bis zu einer scheinbaren Helligkeit von $H = 21.7^{mag}$ in 0.2 Quadratgrad des A901-Feldes bestimmt. Die rote, entwickelte sowie die blaue, sternbildende Galaxienpopulation wurden in Abhängigkeit von der Zeit untersucht. Hierzu wurde eine sich als Funktion der Zeit entwickelnde Farben-Helligkeits-Beziehung abgeleitet, um die rote Galaxienpopulation von der blauen zu trennen. Unsere Ergebnisse zeigen, dass die bimodale Verteilung der Galaxien bis hinaus zu $z = 1.6$ besteht. Weiterhin wurden die Helligkeits- und Massenfunktion beider Populationen untersucht. Hier zeigt sich, dass sich die charakteristische Magnitude M^* in beiden Fällen zwischen $2 > z > 0.2$ signifikant abschwächt. Das schwere Ende der Massenfunktion wird für z<1 von roten Galaxien dominiert, während bei hohen z entwickelte, rote und sternbildende blaue Galaxien zu gleichen Teilen beitragen.

Investigation of the stellar population in galaxies since z=2 by NIR photometry

This study investigates galaxy evolution in the last 10 Gyr of the age of the Universe. To access the high redshift Universe deep near infrared observations have been carried out in the frame of the COMBO-17+4 (Classifying Objects by Medium-Band Observations) survey. Photometric redshifts, rest-frame SEDs and masses have been obtained for 14286 galaxies down to an observed magnitude $H = 21.7^{mag}$ in 0.2 square degree of the A901-field. The red evolved and the blue star-forming galaxy populations distributions have been followed through cosmic time. An evolving colour-magnitude relation as a function of lookback time has been derived in order to separate the red galaxies from the blue ones. Our results show that the galaxy bimodality persist out to $z = 1.6$. The luminosity and the mass function for the red and the blue galaxy populations has been investigated. Our results show that the characteristic magnitude M^* for both galaxy population have considerably dimmed between $2 > z > 0.2$. The massive end of the mass function is dominated by the red galaxies at $z < 1$, whereas above $z = 1$ red evolved and blue star-forming galaxy populations contribute in similar numbers.

Contents

Abstract iv

Table of Contents v

List of Acronyms x

1 Introduction 1
- 1.1 Cosmological Context . . . 1
- 1.2 Galaxies in the Local Universe . . . 2
- 1.3 Lookback Time Surveys . . . 2
- 1.4 Photometric Redshift as a Tool to Study Galaxy Evolution . . . 4
- 1.5 Observation of Galaxy Evolution in the ΛCDM Universe . . . 6
- 1.6 This Study . . . 9

2 The COMBO-17+4 Survey 10
- 2.1 The Limitations of the COMBO-17 Survey . . . 10
- 2.2 Survey Description . . . 11
- 2.3 The Scientific Goals of the Survey . . . 12
- 2.4 Survey Status . . . 12
- 2.5 The Super Cluster Abell 901/902 to Probe Galaxy Evolution . . . 12
- 2.6 Ongoing Ground Based Infrared Surveys . . . 13

3 From Photons to Photometry 15
- 3.1 The Atmosphere in Near Infrared . . . 15
- 3.2 The Omega2k Camera . . . 16
- 3.3 Observational Strategy . . . 17
- 3.4 NIR Observations . . . 19
- 3.5 Data Reduction Scheme . . . 21
- 3.6 Dark Current Correction . . . 22
- 3.7 Flatfield Correction . . . 22
- 3.8 Stray Light Correction . . . 24

3.9 Sky Determination and Subtraction . . . 26
3.9.1 Quadrant Structure Correction . . . 28
3.10 Build a Bad Pixel Mask . . . 29
3.11 Cosmic Rays and Bad Pixels Correction . . . 32
3.12 Frame Summation . . . 34
3.13 Deep H-band Catalogue . . . 34
3.14 Gnomonic Projection . . . 35
3.15 Photometry . . . 35
3.16 Calibration Between Different Wavebands . . . 38
3.17 Magnitude Limit . . . 38
3.18 Colour Calibration with Main Sequence Stars . . . 39
3.19 Astrometry . . . 40

4 Classification by SED Templates Fitting 45
4.1 Colour Indices . . . 45
4.2 The Classification Scheme . . . 46
4.3 Colour Libraries . . . 47
4.3.1 Star Libraries . . . 47
4.3.2 Galaxy Spectral Library . . . 48
4.3.3 QSO Library . . . 48
4.4 Classification Results . . . 49
4.4.1 Comparison of the COMBO-17 Catalogue with the COMBO-17+4 Catalogue . . . 50
4.5 Low Flux Count and Redshift Focusing . . . 52
4.6 Improving Photometric Redshift with NIR Data . . . 53

5 Galaxy Bimodality Through Cosmic Time 60
5.1 Rest-Frame Magnitudes and Colours . . . 60
5.2 Rest-frame Colour Bimodality . . . 64
5.3 Colour Magnitude Relation . . . 68
5.4 Colour-Magnitude Diagrams up to z=2 . . . 69

6 Evolution of the Luminosity Function 73
6.1 Definition of the Luminosity Function . . . 73
6.2 Luminosity Function Estimator . . . 74
6.3 Galaxy Sample Division . . . 75
6.4 Evolution of the Luminosity Function . . . 76

7 Evolution of the Mass Function 83
7.1 Mass Determination 83
7.2 Colour-Mass Diagrams up to z=2 84
7.3 Evolution of the Mass Function 85
7.4 Massive Distant Galaxies 88
7.5 The Most Massive Distant Galaxy 90

Appendix A 1

A Standard Stars SED 1

Appendix B 1

B Photometry Setup File 5

Bibliography 5

List of Acronyms

Acronym	Definition
2dF	Two Degree Field system Galaxy Survey
ACS	Advanced Camera for Surveys
AEGIS	All-wavelength Extended Groth Strip International Survey
ALHAMBRA	Advanced Large, Homogeneous Area Medium Band Redshift Astronomical Survey
CADIS	Calar Alto Deep Imaging Survey
COMBO-17	Classifying Objects by Medium-Band Observations in 17 filters
COSMOS	Cosmological evolution Survey
CDFS	Chandra Deep Field-South
DEEP2	DEEP2 Redshift Survey
ESO	European Southern Observatory
FORS	CfA Redshift Survey
GOODS	Great Observatories Origins Deep Survey
HIROCS	Heidelberg InfraRed Optical Cluster Survey
HST	Hubble Space Telescope
MANOS	PI für Astronomie Near-infrared Optical Surveys
MPG	Max-Planck-Gesellschaft
MUSYC	Multiwavelength Survey by Yale-Chile
NEWFIRM	NEWFIRM Medium-Band Survey
SGP	South Galactic Pole
SDSS	Sloan Digital Sky Survey
UKIDSS	UK Infrared Deep Sky Survey
VIMOS	VIsible MultiObject Spectrograp
VLT	Very Large Telescope
VVDS	VIMOS VLT Deep Survey
WFI	Wide Field Imager

No observational problem
will not be solved by more data

Vera Rubin

Chapter 1

Introduction

Galaxies are the building blocks of our Universe. Understanding when and how galaxies were formed and how they have evolved since the Big Bang is one of the main motivations of contemporary astronomy. The astrophysical studies on galaxy formation and evolution attempt to describe the physical processes which have transformed the primordial homogeneous Universe to the current heterogeneous Universe which contains clustered structures and a large variety of galaxy types.

1.1 Cosmological Context

The most accepted cosmological model to describe our Universe is the Lambda Cold Dark Matter (ΛCDM) model. This model gives a fairly accurate picture of the observable Universe by connecting the Big Bang theory, the inflation and the accelerated expansion of our Universe as well as the structures growth by hierarchical clustering. The ΛCDM model describes the large scale structures of our Universe as a sponge structure with filaments, walls and voids. The millennium simulation by Springel et al. (2005), see Fig. 1.1, gives a good picture of the distribution of the large scale dark matter structures in the ΛCDM context. The last results by WMAP (Hinshaw et al. 2008) show that the present Universe is 13.72 Gyr old and composed of 72.6% of dark energy (vacuum energy from the field), 22.8% of dark matter (non-baryonic invisible matter which interacts only gravitationally, whose nature is still a puzzle for scientists) and only 4.6% is in a form of baryonic matter, like galaxies, stars, gas and dust. In the ΛCDM model, galaxies form at the bottom of dark matter potential wells in dark matter filaments. At the junction of the filaments lie massive galaxy clusters. In this cosmological model, merging and clustering are the main mechanisms with which galaxies gain mass. In a hierarchical way, small structures merge and cluster to form bigger structures. In the meantime, galaxy internal structures evolve from, for example, disk-like spiral galaxies to a giant elliptical galaxy.

1.2 Galaxies in the Local Universe

The present Universe is composed of galaxies with various morphologies (as described by the Hubble sequence, see Fig. 1.1) and various masses, sizes and properties. Galaxies morphological types can be separated into two main distinct sets. On one hand, the bulge-like elliptical galaxies, also called early type galaxies, and on the other hand the disk-like, spiral galaxies also called late type galaxies. These two sets of galaxies not only show a fundamental difference in terms of morphology but also in terms of observable colours. Galaxies are formed by a complex mix of young and old stellar populations. Old evolved or younger but dusty galaxies appear redder than young star-forming galaxies which appear bluer.

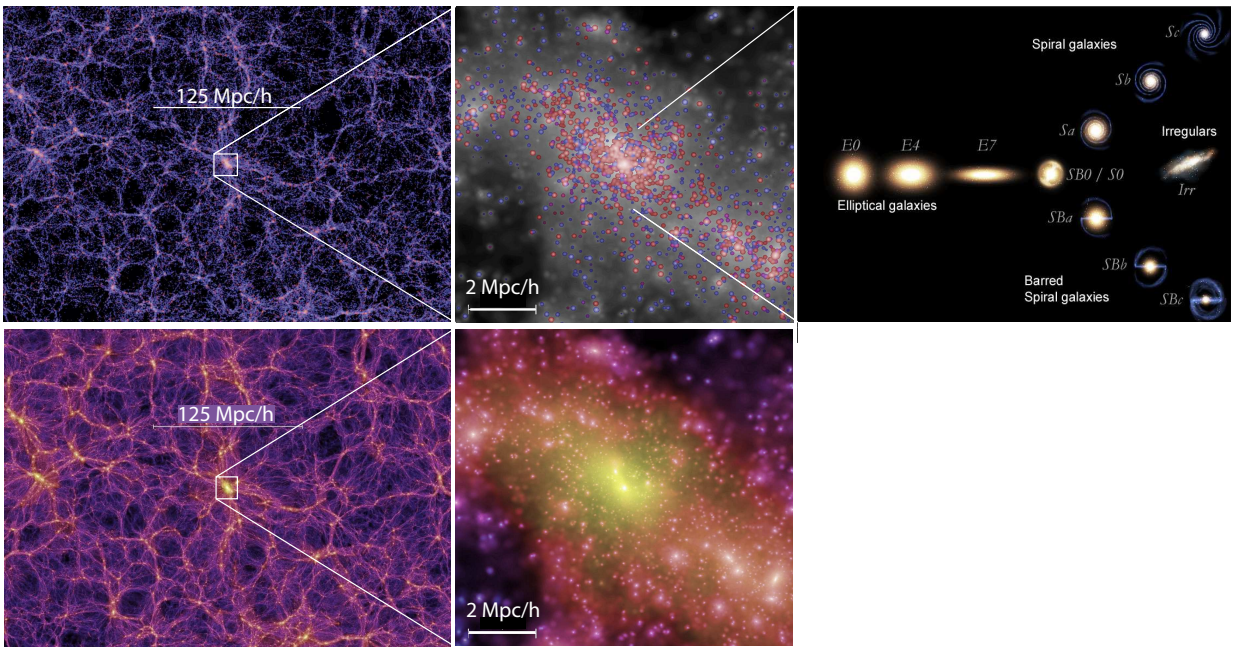

Figure 1.1: Large scale structure at z=0 from the millennium simulation (Springel et al. 2005) and the Hubble Sequence (credit: Fahad Sulehria). Top left panel shows the large-scale light distribution, middle panel shows a rich cluster of galaxies where one can sees galaxies individually, right panel shows the diversity of galaxy types in the present Universe. Bottom row shows the corresponding dark matter distributions.

1.3 Lookback Time Surveys

The cosmological redshift is a redshift caused by the expansion of the Universe. The wavelength of light increases as it traverses the expanding Universe between its point of emission and its point of detection by the same amount that space has expanded during the crossing time; thus if λ_o and λ_e are the observed and emitted wavelengths respectively, we have

$$\frac{\lambda_o}{\lambda_e} = \frac{a_o}{a} = \frac{1}{a} \tag{1.1}$$

where a is the scale factor at the time of emission and a_o is its present value which is normalized to one. The redshift is the relative wavelength change,

$$z \equiv \frac{\lambda_o - \lambda_e}{\lambda_e} = \frac{1}{a} - 1 \tag{1.2}$$

and thus

$$1 + z = \frac{1}{a}, \quad a = \frac{1}{1+z} \tag{1.3}$$

The lookback time as defined by Eq. 1.4 is the time that light takes to travel from an emitting object to us. Since the velocity of the light is finite, when we observe a distant object, this object looks as it was at the time its light was emitted (i.e. when we look at a distant object we look "back in time"). The lookback time allows astronomers to study the evolution of galaxies, by looking at galaxies at different distances, we look at them at different epochs and it is thus possible to study the changes in galaxies with time. Figure 1.2 shows the lookback time and the luminosity distance (see Eq. 1.6) as a function of redshift for a cosmological model where $\Omega_m = 0.28$, $\Omega_\lambda = 0.73$ and H_0=71 km/s/Mpc.

$$t_{lookback} = \frac{1}{H_0} \int_0^z \frac{dz}{(1+z)\sqrt{\Omega_m(1+z)^3 + \Omega_k(1+z)^2 + \Omega_\Lambda}} \tag{1.4}$$

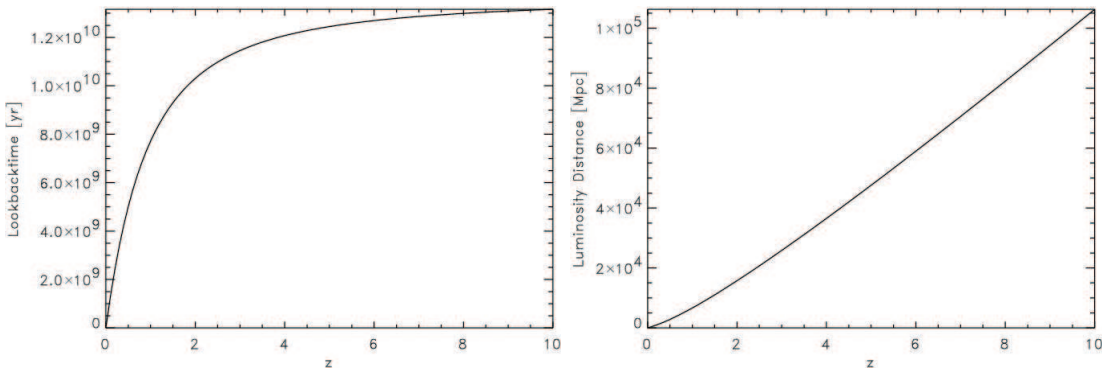

Figure 1.2: Left: Lookback time as a function of redshift. Right: Luminosity distance as a function of redshift. World model Ω_m, Ω_λ=(0.28,0.73) and H_0=71 km/s/Mpc is assumed.

In lookback time surveys we have to take into account that the galaxies spectra move through the observed bands due to their redshift. For high redshifted galaxies, for example, the optical rest-frame is shifted to the near infrared (NIR). Figure 1.3 shows an example of the position of the redshifted spectrum of an Elliptical galaxy with respect to some observed bands. In lookback surveys a k-correction has to be applied to study a galaxy in its rest-

frame. The absolute magnitude M of an object is defined as the apparent magnitude m that this object would have if it were at a distance of 10 parsec, taking into account the k-correction we have:

$$m = M + 5log\left(\frac{D_L}{10pc}\right) + K(z) \tag{1.5}$$

where the luminosity distance

$$D_L = (1+z)\frac{c}{H_0}\int_0^z \frac{dz}{\sqrt{\Omega_m(1+z)^3 + \Omega_k(1+z)^2 + \Omega_\Lambda}} \tag{1.6}$$

and K(z) is the k-correction which depends on the galaxy spectrum

$$K(z) = -2.5log\left[(1+z)\frac{L_{(1+z)\nu}}{L_\nu}\right] \tag{1.7}$$

In order to obtain a rest-frame magnitude a k-correction is applied because the redshifted object emits his light (L_ν) in a different pass bands that the one observed ($L_{(1+z)\nu}$). Combining Eq. 1.5 to Eq. 1.7 if the apparent magnitude and the redshift of an object is known from a photometric or spectroscopic survey, the luminosity distance and the k-correction can be calculated and its absolute magnitude derived. Knowing rest-frame properties for galaxies at different redshift allows us to see different snapshot in the galaxy evolution with time.

Lookback time surveys can study the galaxies into different redshift slice of the Universe. The comoving volume V_C is the measured volume in which the number density of non-evolving objects which are locked in the Hubble flow remains constant with redshift, see Hogg (1999) for a nice review on distance measures in cosmology. Assuming a flat Universe where Ω_K=0, the comoving volume is:

$$V_c = \frac{4\pi}{3}(D_c)^3 \tag{1.8}$$

where D_c is the comoving distance defined as:

$$D_c = \frac{c}{H_0}\int_0^z \frac{dz}{\sqrt{\Omega_m(1+z)^3 + \Omega_\Lambda}} \tag{1.9}$$

1.4 Photometric Redshift as a Tool to Study Galaxy Evolution

To study the galaxy evolution through cosmic time the determination of a galaxy's redshift becomes imperative and the redshift accuracy crucial. Photometric redshift using different colours to estimate the redshift of a galaxy is an economic way to obtain redshifts for a large amount of galaxies in a given field. Since spectroscopy is costly in terms of telescope time due to the optical faintness of distant galaxies, photometric redshift has in recent years become a

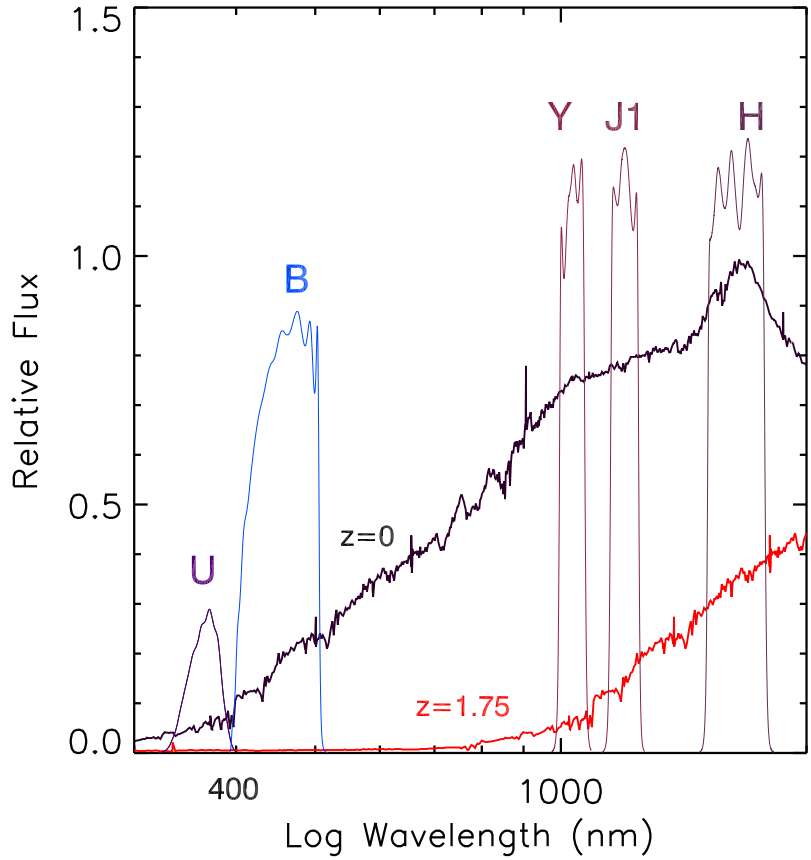

Figure 1.3: Spectrum of an elliptical galaxy at different redshifts. Because of the redshift, the spectrum moves through the different observed bands. At rest (in black) the 4000Å break feature is bracketed by the U- and the B-band while at z=1.75 (in red) it is bracketed by the Y- and the J1-band.

very useful tool for observational cosmology, providing the equivalent of low resolution spectra. The method to obtain photometric redshift consists of taking an image of a galaxy in different filters, performing the photometry, calculating the different colours and finally fitting the observed data points with a synthetic or an empirical Spectral Energy Distribution (SED). The spectral feature of the 4000Å break caused by calcium lines absorption is generally used to determine the redshift. The principle of photometric redshift seems simple but difficulties remain in how good the representation of the templates are to the observed galaxies and in the manner the fit between observed photometry and template is performed.

Based on the Calar Alto Deep Imaging Survey (CADIS) (Meisenheimer et al. 1998), an extragalactic key project of the MPIA in Heidelberg from 1994 to 1999, a robust classification method to distinguish objects between three different classes: galaxies, stars and quasars as

been established. Moreover, the CADIS experience demonstrated that classification and redshift estimation in surveys with medium-band filters are a powerful and accurate tool to study the evolution of galaxies and quasars through cosmic time (Wolf et al. 2001a,b). The main goal of CADIS was to study galaxy evolution through faint emission line galaxies at intermediate redshifts and primeval galaxies at very high redshift (Meisenheimer et al. 1998). CADIS included a deep emission line survey supplemented by a broad band multi-colour survey. This project lead to further projects like the COMBO-17 and the COMBO-17+4 survey which also use a combination of broad and narrow band photometry to perform the classification of objects and redshift determination. The advantage of this survey strategy is to be able to replace telescope time-consuming spectroscopy with multi-wavelength photometry as the main tool for classification and redshift measurements. It also provides accurate redshifts and multi-colour images for each galaxy useful for any further investigation on galaxy morphology.

1.5 Observation of Galaxy Evolution in the ΛCDM Universe

In the last few years, colour-magnitude diagrams, luminosity and mass functions were extensively used to describe the galaxies which populated the Universe (up to z∼1). In a colour-magnitude diagram, see Fig. 1.4, galaxies lie in two distinct populations defined as the galaxy bimodality. Some of them lie in a well defined narrow track called the red sequence while others lie in a more diffuse cloud, called the blue cloud. The red sequence galaxies are principally non star-forming galaxies, called passively evolving, massive galaxies, mainly elliptical galaxies (Bell et al. 2004a; Borch et al. 2006; Cassata et al. 2008) but could also contain obscure star forming dusty galaxies (Wolf et al. 2005). Inversely, the blue cloud is composed of star-forming, starburst, mainly low mass spiral galaxies. The red sequence and the blue cloud are separate by the green valley, an intermediate population of galaxies.

In the last 10 years, many galaxy imaging and spectroscopic surveys like COMBO-17 , SDSS, DEEP2, 2dF, VVDS, FORS, COSMOS, GOODS, UKIDSS[1], etc have probed the Universe and provided more clues on the physical processes which govern galaxy formation and evolution (since z∼1). Using COMBO-17 data, Bell et al. (2004b) have shown that the galaxy bimodality is present at all redshifts out to z=1 and that the red sequence is already in place at z=1. Bell et al. (2004b) also showed that the number density of luminous blue star forming galaxies has decreased strongly since z∼1 and that the stellar mass of the red sequence galaxy has doubled in the same redshift interval. Recent results by Borch et al. (2006) using also COMBO-17 data show that the integrated stellar mass density of blue galaxies stays constant since z∼1 but that the total stellar mass of the Universe has doubled in the same redshift interval. Moreover, in the same redshift interval the combined star formation rate (SFR) drops

[1]see list of acronyms at the beginning of this document for the meaning of the surveys names.

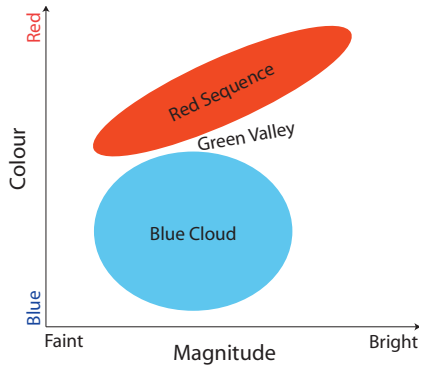

Figure 1.4: Mock colour-magnitude diagram showing the bimodality of galaxies. The red sequence follows a narrow track while the blue cloud lies in a more diffuse area of the diagram. The two populations are separated by the green valley.

by an order of magnitude since z=1 Madau et al. (1996); Lilly et al. (1996); Hippelein et al. (2003); Hopkins (2004), see also Fig. 1.5. The fact that the number of passively evolving galaxies are growing since z∼1 while the number of active star forming galaxies stays constant combined with a declining overall SFR leads to a better understanding of the galaxy evolution in the last 8 Gry. These observations suggest that the stellar mass of the massive elliptical galaxies present today was built up by recent major merges rather than by star formation and that physical mechanisms have shutdown the star formation around z=1.

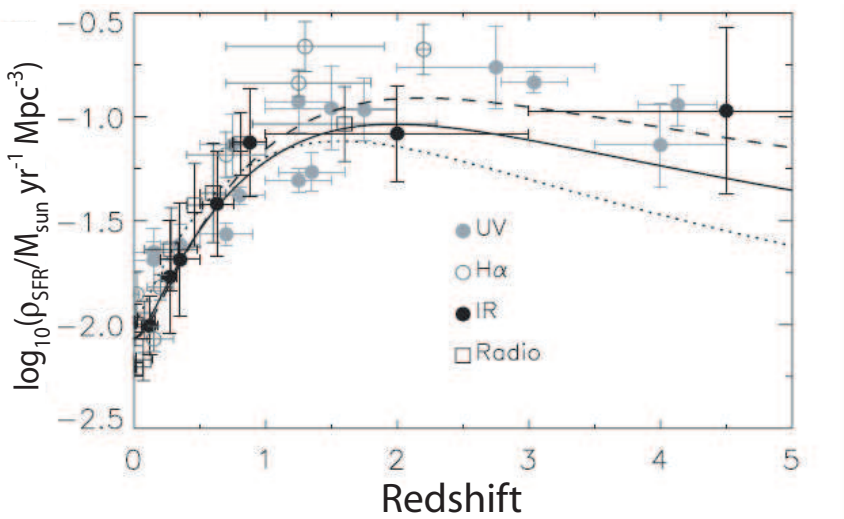

Figure 1.5: Evolution of the cosmic star formation rate using several data set from Borch et al. (2006). The SFR has a plateau at high redshift and severely declines from z∼1 to the present day.

Combining COMBO-17 and DEEP2 data, Faber et al. (2007) shows that since z=1 the buildup of the stellar mass on the red sequence comes from the combination of 1) the migration from the blue cloud galaxies for which the star formation has been quenched and 2) the merging of less luminous, quenched red galaxies. Figure 1.6 shows the buildup of the red sequence from a combination of quenching via wet merge followed by red galaxy dry merging. When the quenching happens through a wet merge of low mass blue galaxies (i.e. the mass is assembled in the blue cloud), the resulting product will populate the lower mass part of the red sequence and then can slowly increase its mass via dry merge on the red sequence. On the other hand, if the quenching happens later with more massive blue galaxies, the resulting product will have already assembled most of its mass in the blue cloud and will populate the massive part of the red sequence. The exact mechanisms which could have shutdown the star formation around z=1, such as quenching, harassment, strangulation, feedback, etc via galaxy dry or wet merge are still a matter of debate and a hot topic in astrophysics.

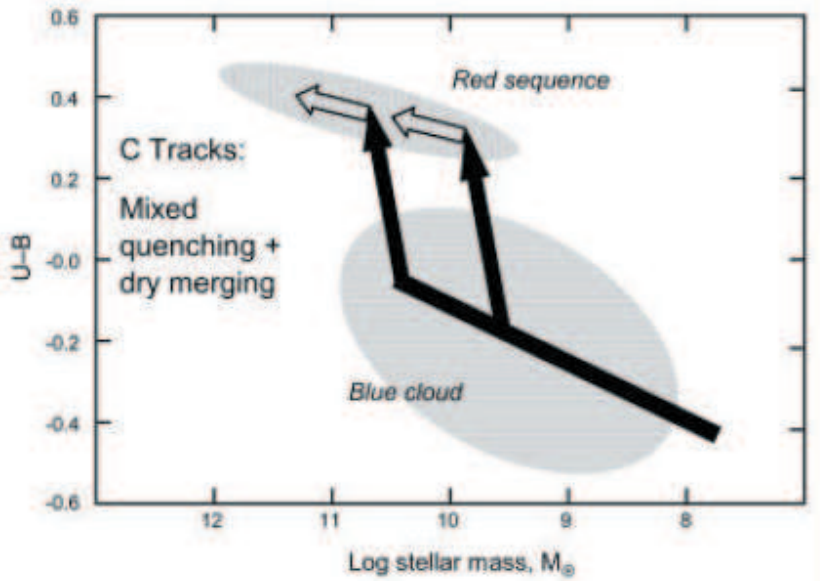

Figure 1.6: Schema of galaxy migration from blue cloud to the red sequence in a colour-mass diagram. The blue cloud galaxies undergo star formation quenching via wet merge and migrate to the red sequence (black arrows). Galaxies on the red sequence could undergo dry merging and hence increase their masses (white arrows), from Faber et al. (2007).

To date, most of the galaxy surveys are limited to describing the Universe below z$\sim$1 due to the difficulty of obtaining a large amount of high redshift galaxy spectra and the use of optical data only in the photometric redshift surveys, and little is known beyond z$\sim$1. It is thought that most of the stars in the Universe were formed between 1<z<3. If we look at the star formation rate (SFR) as a function of redshift in Fig. 1.5 one sees that the SFR modestly

increases between 5<z<3 reaches a peak at z∼2 and suddenly declines since z∼1. In light of these results, the Universe has produced most of its stars between 1<z<3 with an apogee at z∼2 followed by a drastic decline since z∼1. The epoch of the Universe between 1<z<2 is a crucial moment in terms of galaxy formation and evolution, it seems to be a period of transition. Motivating questions are when the red sequence was first formed and how its mass was assembled. If there is no doubt about the bimodality of galaxies below z∼1, things are less clear at higher redshift. Massive, passively evolving galaxies have been observed at z<1.5 (Daddi et al. 2005; Cirasuolo et al. 2007; McGrath et al. 2007; Taylor et al. 2008) and a recent spectroscopic study by Kriek et al. (2008) has confirmed the presence of a red sequence a little beyond z=2, observations also supported by the photometric survey by Williams et al. (2008). The problems encountered by the latest surveys like the low number of objects found at high redshift, the small area surveyed combined with the influence of large scale structures and the selection biases make difficult a rigorous analysis of galaxy evolution at high redshift. When the red sequence first appears is a matter of debate and one of the aims of this thesis.

1.6 This Study

The goal of this thesis is to resume the previous work achieved by the COMBO-17 team by extending the photometric redshift range out to z=2 with the help of deep NIR data to explore galaxy evolution at higher redshift. One of the main contributions of this thesis is to provide high quality NIR photometry and a deep H-band selected sources catalogue for the A901 field. By supplementing NIR to the optical data this work also improves the photometric redshift accuracy for z∼1 galaxies. An investigation of the bimodality of galaxies through cosmic time is done in order to separate the red and the blue populations of galaxy and derive the luminosity and mass function for red and blue galaxies out to z=2.

This thesis is organized as follows: Chapter 2 describes the COMBO-17+4 surveys and his goals. Chapter 3 presents the NIR data and the data reduction procedure and analysis. Chapter 4 deals with the classification of the galaxies and redshift assignment by template fitting. Chapter 5 investigates the galaxy bimodality through cosmic time. Chapter 6 presents the evolution of the luminosity function for the red and the blue galaxies since z=2. Chapter 7 presents the evolution of the mass function for the red and the blue galaxies since z=2. Finally Chapter 8 concludes this study.

Chapter 2

The COMBO-17+4 Survey

This chapter describes the COMBO-17+4 survey, its scientific goals and its context among other ongoing similar NIR surveys. To access information about physical properties of galaxies at high redshift, one needs IR observations since a galaxy's rest-frame optical light is stretched by the expansion of the Universe and shifted in the observed infrared wavelength range. Thus, the IR observations allow us to probe the optical rest-frame luminosity of distant galaxies and their stellar masses. The development of the infrared detectors and wide-field cameras allowed astronomers to further explore the Universe by probing faint and high redshifted sources, impossible to observe in the optical wavelength range.

The wide-field NIR camera OMEGA2k (PI: H-J. Röser), which started to be in operation at the Calar Alto Observatory in 2003, gave us the opportunity to obtain deep NIR images of a large amount of galaxies. The OMEGA2k camera was the largest ground based NIR camera available in the world for many years. At the same time the MANOS project (MPI für Astronomie Near-infrared Optical Surveys) was designed. MANOS is divided into a deep and a wide survey. COMBO-17+4 (Classifying Objects by Medium-Band Observations in 17 filters) consists of a deep NIR extension of the optical COMBO-17 survey to probe galaxy formation and evolution and HIROCS (Heidelberg InfraRed Optical Cluster Survey) consists of a wide NIR survey searching for high redshift galaxy clusters. Those two survey are key ongoing projects at the MPIA Heidelberg.

2.1 The Limitations of the COMBO-17 Survey

Although the COMBO-17 survey could provide a very good picture of the galaxy evolution, the survey is constrained to explore the Universe up to z=1 only. The redshift range of the COMBO-17 survey is limited by two facts:

• First the classification is not reliable above z∼1.1. The classification method uses the pronounced spectral feature from the 4000Å break to assign the redshift of a galaxy. The COMBO-17 survey is based on optical data only and the multi-colour classification method requires at least 2 photometric data points above the 4000Å break for a reliable redshift determination. The second reddest filter used in the frame of the COMBO-17 survey is the medium band λ=856nm, if we sample just above the 4000Å break, say 4100Å, this leads to a maximum reliable redshift of z= $\lambda_{observed}/\lambda_{emitted} = 856/410 - 1$=1.09.

• Secondly, the galaxies at z>1 which contain a considerable amount of old stars are too faint to be observed in the optical pass bands but their flux is substantial in the NIR.

2.2 Survey Description

COMBO-17+4 is a deep NIR survey which combines the 17 optical broad and medium bands from the COMBO-17 with 4 NIR filters (thus the name of the survey: COMBO-17+4). The optical images were taken with the Wide Field Imager (WFI) at La Silla Observatory between February 1999 and January 2001 in the frame of the COMBO-17 survey (Wolf et al. 2003). The NIR survey consists of observation in 3 medium bands Y($\lambda/\delta\lambda = 1034/80nm$), J1($\lambda/\delta\lambda = 1190/130nm$), J2($\lambda/\delta\lambda = 1320/130nm$) and one broad band H($\lambda/\delta\lambda = 1650/300nm$), see Fig. 3.5 for the full COMBO-17+4 filter set. The supplement of 4 NIR filters to the COMBO-17 survey allows to reach galaxies with reliable redshift out to z=2.1. The NIR data were carried out with the wide field IR camera Omega2000 attached to the 3.5m telescope at the Calar Alto Observatory in Spain. Three original targets from the COMBO-17 survey are observed in NIR: Abell 901, Abell 226 and S11, see Table 2.1 for the coordinates. Since the Calar Alto Observatory is located in the northern hemisphere the two other original targets of the COMBO-17 survey, the two southern field: SGP and CDFS, have been excluded from the COMBO-17+4 survey due to their low declination on the sky. Each field has a dimension of $30' \times 30'$ thus the total coverage of COMBO-17+4 survey is an area of 0.77 square degree on the sky (about 4 time the size of the moon).

Field Name	Right Ascension (J2000)	Declination (J2000)
A901	$09^h56^m17^s$	$-10^\circ01'00''$
A226	$01^h39^m00^s$	$-10^\circ11'00''$
S11	$11^h42^m58^s$	$-01^\circ42'50''$

Table 2.1: COMBO-17+4 Survey Field Coordinates

2.3 The Scientific Goals of the Survey

In order to probe the galaxy evolution in the interesting epoch between 1<z<2, the goals pursued by the COMBO 17+4 survey are multiple:

•The survey will provide very accurate $\delta z < 0.03(1+z)$ photometric redshifts, SEDs and masses for a large sample of several thousands of galaxies between $1 < z < 2$, providing for the first time the largest sample of galaxies in that redshift range.

• COMBO-17+4 will improve the determination of the stellar mass since the optical data do not properly cover the spectral contribution of the old stars which contain most of the mass. The NIR data gives access to the information contained in the old stellar population of high redshift galaxies with z>1 (which are too faint in the optical regime to be observed) and thus allows us to improve the determination of their stellar mass.

•The survey aim to establish the luminosity function for the red sequence and blue galaxies in the redshift range $1 < z < 2$.

•In order to investigate the galaxy mass assembly, the mass function for the red sequence and blue galaxies between $1 < z < 2$ is also aimed.

2.4 Survey Status

The COMBO-17+4 survey originally targets 3 fields, A901, A226 and S11, see Tab.2.1. At the time this thesis project started the A901 and the S11 field were the only targets for which the optical data were available and fully analysed. Even though the A226 field is the only field which has been successfully completed in NIR its optical counterpart has not been fully analysed yet, therefore the A226 is not included in this study. Furthermore, due to bad weather, the S11 field is still too shallow in the NIR, data acquisition for this field still has to be completed. Consequently, the S11 field is also not part of this thesis. Nevertheless the A901 field is the most interesting field to probe galaxy evolution since it contains the super cluster Abell 901/A902 centred at z=0.165 and gives the opportunity to study galaxy evolution for galaxies in clusters and in the field.

2.5 The Super Cluster Abell 901/902 to Probe Galaxy Evolution

The Abell 901-field has been chosen to investigate galaxy evolution out to z=2 in the frame of this thesis. The A901-field is also targeted by the multi-wavelength survey STAGES (Space Telescope A901/A902 Galaxy Evolution Survey) which provides HST-ACS imaging, XMM and GALEX coverage, 2dF spectroscopy and Spitzer photometry between 3.6μ and 24μ. The

STAGES collaboration investigates principally the physical drivers of galaxy evolution across a wide range of environments and luminosity, for more details see Gray et al. (2009).

2.6 Ongoing Ground Based Infrared Surveys

In the last few years a great number of NIR surveys to probe galaxy formation and evolution have emerged. Figure 2.1 shows the characteristic of ongoing multi-wavelength imaging and spectroscopic ground based surveys which include deep NIR and give the position of the COMBO-17+4 survey among them in terms of surveyed area and depth.

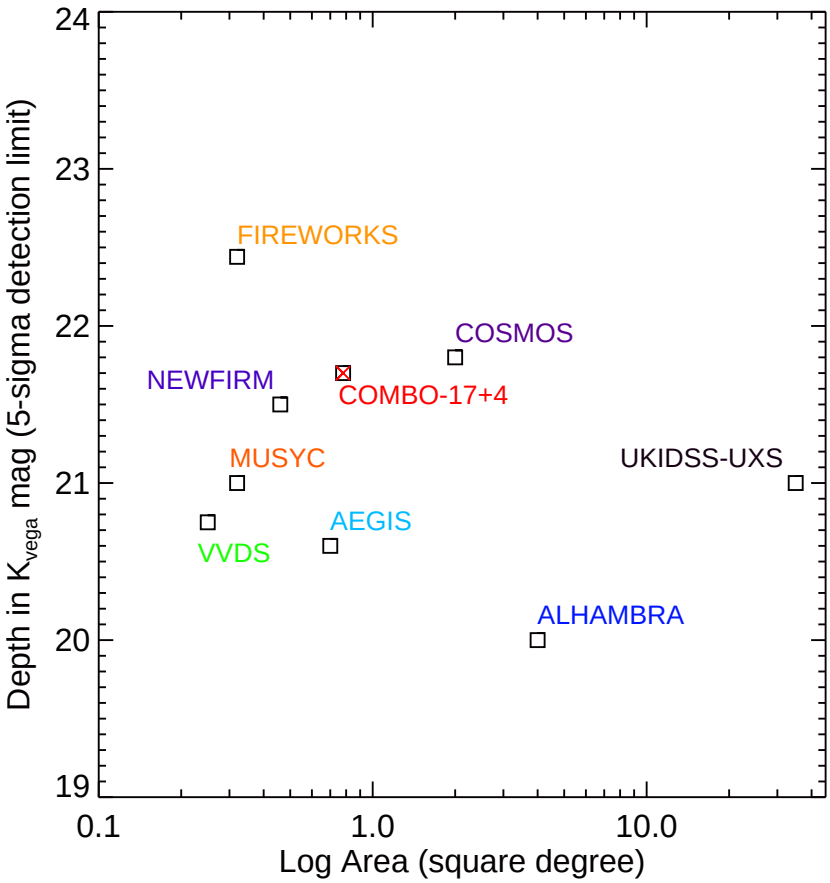

Figure 2.1: Depth and surveyed area of ongoing multi-wavelength surveys including NIR data. For the COMBO-17+4 survey, the depth in the H-band is given as a reference since the survey does not carry out K-band observations.

The majority of those surveys use only broad band photometry except for NEWFIRM and COSMOS [1] which also include medium-bands filters allowing a better photometric redshift accuracy. Despite of the use of NIR photometry, most of those surveys have so far only investigated the $z<1$ Universe. On the other hand, surveys like VVDS, UKIDSS, COSMOS, MUSYC, FIREWORKS and NEWFIRM have extended their investigation out to $z\sim2$. All these surveys combined will provide a profusion of data and results providing more information about galaxy formation and evolution since $z\sim2$.

[1] see list of acronyms at the beginning of this document for the meaning of the surveys names.

Chapter 3

From Photons to Photometry

The main body of this chapter explains the NIR data reduction which leads to the photometry. Obtaining the NIR photometry was one of the major contributions of this thesis. Accurate photometry measurements allows us to derive accurate colours which are the cornerstone for a reliable object classification necessary for assigning photometric redshift and Spectral Energy Distribution (SED) for each galaxy. This chapter explains each necessary step involved in the data reduction process to correct the NIR data collected by the telescope and allow the study of galaxy evolution through cosmic time. This chapter presents first the characteristic of the infrared sky, followed by the description of the instrument used to collect the NIR data and the observational strategy used in the frame of the COMBO-17+4 survey. The NIR observations used in the frame of this study are also presented.

3.1 The Atmosphere in Near Infrared

To better understand the procedure used to perform the data reduction and the type of data the COMBO-17+4 survey are dealing with, it could be helpful to first spend a few words to describe the sky in infrared. The Earth's atmosphere possesses a high transmission window between $\sim 320\,\mathrm{nm}$ to $\sim 2.6\mu m$ making optical and infrared observations possible for a ground based telescope. However, in infrared, the atmosphere is not completely transparent. Water vapour and CO_2 molecules being the main cause of absorption, filters are carefully designed to avoid the strongest absorption lines, see Fig. 3.1. Moreover, the infrared sky brightness is dominated by many emission lines. In the NIR regime from $\sim$950nm to $\sim$2.6μm, the sky background is dominated by narrow hydroxyl (OH^-) emission lines also called airglow. Figure 3.1 shows the intensity of the (OH^-) emission lines in the J- and H-bands. Infrared images have high background level due to the airglow and moreover airglow varies temporally and spatially. A study on the NIR sky brightness at the Calar Alto Observatory was recently done by Sánchez et al. (2008). This study shows that the (OH^-) emission varies during the day and are stronger during daytime and during twilight. They also observe that the (OH^-)

emission lines decrease in intensity by a factor 2 or 3 in one or two hours after the twilight, and does not increase again until just before the sunrise (Sánchez et al. 2008). A study by Fassbender (2003) shows that, at any time of the night, a variation between 10%-20% of the sky background level can be expected every ∼10 min in the H-band. In photometry, to obtain the flux measurement of a given source, we need to know the contribution of the sky background emission surrounding that source. We have to keep in mind that the NIR sky background varies temporally and spatially during the data acquisition which causes a direct impact on the manner the data reduction is performed. Fortunately, to first order this is deal sufficiently well by our photometry software which subtract the local time-averaged background around each object.

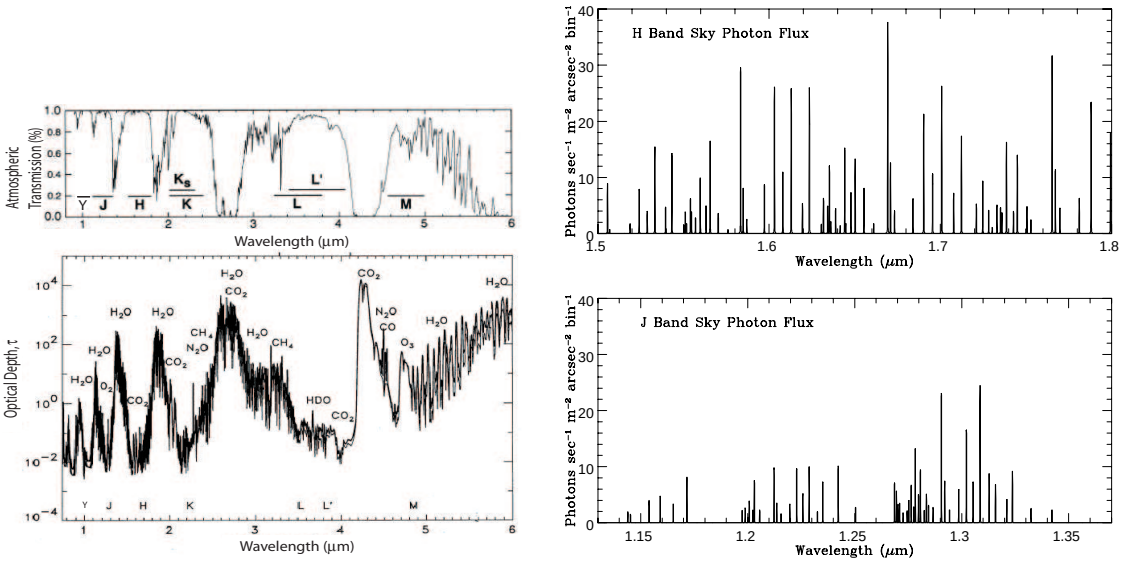

Figure 3.1: Left top: Atmospheric transmission window in the NIR with corresponding filter names, adaptation from Cox (2000). Left bottom: Molecules which contribute to atmospheric absorption in the NIR regime, Cox (2000). Right: Airglow caused by the OH^- emission lines in the J- and H-band from Herbst (1994), no data for the Y-band are available in the literature.

3.2 The Omega2k Camera

The OMEGA2k camera (PI: H-J Röser) has been created for surveys like COMBO-17+4 and HIROCS which are part of the MANOS project. The aim of the camera is to provide wide field high quality images to probe the distant Universe in the infrared. The OMEGA2k detector consist of a focal plane array (FPA #77) of type HAWAII-2, see Fig. 3.11. The detector array contains 2048×2048 pixels and its sensitive from 850 to 2500 nm. The camera is mounted at the prime focus of the 3.5m telescope at the Calar Alto Observatory, see Fig. 3.2. With a pixel size of 0.45 arcsec/pixel the camera has a wide field of view of $15.4' \times 15.4'$ (Baumeister et al.

2003). Wide field imager cameras often suffer from field distortions but one of the advantages of the OMEGA2k camera is that the distortion is negligible across the entire field of view (Röser 2006). The detector is divided in 4 quadrants each containing 8 channels. The camera offers several reading modes, the one used for the COMBO-17+4 survey observations is the Line Interlaced Read (LIR) which is the most time efficient mode (Kovács 2006). The camera cryostat contains 3 filter wheels with a possibility of several different narrow, medium and broad band filters. For more details on the OMEGA2k camera and a characterization of its detector and its different readings mode see Kovács (2006).

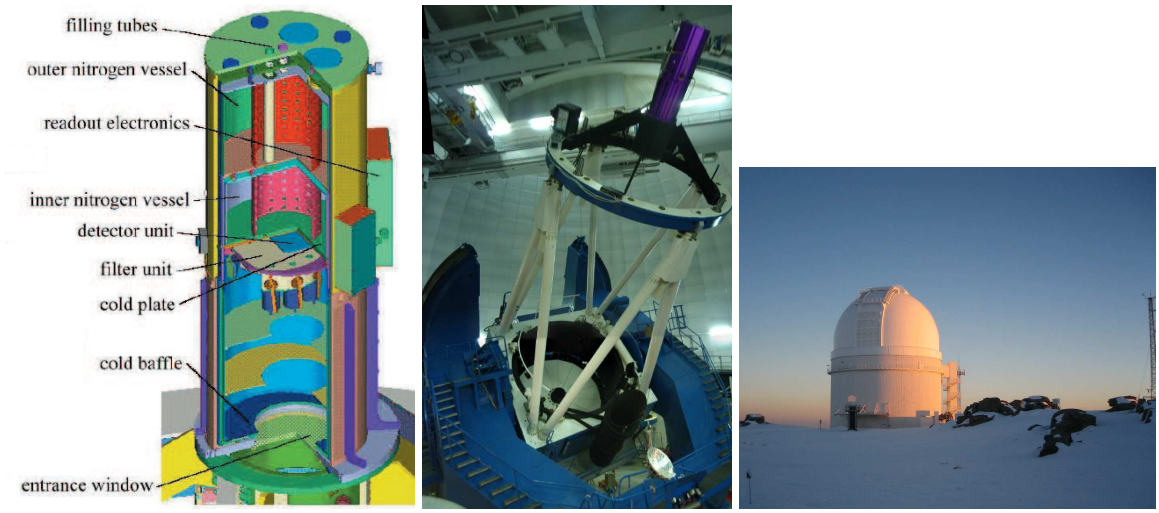

Figure 3.2: Left: Design of the wide field near infrared camera OMEGA2k. Middle: The camera attached at the prime focus of the 3.5m Cassegrain telescope. Right: Dome of the 3.5m telescope at Calar Alto Observatory.

3.3 Observational Strategy

The A901-field has a size of $30' \times 30'$ and was originally targeted by the Wide-Field imager (WFI) camera in La Silla Observatory. Since the field of view of the OMEGA2k camera is $15.4' \times 15.4'$ 4 pointings were required to cover the A901-field entirely. To this end, the full field has been divided into 4 subfields named A, B, C and D, see Figure 3.3. The 4 subfields were observed in 4 NIR filters including 3 medium band filters: Y, J1, J2 and the broad band H. The characteristics of the NIR filters used are listed in Tab.3.1 and the filter transmission curves are shown in Figure 3.5.

During the data acquisition the technique of dithering was applied. Dithering is a technique used frequently in astronomy. The technique consists of taking several exposures and moving slightly the position of the telescope relatively to the field centre between each exposure. In this way an object does not fall in the same pixel on different images. Frequent dithering allows a given pixel to see pure sky in most of the images. Figure 3.4 depicts this technique, the pixel A sees the pure sky in frame 1 to 4 but pixel B only in frame 1 and 2. When a median is calculated through the stack of images the object signal is eliminated and the result is a frame with pure sky only. This method allows a good sky background determination. All images taken at the telescope in the frame of the COMBO-17+4 survey were dithered.

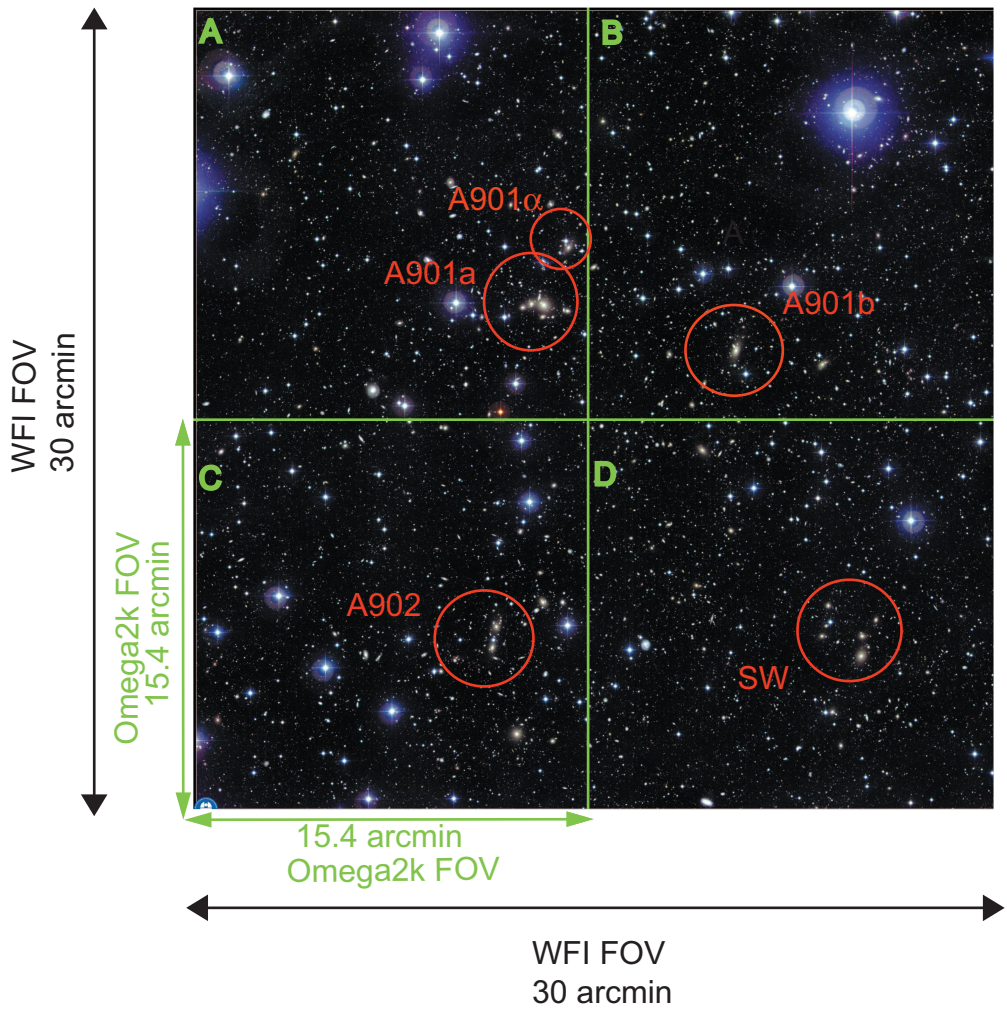

Figure 3.3: Optical composite image of the A901-field. The field is divided in 4 subfields named A, B, C and D. The circle show the galaxy clusters A901a, A901α, A901b and A902 as well as the South West galaxy group.

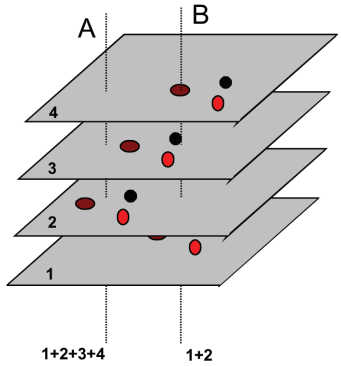

Figure 3.4: Stack of images with dithering from Röser (2006). In order to determine the sky background contribution, the images are aligned pixel-wise thus the pixel A sees the pure sky in frame 1 to 4 and pixel B in frame 1 and 2.

Filter Name	Central Wavelength (nm)	FWHM nm	5%cut off nm	5%cut off nm
Y	1034	75	988	1079
J1	1198	95	1141	1254
J2	1302	106	1239	1364
H	1647	266	1502	1797

Table 3.1: Characteristics of the OMEGA2k filters used for the COMBO-17+4 survey.

3.4 NIR Observations

The NIR observations were carried out over several runs between December 2005 and April 2008. Table 3.2 and 3.3 summarize the observations collected for this study. The total integration time reached in each subfield in each filter is shown in Tab. 3.4. Due to repetitive bad weather during the different observation runs, only the subfield A, B and C (i.e. 3/4 of the entire field) have been observed with a sufficient depth to reach useful magnitude limits for reliable photometry of faint objects in the field. As we can see on Tab. 3.4 the subfield D is far too shallow due to a lack of data in the J2- and H-band filter;[1] therefore this subfield is not included in the data analysis. The results presented in this thesis are based on data from the A901 subfield A, B and C only (representing an area of 0.2 square degrees on the sky).

Each image in the H-band is a 60 sec exposure which consists of a coaddition of 20 frames having 3 seconds exposure each. The J2-band images are 80 seconds exposures which are a coaddition of 8 images having 10 second exposure. The J1-band images are 100 exposures which are a coaddition of 5 images with 20 seconds and finally the Y-band images are 100

[1]Observations in subfields A, B and C have been obtained in Spring 2009 to complete the survey.

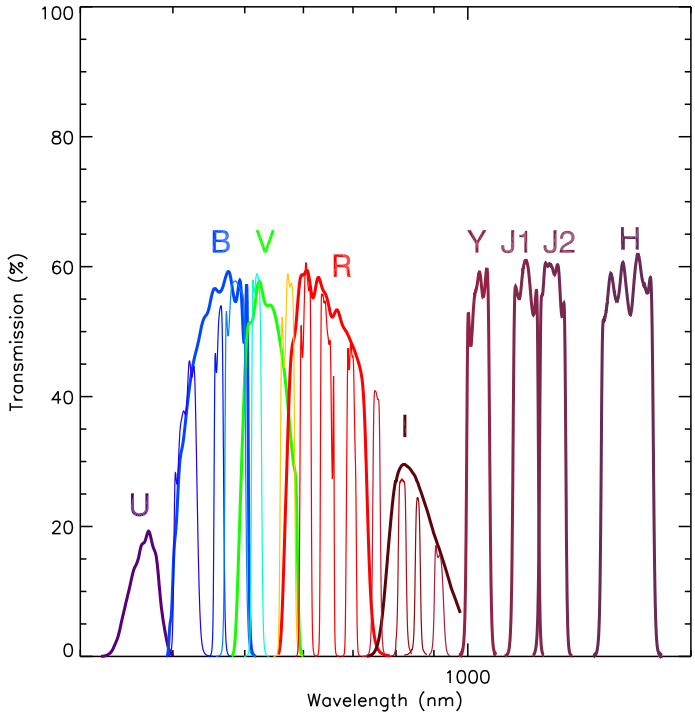

Figure 3.5: Transmission curves for the 21 filters used in the COMBO-17+4 survey.

seconds exposures with 10 images of 10 second coadded. Table 3.4 gives the total integration time obtained, all filters combined it is more than 1300 images which have been processed for this study.

In order to perform the data reduction, calibration frames are required. They have been taken besides the science frame for each campaign. The calibration series consists of a series of dark exposures with increasing integration time, series of dome flatfields with increasing integration time and a series of dusk or dawn sky flatfields. The calibration series allows to creates Bad Pixel Masks and Flatfields which are explained in the next sections.

The quality of the data can be characterized by the seeing[2] of the images. The seeing measurement of the images are shown in Fig. 3.6 for each filter and subfield. The seeing ranges from $\sim 0.85''$ to $\sim 1.5''$ depending on the subfields and the filters. For the photometry only images with seeing $< 1.5''$ have been used, see §.2.15 for photometry procedures.

[2]The seeing is a measure of the blurring of an image caused by the turbulence of the Earth's atmosphere. In ideal condition a point-like source (e.g. stars) is represented as a diffraction pattern with a central peak, the seeing is the measure of the FWHM of the distribution.

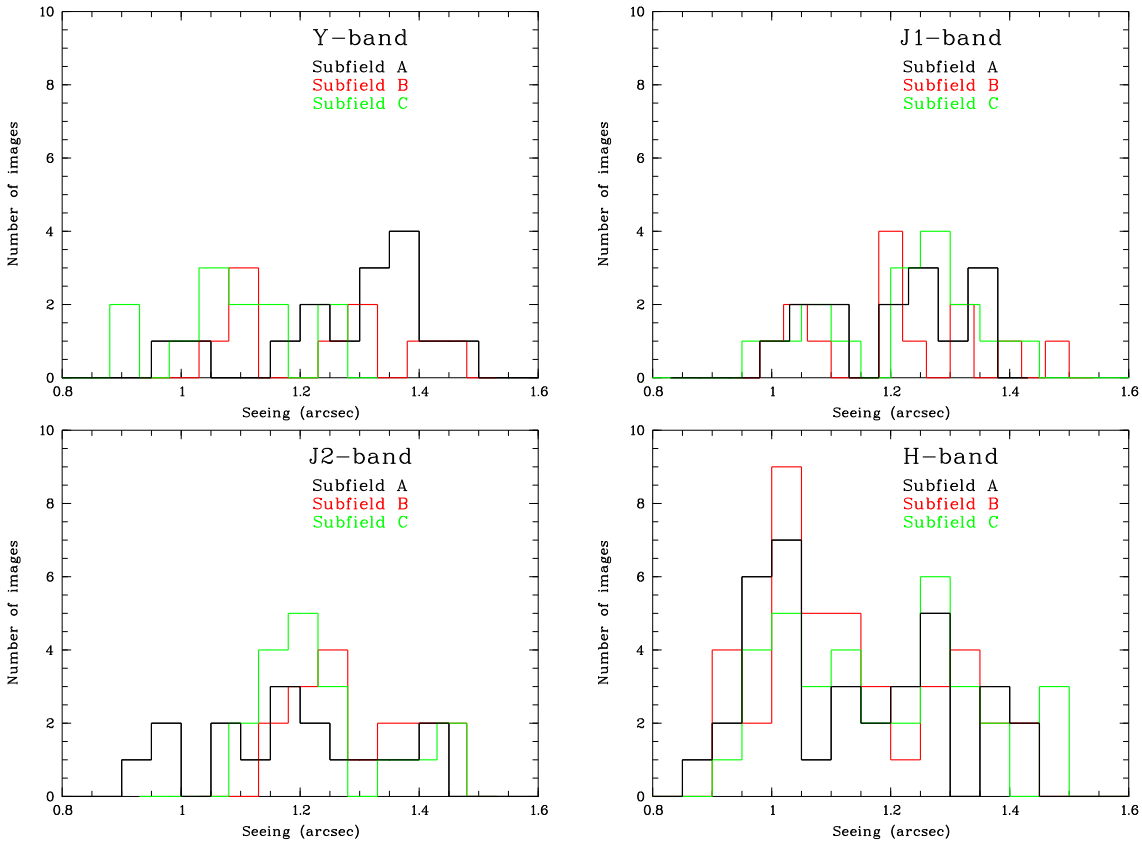

Figure 3.6: Histograms of the seeing distribution among the frames of different A901-subfields in the four NIR bands of the COMBO-17+4 survey.

3.5 Data Reduction Scheme

During the observations the photons emitted by distant galaxies are collected by the detector of a camera. Unfortunately the detectors used are never perfect, for example their sensitivity could be unequal or some of their pixels could be defective. These intrinsic imperfections must be corrected before any further analysis of an astronomical image. In addition, every pixel of the detector hit by high energy particles (cosmic rays) has to be corrected. This set of corrections applied to raw images coming from a telescope is called the data reduction. The goal of the data reduction is to provide images free of imperfections ready to calculate the photometry. The data reduction is a very important step which must be done carefully to be able to achieve an accurate photometry. The data reduction was performed with the software ESO-MIDAS (European Southern Observatory Munich Image Data Analysis System). MIDAS is developed and maintained by the European Southern Observatory. Under MIDAS the package MPIAPHOT developed by Röser & Meisenheimer (1991) was used for the data reduction and the photometry. The MPIAPHOT package was used for every step of the data reduction exempt for the flatfielding, the sky background modelling and subtraction and the

dark subtraction where the OMEGA2k data reduction pipeline developped by Fassbender (2003) was used.

The data reduction process is depicted in Figure 3.7. The next sections of this chapter describe in detail each step of this process. As an overview, the general data reduction procedure works as follows: for a set of data of a certain subfield (A, B or C) taken in the same filter (Y, J1, J2 or H), the raw images and a normalised flatfield image are used as input in the O2K-pipeline. The pipeline divides each image by the normalised flatfield image, then the sky background is determined and subtracted from each image. The output of the O2K-pipeline are flatfielded and sky-subtracted images for which the averaged sky level has been kept. [3] The next step is to correct for bad pixels and cosmic rays with the help of a bad pixel mask and a mosaic-median image. Then, several of the fully reduced single images with similar seeing are summed pixelwise by groups of 5 images. The dimension of each output summed frame is the common area of the 5 input individual frames. The final output are fully reduced images which are ready for the photometry.

3.6 Dark Current Correction

The dark current subtraction is generally the first correction applied to the raw images. The dark current is due to the thermal excitation of the electrons in the conductive bands of the detector. The dark current is always present even if the detector is not illuminated, and is a function of time and temperature. By cooling down to 78K, the OMEGA2k detector's dark current becomes very low, only $<0.03\ e^{-}/sec$ are produced by the dark current (Fassbender 2003). Since the integration time of a single NIR image is short ($\sim 3sec$), the dark current amounts to a few electrons only. Nevertheless, these additional counts have been removed by a subtraction of the dark current from the scientific raw images. To remove the right amount of dark current one needs to subtract a dark current frame with the same integration time as the raw images. The information of the dark current is contained in the sky background model created by the O2k-pipeline for each individual raw image. Hence, by subtracting the sky background model from the raw images, the dark current is also subtracted.

3.7 Flatfield Correction

One of the major corrections applied to the raw images obtained by the telescope is the so called flat field correction. The aim is to correct firstly the pixel-to-pixel sensitivity variation and secondly the global non homogeneous sensitivity of the detector. This pixel-to-pixel sensitivity shows fixed patterns on the image and thus is also called fixed pattern noise (FPN), see Fig. 3.8. The pixel to pixel sensitivity variation comes from the fact that each pixel cell

[3] That is, we subtract only the small-scale variation of the sky background with respect to its global value.

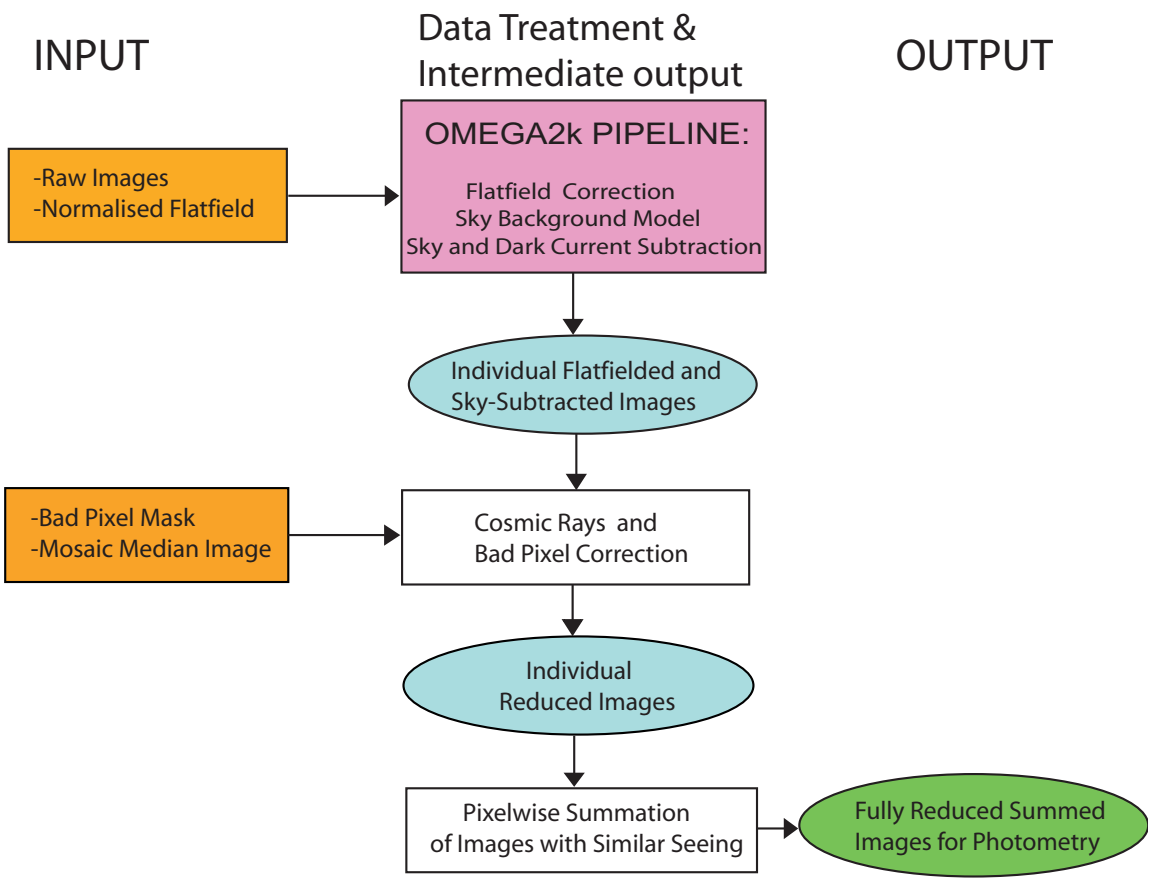

Figure 3.7: Data reduction scheme used to treat the NIR raw images from the OMEGA2k camera in the farme of the COMBO-17+4 survey.

unit may contain different levels of impurities. On the other hand, the non-uniform sensitivity across the detector (the variation of the quantum efficiency (QE)) is caused by the non-uniform thickness of the photosensitive layer which covers the detector (Kovács 2006) .

The pixel-to-pixel sensitivity variation as well as the global sensitivity variation of the detector must be corrected in a multiplicative way. The flatfield correction technique consists of constructing a flat field image from a series of dome flats and/or sky flats and dividing each scientific image by this normalised flatfield image. Since the fixed pattern noise depends on the wavelength, a flatfield image is needed for each filter used during an observational night (i.e. the Y-, J1-, J2- and H-band). To map the FPN and the detector global sensitivity variation we need uniformly illuminated images, hence the sky illumination during twilight is used to illuminate the detector. A sky flat series, which consists of a series of images of the sky, is taken for each campaign and is used to map the sensitivity variation of the detector. For the sky flat series a blank field (ideally with no stars) is targeted by the telescope, avoiding any

bright stars which could introduce unwanted patterns or saturate the images of the sky flat calibration series. To prevent the remaining stars from always falling on the same pixels of the detector, a telescope offset of a few arc seconds has been applied between each exposure of the series (i.e. dithering, see Fig. 3.4). The OMEGA2k acquisition software (Fassbender 2003) provides an efficient routine which maximizes the number of sky flats taken during the short twilight time. The routine automatically calculates the level of the background and adapts the exposure time to the changing light conditions to ensure that the count level is maintained around 15000 counts. When the exposure times get too long or too short the program stops. A sky flat series has been taken for each filter used for each observational night.

A representative flat field image is created with the MPIAPHOT routine FLAT/AVERAGE using the skyflat series. The routine aligns the stack of sky flat images by pixel coordinates. Since the images are dithered with respect to each other, an object never falls onto the same pixel. The routine looks through each same pixel of the stack of images and determines the median value. Pixel value above a certain κ-threshold are exclude of the median determination, preventing any cosmic or bad pixel to bias the median value. The routine FLAT/AVERAGE also creates an RMS image which contains the residuals (faint stars and cosmic events). In the median filtering process a κ-threshold value of 5-σ has been sufficient to remove faint stars and cosmic events. The result is a flat field image containing the global variation of the sensitivity of the detector and the pixel-to-pixel sensitivity variation. In order to be used by the O2k-pipeline, the flat field image is then normalised to one by dividing the flat field image by its median value. Before inputting this normalised flat field image in the O2k-pipeline to correct the raw images for the FPN and the global sensitivity variation, we need to correct the flat field for stray light if necessary as discussed in the next section.

Figure 3.8 shows an example of a normalised flat field image created from a sky flat series observed in the H-band filter. On the left panel we see the global sensitivity of the detector. The darker region on the upper left has a count level around 0.80 while the region in green in the lowest part of the detector has a count level around 1.20, meaning that the global sensitivity varies about 40% across the detector. Similar results are found for flatfields in the medium bands Y, J1 and J2. The quality of each flat field created for each observational night has been tested. Results show that a raw image which has been divided by a flat field has a noise level which is ~20% of the expected photon noise which is not perfect but acceptable.

3.8 Stray Light Correction

The OMEGA2k camera suffers from a stray light (or internal reflection light) problem. Stray light appears on every single image taken with the camera, forming a ring pattern centred in the middle of the detector, see Figure 3.9. The origin of this stray light is not yet fully understood

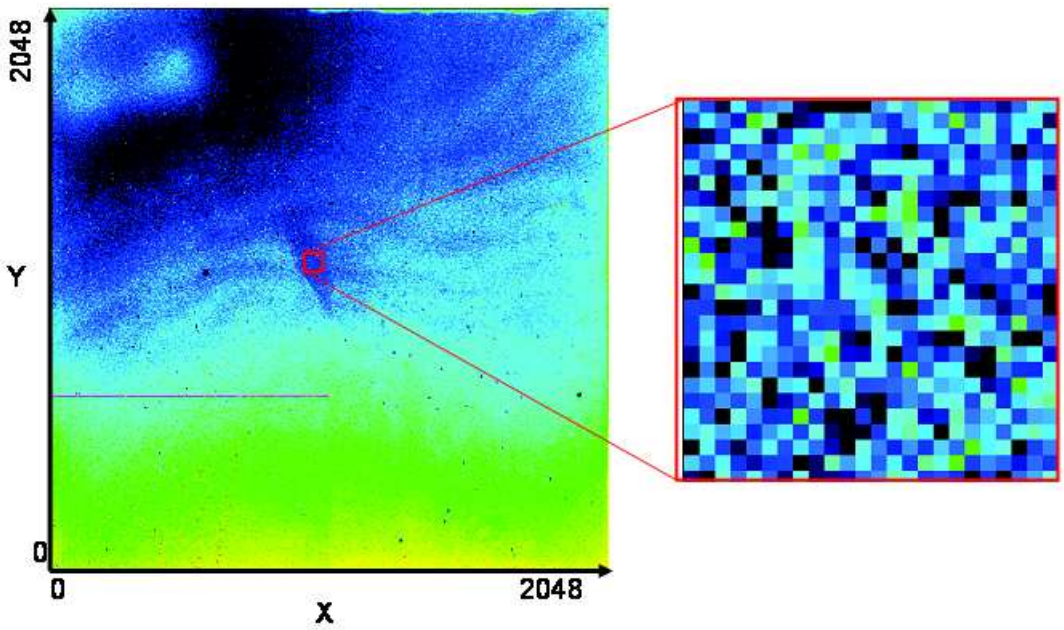

Figure 3.8: Normalised flat field in the broad band H ($\lambda = 1647nm$). The left panel shows the global variation of the sensitivity of the detector of the camera OMEGA2k. The right panel shows a zoom into the image, the pixel-to-pixel variation becomes apparent. The colour cut is between 0.80 counts(dark blue) to 1.20 counts (green).

but likely comes from some reflected light by an optical surface in the OMEGA2k camera.

The intensity of the stray light is more or less pronounced depending on the filter used. No relation has been found between the intensity of the stray light and the wavelength (i.e. no monotonic trend was found as a function of the wavelength λ). It has been found that the stray light is much more intense in the J2 filter for which it contributes an additive 10% of the flux. For the J1 and the Y filter the stray light contributes about 5% and for the H filter the contribution is negligible with less than 0.5%. Stray light contribution can be ignored in the science images since the photometry routines will subtract it correctly as a background contribution. However, the stray light contribution could severely corrupt the flat fields. For example, a central enhancement of the flat field exposure by 10% can mimic a central increase of sensitivity which is not present. So correcting for it would incorrectly decrease the contribution of objects by 10%. Great care has to be taken to remove any stray light contribution from the flat field exposure. Accordingly, it is most important to subtract the ring pattern to the flat field images. Since the scientific images are divided by the flat field image, if the flat

field contains the additive contribution of the ring, the scientific images would be divided by a wrong background shape, thus the ring pattern is removed first from the flatfield image. The stray light correction has been applied for flatfields in the Y, J1 and J2 bands. The method used to correct for the stray light is done in 3 steps: for a given normalised flat field image the ring is first isolated then modeled and finally subtracted from the original flat field image. The detailed procedure is the following:

•In order to isolate the ring from the flat field image, a model of the background shape of the flat field image has been created by fitting a 2 dimensional polynomial function with the help of the MIDAS command FIT/FLAT, resulting of an image of pure background. By dividing the original flat field by the background model the contribution of the ring has been isolated in a separate image.

•The ring is then modeled with the MPIAPHOT routine FINDRING which transforms an image from Cartesian coordinates x,y to polar coordinates r,θ with a given centre. The exact centre of the detector (in pixel coordinates) has been used since the ring pattern is well aligned with this one. The routine interpolates and smoothes the image in the r^2 and θ direction with a given window size of 10 by 10 pixels. The result is a frame containing the smooth model of the ring, which is then multiplied by the model of the background to recover the varying sensitivity gradient over the ring. This results in a model of the ring which contains the additive contribution plus the shape of the global detector sensitivity gradient.

•This elaborate model of the ring is finally subtracted from the original flat field image.

This normalised flatfield image free of stray light is used as input in the O2K-pipeline which performs the flatfielding. In the flatfielding process the raw images are divided by the ring-free flat field image. Since the stray light pattern is present in every raw image, the result is images corrected for the FPN and the global variation of the sensitivity but which still contain the additive contribution of the stray light. The ring pattern is then removed at the level of the sky subtraction which is the next step performed by the pipeline as described in the next section.

3.9 Sky Determination and Subtraction

The OMEGA2000 data reduction pipeline (or o2k-pipeline) from Fassbender (2003) has been used to perform the sky background modelling and subtraction. As we have seen in §3.1, the NIR sky background varies in shape and intensity on a short timescale. For example in the H-band the sky is said to be "stable" for a period of only about 10 min. For a typical sequence of data acquisition of 40 min, the shape and the intensity of the sky background could be

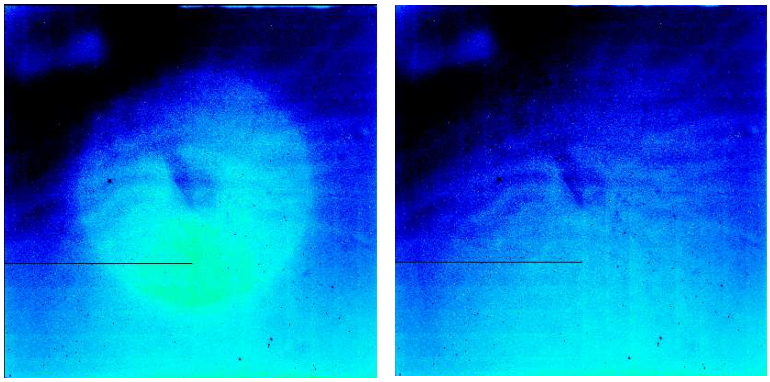

Figure 3.9: Flat field image in the narrow band J2 ($\lambda = 1302nm$). On the left one can see the reflected light which produces a ghost image of the telescope prime mirror in the centre of the image, on the right the stray light has been removed.

totally different between the first and the last image of the sequence, since the images are taken chronologically with the camera. The method applied by the O2k-pipeline to determine the background is to use n number of images prior and subsequent to a given image position in the stack. Best results are obtained by using 5 images bracketing the respective image. This means that for a given image the sky background is determined using a stack of images containing the 5 frames taken before the given image and the 5 frames taken after the given image.

Figure 3.10 from Fassbender (2003) shows the different steps involved in the sky modeling process performed the O2k-pipeline. First, the O2k-pipeline loads a stack of images all taken in the same given filter. Since the different images of the stack are offset from each other (dithered Fig. 3.4) an astronomical object does not fall always on the same pixel. Second, the O2k-pipeline aligns all the frames pixelwise and for each pixel column through the stack of input images, the pixel values are extracted and sorted. The sky signal is determined in each pixel of each image of the stack of images by taking the median or the minimum value from the sorted pixel column values. For our purpose, the mode outlier-clipping has been used to create the sky model. In this mode the pixel containing a value a given $\kappa - \sigma$ above median (for our purpose $3-\sigma$ has been used) are excluded from the median determination. For each pixel the median sky value is thus determined and saved in a sky model array. This sky frame is then subtracted from the scientific image of the stack.

Using the sky subtracted images, a second iteration called the double background subtraction as been performed by the O2k-pipeline. This second iteration is applied because in the proximity of bright star halos or objects which extend larger than the dither pattern, the median sky value is distorted. In order to better extract the sky background level in these regions, the O2k-pipeline performs a second iteration in the background determination using

an object mask. In this step the objects having a κ-threshold $> 1.2-\sigma$ are masked out by an object mask created by the pipeline. The masked regions are projected onto the raw frame and replaced by the local median value determined from the closest unmasked pixels. As in the first iteration the median sky value is determined for each frame and subtracted. At the end the flux level of the image is preserved by adding the mean count level of the background after the background subtraction.

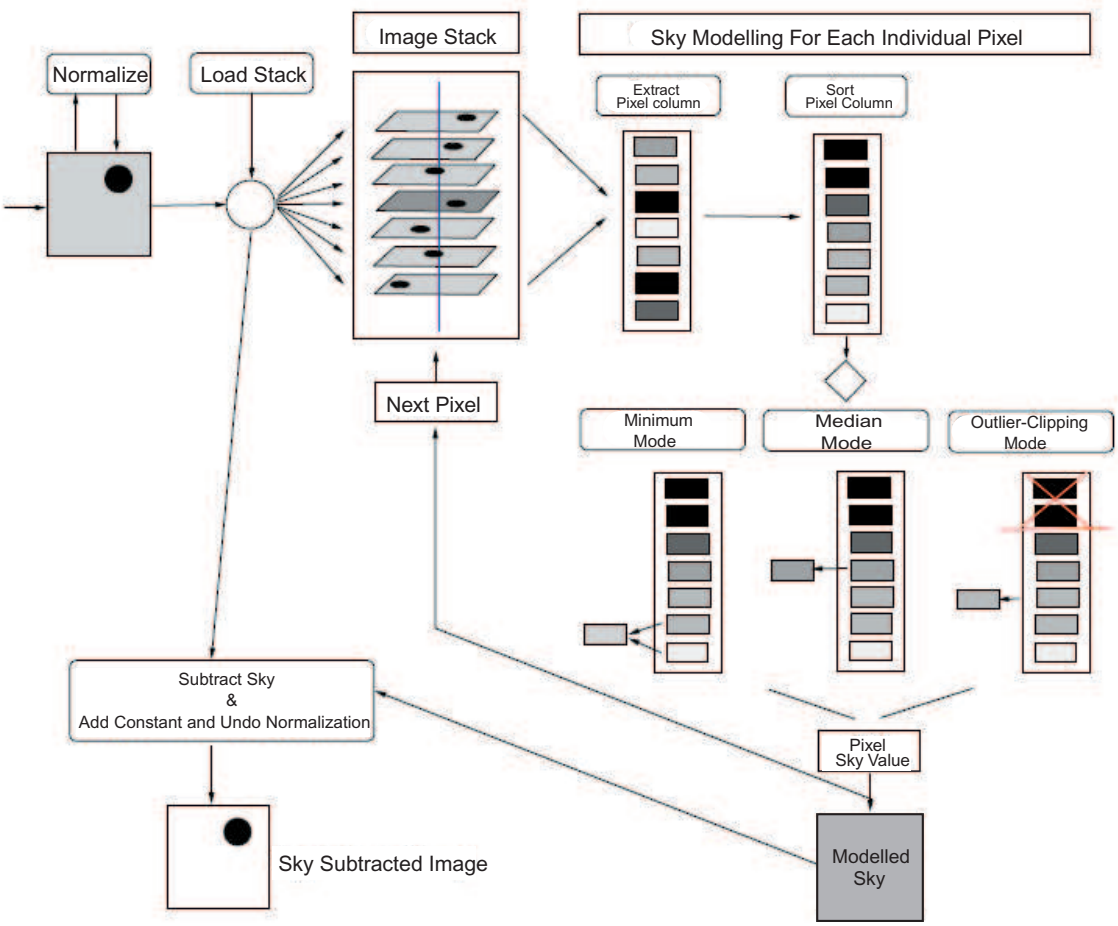

Figure 3.10: Schema of the sky modeling from Fassbender (2003). The solid black circle on the different frames of the image stack represent the same astronomical object which falls in a different pixel due to the dithering. The different shade of grey in the pixel columns represents the different count level, from low count level (light grey) to high count level (black).

3.9.1 Quadrant Structure Correction

Quadrant structures could appear in the images taken with the OMEGA2k camera due to a combination of passing clouds and the reading mode of the detector. The OMEGA2k camera detector is composed of four electronically independent quadrants. Each quadrant is read

in the way shown in Figure 3.11. The mode used for the data acquisition is the LIR (Line Interlaced Read). In this mode each line of the detector is read-reset and read again before the integration start. The second readout provides the reset level of the detector. For more details about the different reading mode of the OMEGA2k detector see Kovács (2006) as well as the OMEGA2k User's Manual (Röser 2006). However, if clouds pass across our field of view and suddenly increase the count level between the reset and the next acquisition, the reset value will be too high compared to the real count level. This phenomenon produces quadrant structures in the images, Fig. 3.11 (right panel). When this occurs, the quadrant structures in a given frame have to be flattened before using them as input in the O2k-pipeline in order to ensure objects recognition possible during the sky modelling process. The quadrant structures appear mostly in images taken in the broad band H and the medium band J2 data which are the most sensitive to water vapour. This quadrant pattern appears only if some low altitude clouds happen to pass over during the data acquisition, which is not often the case but the frame must be corrected if this occurs. For images having quadrant structures the background of the images has been smoothed and subtracted. After the quadrant structures have been flattened, the variation across the junction of the four quadrants is less than 1%.

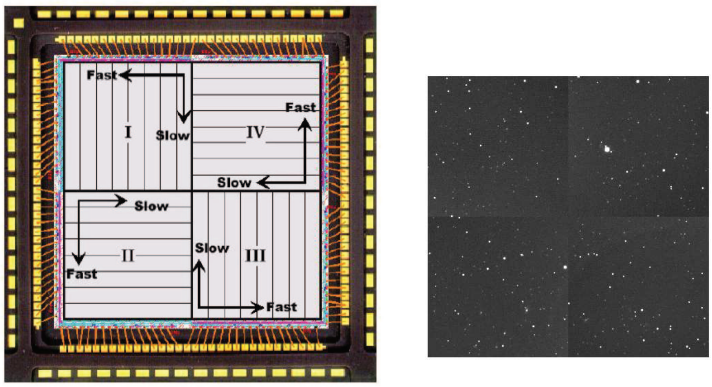

Figure 3.11: Left: Shema of the reading mode of the OMEGA2k camera detector. Right: Quadrant structure in a sky subtracted frame from the A901 subfield B in H-band, we see that at the junction of the quadrants the sky level is unequal.

3.10 Build a Bad Pixel Mask

The OMEGA2k camera detector contains approximately 1% bad pixels on his array. A bad pixel is a pixel for which the response to the illumination of the detector is not linear. A bad pixel can be a hot pixel, a dead pixel or simply a pixel for which the response is not linear. A hot pixel is a pixel which seems to be always illuminated and in contrary a dead pixel is a pixel which seems to never be illuminated. Bad pixels must be identified and corrected since the information they contain is meaningless and can corrupt the photometry of an object. In

order to correct for the bad pixels, a bad pixel mask is created. Bad pixels are replaced by a median value using the same technique as the cosmic rays correction which is explained in §.3.11.

The technique used to identify the bad pixels utilize different calibration frames. A series of dark and dome flat frames with different exposure times from 2s to 100s are used. For the dome flat series one must be sure to use an appropriate lamp power to illuminate the dome and thus avoid saturating the detector. For the OMEGA2k camera one expects the detector to be linear up to 30 000 counts. Whatever the filter used for the dome flat series the lamp must be dim enough to reach $\sim$ 30 000 counts in a integration time of t $\sim$ 100 seconds. As an example, Figure 3.12 shows the response in counts as a function of the exposure time for a set of 12 central pixels belonging to the OMEGA2k detector (the FPA#77 detector). We see that the response is linear until 30000 counts. For every pixel of the detector a linear fit has been performed through a stack of dome flats frames with increasing exposure time. A slope, a constant and RMS are derived from the fit and are analysed to identify the bad pixels.

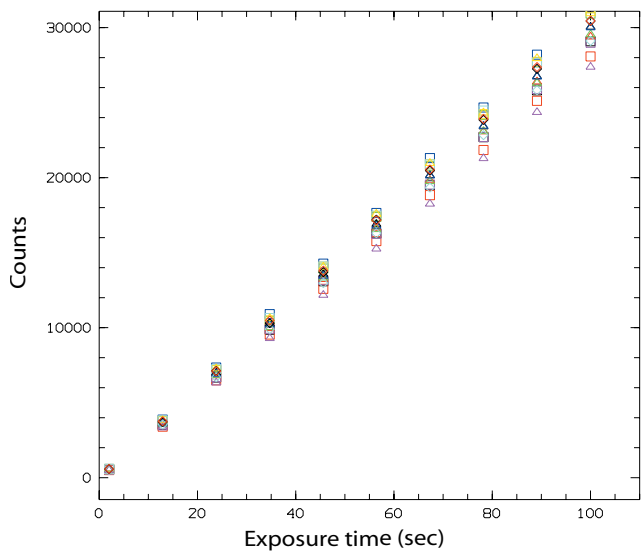

Figure 3.12: Linearity regime of the detector FPA#77 in the OMEGA2k IR camera. Each symbol represents the behaviour of a single pixel of the detector through a series of dome flats with increasing integration time from 2s to 100s.

The distribution of the different slope values derived from the linear fit is shown in the Figure 3.13 (top left panel). The pixels which have a slope value deviating by more than 3σ of the mean slope value are flagged as bad pixels. About 5500 bad pixels have been flagged this way. The root mean square (RMS) values resulting from the linear fit represent the scatter of the pixel values around the fit and is also used to find bad pixels. The pixels which deviate

from a linear behaviour have a high RMS value. Pixels were flagged bad pixels if their RMS values were $>5\sigma$ of the mean RMS value. The RMS values histogram is shown on Fig. 3.13 (top right panel). About 1200 bad pixels have been found this way. Bad pixels can also be found by using the distribution of constant values added to the linear fit, Fig. 3.13 (bottom panel). Pixels with a very low $<3\sigma$ (dead pixels) or a very high $>3\sigma$ (hot pixels) constant value are flagged as bad pixels. About 22000 bad pixels have been found by this latter method.

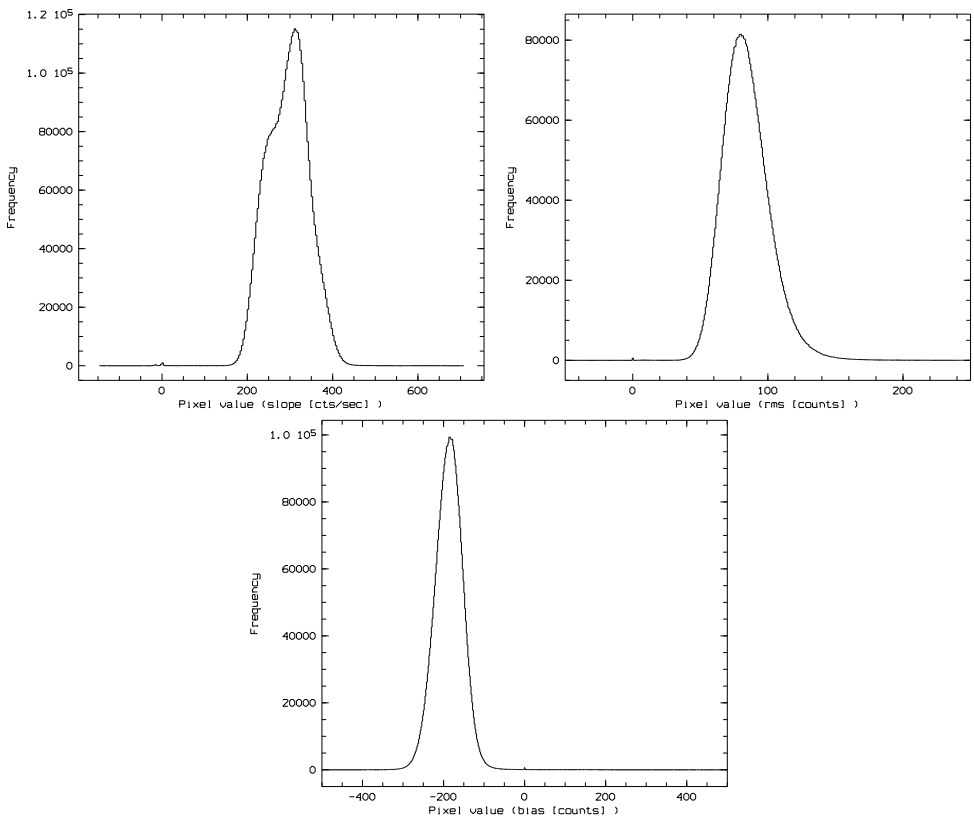

Figure 3.13: On the upper left the histogram of the slope values derived from a linear fit through a stack of dome flat frames with increasing exposure time. On the upper right the histogram of the RMS values, the bottom panel shows the histogram of the distribution of the constant values.

An efficient way to create a bad pixel mask is to combine the bad pixels found with the slope values, the RMS values and the constant values distributions. The result is shown in Figure 3.14. Each bad pixel is shown in black while good pixels are in white. We can distinguish a bad pixel line in the middle left bottom quadrant. This bad pixel mask contains ∼28000 bad pixels (0.7% of all detector pixels). An individual bad pixel mask is created for each different observational campaign since each time the camera is dismounted the amount of bad pixel changes.

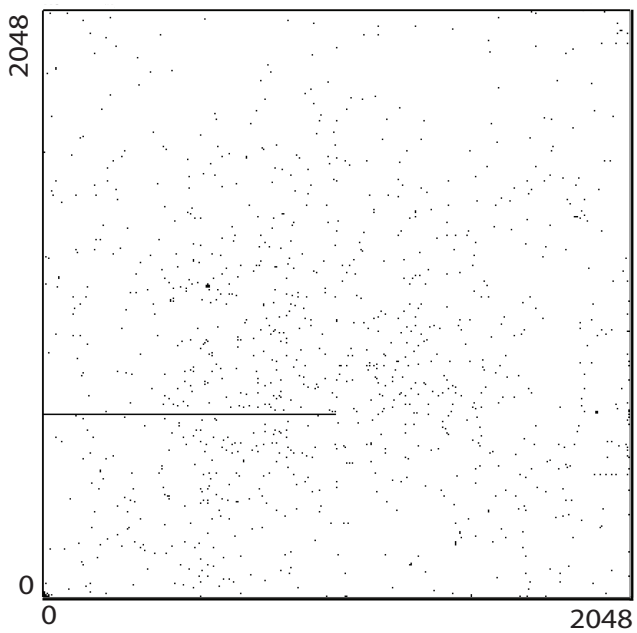

Figure 3.14: Bad pixel mask created to flag the deviating pixels of the OMEGA2k detector. The bad pixels are shown in black while the good pixels are shown in white. Not all bad pixels are visible on the image since the resolution of this document is not high enough to see all of them.

3.11 Cosmic Rays and Bad Pixels Correction

Cosmic rays are high energy charged particles which produce spurious signals when they hit the detector and thus can corrupt the photometry of an object. They must be identified and replaced before attempting any photometry. The cosmic ray removal has been done with MPIAPHOT packages with the help of a mosaic median image created from the sky subtracted frames from all pointings. The aim of the mosaic median image is to be able to correct pixels hit by cosmic rays which are located on the edge of the frames and at the junction between the different subfield where the coverage is not sufficient if we use dithered frames from only one same subfield (pointing). Since the frames are dithered from each other there is small overlap at the junction between frames from different pointings. For each of the NIR filters: Y, J1, J2 and H, a mosaic median image is created and used to perform the cosmic and, at the same time, the bad pixel correction in each individual frame. To perform the cosmic correction the procedure is done in 3 steps:

•First, a mosaic median image is created out of the assemblage of all individual frames from all pointings.

•Second, each individual frames is compared with the mosaic median image and deviating pixel are flagged.

•Third, the flagged pixels in the individual frames are replaced by the median value from the mosaic median image.

In more detail, for each of the NIR filter Y, J1, J2 and H, a mosaic median image is created with a set of MOSAIC routines offered by the MPIAPHOT package. First a reference table containing bright stars across all the A901-field in gnomonic coordinates relative to the projection centre has been created. The reference table coordinates are projected into each frame (gnomonic projection)[4]. Then, a mosaic image is built by inserting all individual gnomonic frames from all pointings (subfield A, B and C) at the right position in a large output image. During the mosaic assembling, for each pixel, a median value is calculated by looking at the values in that pixel position through the stack of different dithered individual frames. The resulting mosaic contains the calculated median values for each of its pixels. A median value is obtained only if a pixel is covered by at least 3 frames otherwise the pixel is flagged and will not be use for the photometry. The centre of the mosaic is never a problem since it is covered by several frames. This is not the case in the extreme border of the mosaic were sometimes only one or two frames overlap.[5] In the next step, each pixel value from each individual frame is compared to the pixel value in the mosaic image at that given position. If the pixel value from the individual frame deviates by more that 5σ of the median value, this pixel is flagged as a cosmic. In a second iteration, the neighbourhood of each detected cosmic is analysed, this time pixels which deviate for more than 2.5σ are flagged as cosmic. For each frame a cosmic mask which contains the position of the pixel hit by a cosmic event is created. The bad pixel correction is performed at the same time as the cosmic correction. The position of the bad pixels are known from the bad pixel mask. Frames from the same observational campaign are associated to their respective bad pixel mask (BPM). For each frame the gnomonic projection of the BPM is calculated and added to the cosmic mask. Then, the deviating bad pixels in the individual frames are replaced by the median value contained in the median mosaic image for that pixel. The cosmic masks contain the positions of the bad pixels and the pixels hit by cosmics in the gnomonic frames, making it possible to recover those pixels in the original frames by applying a back transformation of the gnomonic projection. After the cosmic and the bad pixel correction, the frames are fully corrected and ready for the photometry.

[4]The gnomonic projection is the projection of points on the surface of a sphere from a sphere's centre to a point onto a tangential plane.

[5]The objects located in the extreme edges of the mosaic where the cosmic and bad pixel correction were not possible are excluded from our object catalogue.

3.12 Frame Summation

Ideally, to have a better estimation of the fluxes measurements and their errors, the photometry should be performed using every single reduced image. Because of the limited capacity in the MIDAS table files, the number of images used to perform the photometry had to be reduced. For this reason the images are summed by groups. The summation has been performed with the MPIAPHOT routine SUM/IMAGE which calculates a straight-forward pixelwise summation. The summation process is integer pixel based and the resulting summed image has the dimension of the common area of all input frames.

The individual frames with a similar seeing ($\Delta \leq 0.1''$) in a given filter have been summed by groups of 5 which was a good compromise between the obtained S/N ratio of the summed frame and number of frames available to perform the photometry. Grouping the single exposure frames together allows to increase the S/N of the resulting frames but unfortunately deteriorates the seeing quality. In fact, for input frames of the exact same seeing the resulting summed frame has its seeing increased by $\sim 0.1''$ due to the frame alignment which cannot reach a better accuracy. The summation process is the last step of the data reduction. The images are now summed and fully reduced.

3.13 Deep H-band Catalogue

A deep H-band sources catalogue used to identify the objects and obtain their photometry has been extracted from our deep H-band mosaic image. The H-band mosaic image is built from the sum of gnomonic images in the H-band from all pointings with the MPIAPHOT routine MOSAIC/SUMUP. The sum is a weighted sum in which the input gnomonic images are weighted according to their depth. The weight is calculated as follows:

$$weight = \frac{1}{(transmission) \times (background \quad noise)^2 \times PSF^2} \tag{3.1}$$

which give the best results for point sources (Gabasch 2004). The A901 H-band mosaic image is built from 114 summed frames among the 3 different pointings for a total exposure time of $t_{exposure} \sim 11\,600$ sec/pixel. The H-band mosaic has a seeing of $1.03''$; since the mosaic image is the result of a weighted sum only the best seeing images contribute significantly.

The software SExtractor (Bertin & Arnouts 1996) has been used to identify sources in the H-band mosaic deep image. The SExtractor default parameters have been used. In that case the minimum amount of pixels required to detect an object is adjusted to the seeing of the mosaic. A threshold in units of S/N ratio of 4.7 has been used. This threshold fixes the lower limit on the magnitude error which corresponds to $0^m.21$ of the total magnitude MAG_BEST

calculated by SExtractor. Also, the minimum amount of pixels needed to identify an object is adjusted to the seeing of the image. SExtractor allows the use of a weighted image to weigh the object detection according to the different depths within the mosaic image. Tests demonstrate that better results are obtained by using a weighted image. In fact, the depth and the point spread function in the 3 different mosaic subfields varies a little due to the different integration times reached in each individual subfield, see Table 3.4. Figure 3.15 shows the mosaic image which has been used to derive the H-band catalogue.

The deep H-band source catalogue has been compared to the deep R-band sources catalogue previously obtained by Wolf et al. (2003) to derive the original optical-only COMBO-17 photometry. The H-band catalogue recovers most of the sources detected in the deep R-band catalogue. The optically faint blue objects which are too faint in the NIR are manifestly missing in the new H-band catalogue but since our study focuses on the red objects and high redshift galaxies it is not essential to recover those blue faint objects. A detailed comparison between the optical catalogue based on R-band and the new NIR catalogue based on H-band will be discussed in the next chapter.

The optical photometry has to be re-derived based on the deep H-band source catalogue instead of the previous R-band catalogue. Thus, both the optical and NIR photometry of COMBO-17+4 are based on this deep H-band sources catalogue. An area of $68'' \times 76''$ centred on the very bright star in the middle of the field as been cut from the catalogue to avoid spurious objects created by the star halo. The resulting A901-field sources catalogue contains a total of 31747 objects.

3.14 Gnomonic Projection

The photometry is obtained by projecting the object coordinates from the H-band catalogue into each frame and measuring the flux at that position. For this end, the position of 100 bright unsaturated stars are compared between the H-band catalogue and the individual frames. The accuracy of the projection is very good with $\leq 0.1''$. Figure 3.16 shows an example of the scatter in the accuracy of the projection for a frame versus the radius centred in the centre of the frame, here the RMS value is $0.074''$. During the projection process the best guess PSF shape is determined from the same bright stars used for the projection. The PSF value determined for each summed frame is fundamental and used as input in the aperture photometry process.

3.15 Photometry

Once the frames are fully corrected and thus free of imperfections due to the various phenomena discussed previously, the flux of each object in the A901-field can be measured. The

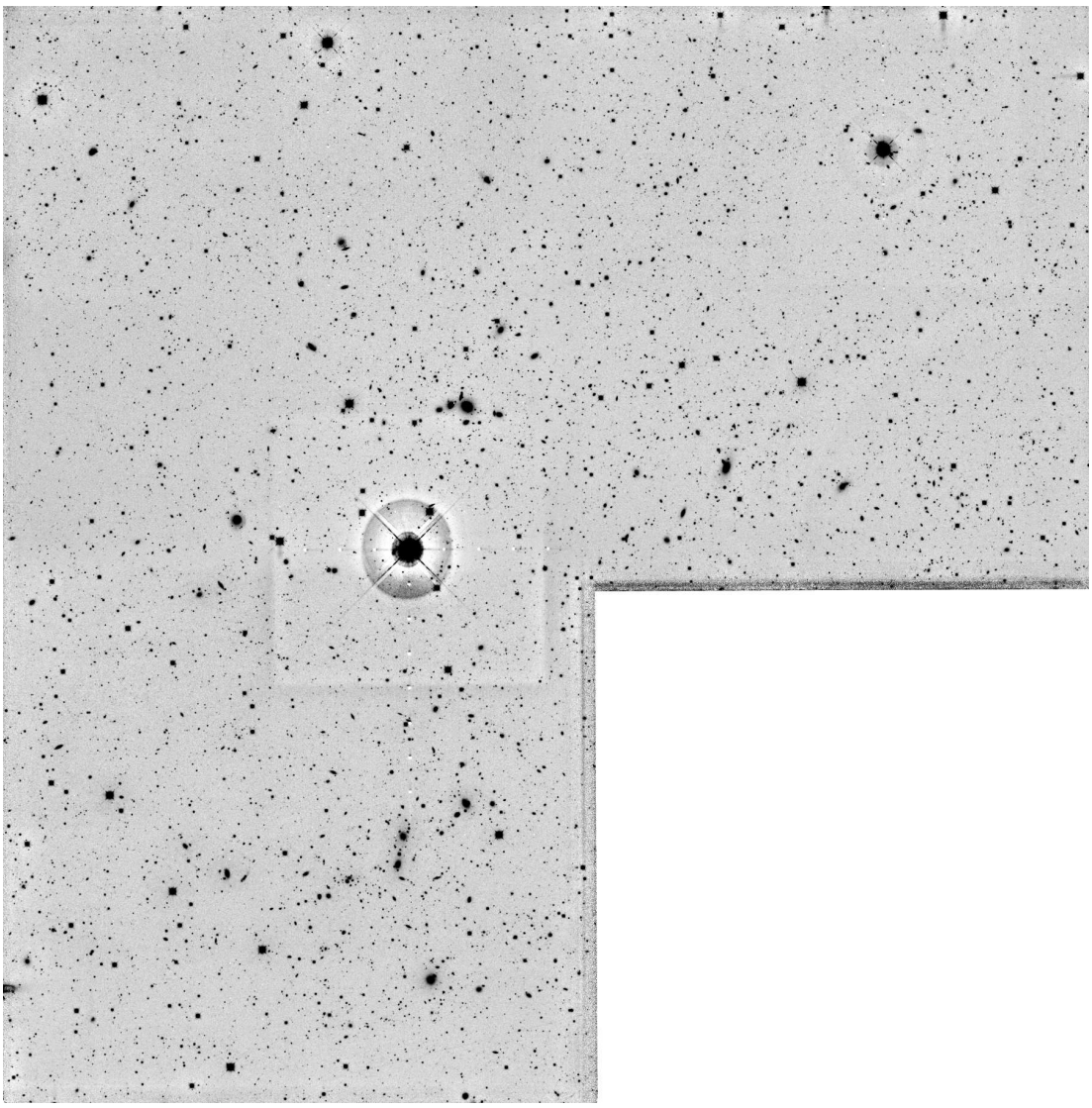

Figure 3.15: Mosaic image of the A901-field in the H-band filter used to extract the H-band source catalogue. The very bright Mira variable star with a magnitude K=5.75 and spectral type M8 III (Gray et al. 2009) appears in the middle of the field. The reader is invited to compare this image with the counterpart optical image in Fig. 3.3, in NIR the distant galaxies and red stars shine while blue stars and galaxies appear fainter.

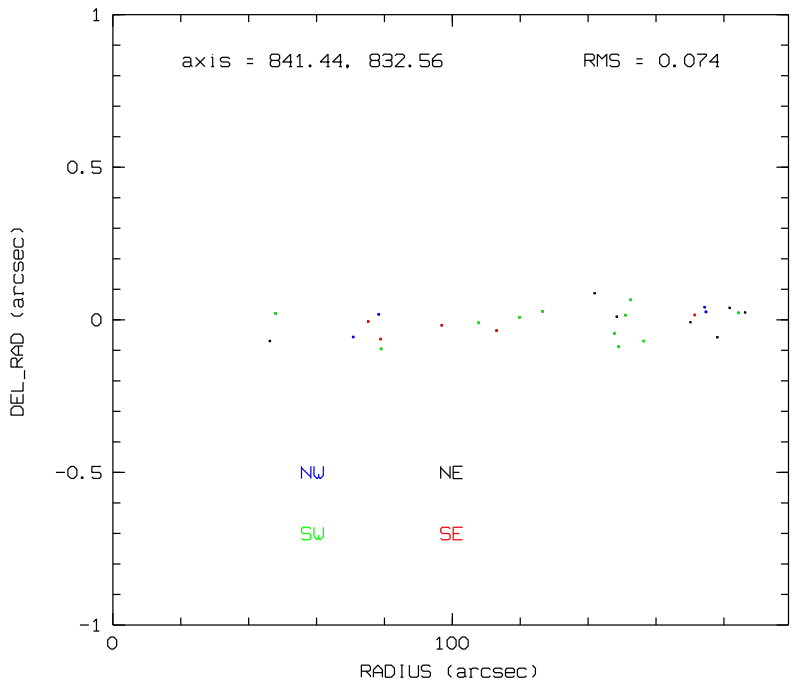

Figure 3.16: Accuracy of the gnomonic projection for an image of the A901 subfield A. Error on the position Δ_RAD as a function of the radius centred in the middle of the detector.

photometry is performed using the EVALUATE/IMAGE routine from the MPIAPHOT package (Röser & Meisenheimer 1991). The routine performs a seeing adaptive weighted-aperture photometry. In essence, the central surface brightness of an object is measured on an individual frame convolved to a common PSF of 1.7″ FWHM. By proceeding that way, one obtains a better estimate of the flux error measurements than performing the photometry directly on a single summed deep exposure. The routine chooses the necessary Gaussian smoothing to reach a common effective PSF of 1.7″. The PSF is thus uniform in all frames in all of the 21 bands. The EVALUATE setup file used to perform the photometry can be found in the Appendix B. Subsequently, all flux measurements from an individual filter are combined into a single deeper filter measurement using the routine CADIS/UNITE.

The count rates are then converted into physical units (photons/$(s \cdot nm \cdot m^2)$ for each flux measurement by calibrating the counts with chosen standard stars for which the spectrum have been convolved with the telescope and filter transmission curve (optics system efficiency). As we have seen, the whole A901-field is composed of a mosaic of 3 subfields and each subfield is composed of several dithered frames. Before calculating the photon flux for each source in a given waveband, the relative flux must be calibrated among the different frames of that given waveband. Standard stars in each subfield have been selected for this purpose. The standard stars are used to adjust the count-rate to flux conversion among the different frames in a given

filter. After calibration the flux of the standard star is the same in each frame in a given filter. The objects flux in each frame is rescaled accordingly.

To calibrate the subfield A and C two standard stars have been used while four standard stars have been used to calibrate the subfield B. The amount of standard stars used to calibrate each subfield depends on the amount of good standard star candidates available in each subfield. The different standard stars have been selected from the R-band catalogue according to their magnitude, colour and spectral type. Since we want to calibrate the NIR data one should avoid very blue stars which might be bright in the optical regime but too faint in the NIR regime. Thus stars with a colour B-R$\sim$0 and R$<$20 have been selected. The last requirement was the quality of the star spectra available in the Pickles (1998) spectral library, see §4.3.1. Stars with a well behaved spectra in the NIR were selected. The characteristic of the standard stars used is presented in Table 3.5 and their SED are presented in Appendix A.

The final step is to assemble the flux measurements (the photometry) from the 21 filters together in a so called *flux table*. The flux table is the final product obtained by the MPIAPHOT package. This table contains, among others, the position in world coordinates, the flux and the magnitude in each filter and their respective errors for each object of the catalogue. The derived flux table has the same structure as the optical R-band based flux table derived by Wolf et al. (2003), where a description of the flux table content is given.

3.16 Calibration Between Different Wavebands

A relative calibration among the different optical wavebands was ensured by using only a few spectrophotometric standard stars in the A901-field by Wolf et al. (2003). Spectra of those standard stars were carried out in a photometric night and connected to published standard stars (Oke 1990). In this way, spectrophotometric standards were available in every single exposure of the survey and no further calibration was required regardless of the photometric conditions under which the regular imaging was carried out.

3.17 Magnitude Limit

The depth reached in each filter has been calculated and is represented by Fig. 3.17. The Figure shows the magnitude error versus the magnitude for all objects with errors below $0^m.1$ ($10-\sigma$) in the Y, J1, J2 and H filter. The $10-\sigma$ magnitude limit reached is 22.0 in the Y filter, 21.5 in the J1 filter and 21.0 in the J2 and H filter. These error plots are useful to diagnostic hidden problems in the data reduction. Ideally, the data points form a parabola shape for which the position of the vertical branch vary according to the depth of the survey. The thickness of the branch (the scatter) is due to the unequal depth reached in the different subfields. The

scatter is larger in the Y-band due to the unequal depth reached in different subfields, see Tab. 3.4. The minimum error reached for bright objects which form the horizontal part of the parabola is given by the photon noise. The scatter at the bright end of the Y, J1 and J2 photometry is due to the FPN which couldn't be removed better. While not perfect the result is acceptable.

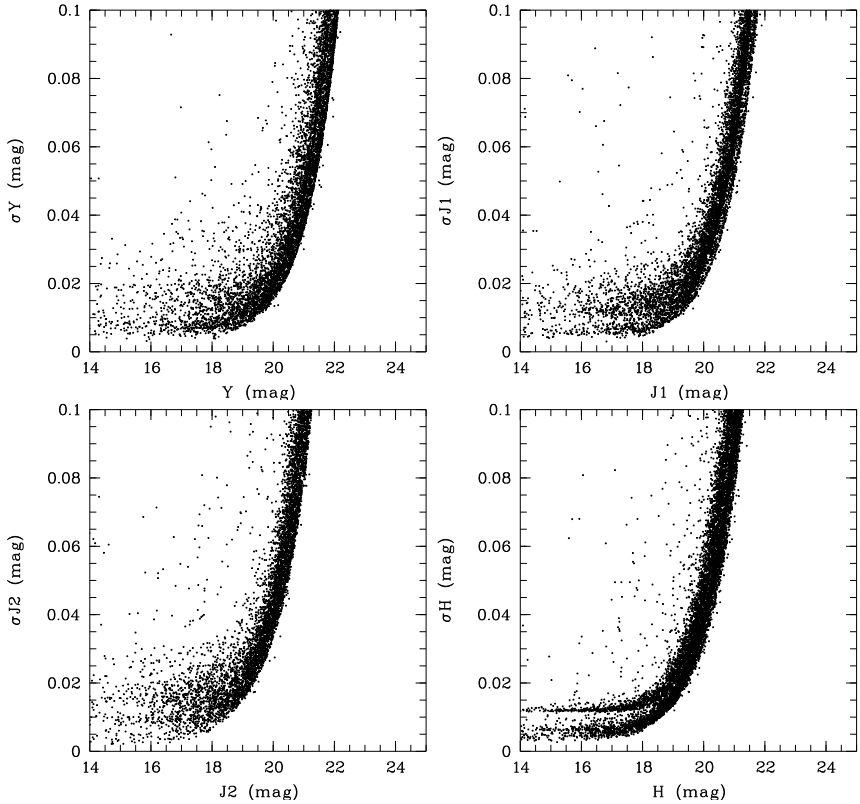

Figure 3.17: Error versus Vega magnitude for objects belonging to A901-subfields A, B and C in the COMBO-17+4 NIR bands.

3.18 Colour Calibration with Main Sequence Stars

For a reliable multi-colour classification it is necessary to input objects having well calibrated colours, otherwise an object having faulty (offsetted) colours will be misclassified. Thus, prior to the classification, the colours indices calibration has been checked by comparing the colours indices of the point sources in our A901 catalogue with the star colours from the Pickles (1998) spectral library. The latter is also used in the classification process, thus the star colours from the library should be consistent with the star colours in our catalogue.

The main sequence stars, due to their well determined surface temperatures, lie in predefined regions in colour-colour plots. The calibration check involves a visual comparison of

colour-colour plots for all point sources of our catalogue which have a magnitude 13<H<18. Very bright point sources which have a high S/N are used since their scatter is small in the colour-colour plots due to their small fluxes errors. There are 552 point sources in our catalogue which were used for the colour calibration, all of which have been pre-classified as stars by SExtractor. Figure 3.18 shows a selection of colour-colour plots using the NIR colours. Any calibration error from our catalogue would appear as an offset in the x or y direction relative to the library data point. The colour-colour plots shown in Fig. 3.18 have been colour calibrated and show that our data points (black) closely match those of the template (red). The colour correction values applied to match the colours from our catalogue to the spectral template are listed in Tab. 3.6. The colour corrections are relative to the R-band which is our zeropoint established with spectrophotometric stars. For certain colours such as U-B and I-J_1 a colour error threshold as been applied. The colour error threshold for the U-B colour is due to the U-band which cannot be better calibrated than a tenth of a magnitude. The colour error threshold for the I-J_1 comes form the relative calibration between optical and NIR which has a limited accuracy in the order of 7%. This visual colour calibration check with the help of Fig. 3.18 allows us to detect a colour shift of the order of $\gtrsim 0^m.02$ which gives a lower limit on the performance of the multi-colour classification.

3.19 Astrometry

The astrometry has been performed to obtain real sky coordinates for the objects in our catalogue which up to now were in internal coordinates. The astrometry was performed with IRAF (Tody 1993) using the 2MASS point sources catalogue. In the A901 field there are ~800 bright (H$\lesssim$16) stars in common with the 2MASS catalogue. Both catalogues have been matched and a very good astrometric accuracy of $0.1''$ in RA and DEC has been achieved.

The photometry achieved one have in hands flux and magnitude in 21 filters for each objects in our catalogue. In order to analyse the stellar population in galaxies at different redshift, one must obtain the objects photometric redshift and spectral energy distribution. The next chapter go briefly through the object classification process and SED template fitting, via the colours, to assign a redshift, an SED and a class to each object in the catalogue.

Subfield	Filter	Observation date	Integration time (sec)	Seeing arcsec	Campaign name
A901a	H	December 2005	2520	1.00-1.35	242
	H	December 2007	4200	0.85-1.35	256e
	H	December 2007	1500	1.13-1.50	256d
	H	January 2008	1380	0.89-1.06	257
	H	March 2008	1500	0.76-0.93	257c
	J2	December 2005	1120	1.13-1.24	242
	J2	December 2006	2960	0.89-1.24	250
	J2	January 2008	1440	1.06-1.30	257
	J2	March 2008	1600	0.82-1.50	257c
	J1	December 2005	1400	1.29-1.46	242
	J1	February 2006	1700	1.15-1.34	244
	J1	December 2007	3600	0.96-1.29	256e
	J1	April 2008	1900	1.01-1.50	257d
	Y	December 2005	1600	1.11-1.23	242
	Y	December 2007	1500	1.13-1.45	256d
	Y	December 2007	1600	1.16-1.42	256e
	Y	January 2008	1300	1.24-1.50	257
	Y	March 2008	1500	1.23-1.39	257c
	Y	April 2008	1400	0.86-1.12	257d
A901b	H	December 2005	1500	1.07-1.45	242
	H	February 2006	1500	0.80-1.15	244
	H	December 2007	4500	0.84-1.23	256e
	H	December 2007	1500	1.09-1.44	256d
	H	January 2008	1500	0.90-1.16	257
	H	April 2008	1800	1.19-1.50	257d
	J2	December 2005	2240	1.08-1.46	242
	J2	December 2006	2560	1.02-1.27	250
	J2	January 2008	1920	1.10-1.50	257
	J1	December 2005	1000	1.19-1.50	242
	J1	February 2006	1000	1.36-1.50	244
	J1	December 2007	3500	0.97-1.33	256e
	J1	April 2008	1800	1.04-1.17	257d
	Y	December 2005	1600	1.11-1.23	242
	Y	December 2007	1200	1.15-1.50	256e
	Y	January 2008	1000	1.26-1.50	257
	Y	March 2008	1400	1.12-1.50	257c

Table 3.2: Observations A901-field (April 2008)

Subfield	Filter	Observation date	Integration time (sec)	Seeing arcsec	Campaign name
A901c	H	December 2005	1020	1.10-1.50	242
	H	December 2007	5880	0.82-1.42	256d
	H	December 2007	1500	1.13-1.35	256e
	H	March 2008	1500	1.07-1.38	257c
	H	April 2008	1500	0.85-1.10	257d
	J2	December 2005	3120	1.03-1.21	242
	J2	February 2006	1600	1.29-1.48	244
	J2	January 2008	2160	1.12-1.50	257
	J2	April 2008	1600	0.94-1.22	257d
	J1	December 2005	1700	1.18-1.47	242
	J1	December 2007	1800	0.86-1.03	256d
	J1	December 2007	3500	1.09-1.28	256e
	J1	April 2008	1800	1.12-1.35	257d
	Y	December 2005	1600	1.00-1.27	242
	Y	December 2007	1600	0.91-1.14	256d
	Y	December 2007	1600	0.84-1.20	256e
	Y	March 2008	1600	0.86-1.31	257c

Table 3.3: Table continued: Observations A901-field (April 2008)

Filter	Subfield A	Subfield B	Subfield C	Subfield D	Goal (1×10^3 s)
Y	8.9	5.2	6.4	1.1	8
J1	8.6	7.1	8.3	1.3	8
J2	7.1	7.4	8.5	5.3	12
H	11.8	12	11.1	0.8	12

Table 3.4: Total NIR integration time for each A901-subfields (April 2008)

Catalogue Number	Name	R.A h:m:s	DEC d:m:s	mH ABmag	mR ABmag	Spectral Type	Associated subfield
12416	A901_11	09:56:41.432	-09:59:33.11	18.4	19.2	wF5 V	A
18792	A901_14	09:56:34.416	-09:54:47.19	18.7	19.5	wF5 V	A
14134	A901_21	09:56:01.891	-09:58:11.48	16.9	17.8	wF8 V	B
14571	A901_22	09:55:59.392	-09:57:41.04	15.2	16.2	rF8 V	B
15322	A901_23	09:55:49.459	-09:57:14.07	16.6	17.4	wF8 V	B
19275	A901_24	09:56:13.159	-09:54:33.75	16.9	17.8	wF8 V	B
03500	A901_35	09:56:41.672	-10:10:04.70	19.4	20.3	wF8 V	C
08237	A901_31	09:56:44.198	-10:03:12.40	18.7	19.7	wF8 V	C

Table 3.5: Standard star characteristics. The star spectral template library from Pickles (1998) is used for the objects classification thus the spectral type for the standard stars can be determined. The spectral type with the prefix 'w' indicates metal-weak abundance and the prefix 'r' indicates metal-rich abundance, all stars belong to the main sequence, spectral type F of luminosity Class V.

Colour Index	Colour Correction CD mag	Threshold CD mag	Colour Index	Colour Correction CD mag	Threshold CD mag
U-B	-0.02	0.100	643-R	+0.03	
B-V	0.02		R-697	0.00	
V-R	-0.06		752-I	-0.01	
R-I	-0.03		816-I	+0.03	
418-B	0.00		I-856	0.00	
B-464	-0.05		I-915	-0.03	
486-V	-0.02		I-J_1	+0.03	0.07
520-V	-0.05		Y-J_1	-0.046	
573-R	-0.05		J_1-J_2	+0.05	
605-R	+0.01		J_1-H	+0.05	

Table 3.6: Colour correction values which allow a good match between colours from point source objects from our A901 H-band catalogue and the colour from Pickles (1998) spectral star library. Colour indices: Letters denote the broad-bands and numbers represent the central wavelength of medium-band filters measured in nanometres.

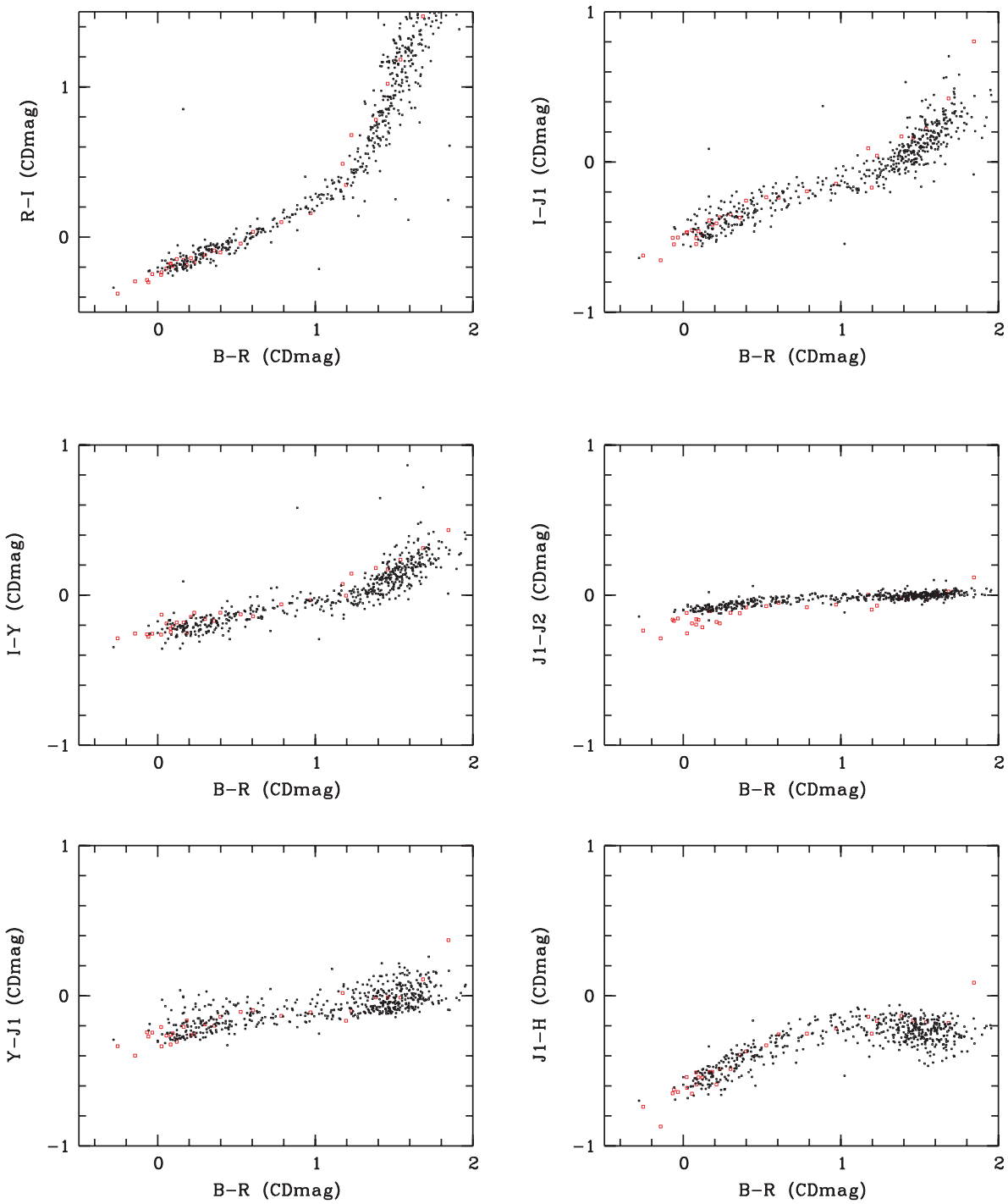

Figure 3.18: Comparison between point source objects from the A901 H-band catalogue (black) and the main sequence stars from the Pickles (1998) spectral library (Red). Colours are given in CD magnitude, see §4.1.

Chapter 4

Classification by SED Templates Fitting

This chapter explains the multi-colour classification scheme and presents the results obtained from a classification using the full optical plus NIR photometric data set of the A901-field. Prior to the classification it is necessary to calculate the colours and calibrate them. Then, the objects classification can be performed using star, galaxy and QSO templates. The first part of this chapter introduces the colour indices and the classification scheme, the second part compares the classification obtained for the new H-band catalogue with the previous R-band catalogue obtained with optical data only in the frame of the COMBO-17 survey.

4.1 Colour Indices

The colour indices are used for the calibration tests with the main sequence stars (see §3.18) and for the objects classification. The colour index is simply the difference in magnitude measured in two different filters. In the Vega magnitude system, if A and B are two different filters, the colour index is:

$$A-B \equiv m_A - m_B = -2.5log\frac{\int_0^\infty d\lambda S_\lambda(A) f_\lambda(Obj,A)}{\int_0^\infty d\lambda S_\lambda(B) f_\lambda(Obj,B)} + 2.5log\frac{\int_0^\infty d\lambda S_\lambda(A) f_\lambda(Vega,A)}{\int_0^\infty d\lambda S_\lambda(B) f_\lambda(Vega,B)} \quad (4.1)$$

where S_λ is the combined sensitivity of the telescope, CCD and filter. However, the spectrum of the star Vega has a non-trivial shape on a physical flux scale and as a consequence the colour indices values cannot directly be converted into physical flux ratios. Based on the CADIS survey experience and since the flux values obtained at the end of the data reduction process are naturally expressed in units of *photons* per $(m^2 \cdot sec \cdot nm)$, another magnitude system, the CD magnitude, was introduced by Wolf et al. (2001b). The CD magnitude system is defined as:

$$CDmag = -2.5logF_{phot} + 20^m.01 \quad (4.2)$$

where F_{phot} is in *photons* m^{-2} s^{-1} nm^{-1}. An object which has F_{phot}=constant has all CD colours equal to zero. The CD magnitude system has its zero point at λ_0=548 nm with $m_{CD}=m_{Vega}$ one find that an object with V≈20 has a flux of 1 γ m^{-2} s^{-1} nm^{-1} at λ_0. Thus the colour indices input in the multi-colour classification are in units of CD magnitude defined as:

$$A - B \equiv m_A - m_B = -2.5log\frac{F_{phot,A}}{F_{phot,B}} \tag{4.3}$$

and the error is,

$$\sigma_{m_A - m_B} = \sqrt{(\sigma_{F_{phot,A}}/F_{phot,A})^2 + (\sigma_{F_{phot,B}}/F_{phot,B})^2} \tag{4.4}$$

For more details about different magnitude system such as the Vega, AB, ST and CD systems used in astronomy see Wolf et al. (2001b). Magnitudes are calculated in order to obtain colours, but for low flux level (especially for F<0) the conventional logarithmic magnitude system is inappropriate. Thus, alternatively, approximation like "Asinh" magnitude and the "upper limit" magnitude were also calculated. The Asinh magnitude system was introduced by Lupton et al. (1999) to deal with low flux objects and the upper limit magnitude has been introduced by Meisenheimer et al. (in prep 2009) as an alternative to the Asinh magnitude, §4.5 deals more in detail with problems encountered during the conversion in magnitude from objects with low flux measurements.

Having the photometry in 21 different filters in hand, it is possible to use a wide range of different colour indices for the classification. We have used the same optical colours used in the previous classification done for the optical only COMBO-17 survey plus the new NIR colours derived from the COMBO-17+4 survey. The set of colours indices include the standard colours derived from broad-band filters such as U-B, B-V, V-R and R-I and a series of colours derived from a mix of narrow-band and broad-band such as 418-U, R-697, etc. The new colours derived by the NIR photometry are I-J_1,Y-J_1,J_1-J_2 and J_1-H. The colours have been chosen to be the difference between a shorter wavelength and a longer wavelength and the narrow-bands are always linked to a broad-band. Table 3.6 contains the 20 colours used for the classification.

4.2 The Classification Scheme

The multi-colour classification was developped by Wolf (1998) in the frame of the CADIS survey. Here only a brief overview is given. More details about the classification scheme are available in Wolf et al. (2001a) and Wolf et al. (2001b). The global scheme of the object classification and redshift determination is to compare and match the observed colours of each individual object from our deep H-band sources catalogue with a colour library of objects with known spectra. The objects are classified by locating them in colour space and com-

paring the probability for each class to generate the given measurement. The multi-colour classification first assigns a class between star, galaxy, QSO or strange object for each individual astronomical source. For extragalactic sources like galaxies and QSOs, the multi-colour classification estimates a redshift and its error. The object class as well as the redshift and its errors are determined using the maximum-likelihood (ML) and the minimum error variance method (MEV) estimator. Using colours indices instead of fluxes in the classification process allows us to avoid absolute calibration for each waveband used. Wolf et al. (2001a) has shown that the use of the colour indices as an input to the classification rather than the fluxes themselves are equivalent under the condition that the fluxes used to calculate the colours are well calibrated with each other. As discussed in §3.16 a relative calibration among the different optical wavebands was ensured by establishing few spectrophotometric standard stars in the A901-field. The performance of the classification relies on colours accuracy which relies on the relative calibration among the different wavebands. Since the calibration among the different wavebands cannot be better achieved than a few percent (2%-3% according to the scatter in the data point on Fig. 3.18), the performance of the classification is limited by a systematic uncertainty of this order which is the assumed minimum error for the colour indices. Table 3.6 shows the minimum error assigned for different colour indices.

4.3 Colour Libraries

The colour libraries are constructed from observed or synthetic spectral libraries which contain the object SED on which we convolve the transmission of the telescope optics, the CCD quantum efficiency and a given filter transmission efficiency and thus derive synthetic photometry and colours. Four colour libraries are used by the classification process, two are for stars, one for galaxies and one for QSOs, each of them contain the 20 colours indices used in the COMBO-17+4 surveys.

4.3.1 Star Libraries

The star colour library was derived from the Pickles (1998) stellar spectral library. This spectral library contains 96 stars of spectral types F, G, K and M of luminosity classes from I to V. Unfortunately even though the spectra were formed by combining data from several sources overlapping in wavelength coverage from UV to IR, the NIR ($\lambda\lambda$ ~1000nm-1500nm) range is covered for only a few spectra in the library. Due to the lack of NIR data the remaining spectra of the library have been inter- or extrapolated in the NIR regime. Nevertheless, Zatloukal (2008) have shown that this star library gives a more reliable classification than other star libraries like the Decline (priv. communication) library.

The second star library containing more peculiar blue types of stars like white dwarfs (WD), blue horizontal branch (BHB) stars and sub-dwarfs. The second star library is derived from theoretical spectra from Koester (priv. communication). Those two star libraries have also been used for the COMBO-17 survey.

4.3.2 Galaxy Spectral Library

The new feature in the classification process is the use of a new galaxy template library developed by Meisenheimer et al. (in prep 2009). This new galaxy library differs from the one used previously by Wolf et al. (2003), which is based on a single burst model with reddening, and consists of an improvement of the templates based on a two burst-model derived by Borch et al. (2006) which could not reproduce accurate redshift. The motivation of a two-burst model was to be able to better reproduce the star formation history for the wide range of galaxy types from Starbursts to Ellipticals. The second burst model allows a mix of old and young stellar populations, since old stars generally dominate the mass while young stars dominate the optical flux, it is important to be able to constrain their relative amount from the SED to better estimate the stellar mass-to-light ratio M/L of a galaxy. The new galaxy library was calculated with the PEGASE package (Fioc & Rocca-Volmerange 1997), a synthesis population model. The spectral galaxy library includes galaxy templates of 60 different ages from 50 Myr to 15 Gyr times 6 levels of extinction from 0 to 0.5 by steps of 0.1. The template involves a Kroupa IMF and an initial metallicity of 0.01 (that is half solar Z/Z_o=0.5) and is extinction-free. The extinction is applied afterwards as a screen following the SMC law defined by Pei (1992). Steps in redshift cover the range from 0 to 2.3 with a resolution of 0.005 on a log(1+z) scale. The SFR follows two exponential declines, the first one occurred several billion years ago with an e-folding time of 1 Gyr and a second burst started 2750 Myr after the first burst with an e-folding of 0.1 Gyr.

4.3.3 QSO Library

The same QSO templates library as for the COMBO-17 survey has been used. The QSO colour library was derived from the SDSS template spectrum by Vanden Berk et al. (2001). The resulting QSO colour library covers redshifts between 0.3<z<2.02 with a redshift resolution of 0.01 in log(1 + z). For QSO below z=0.3 the templates do not cover adequately the NIR wavelength range and consists of a smooth continuum model. For those QSO the fit during the classification is less well constrained than at higher redshift. As assumed in the frame of the COMBO-17 survey, we do not expect many QSO at z<0.5 and thus this problem should not affect greatly our results in that low redshift regime. More details about the design of the QSO library can be found in Wolf et al. (2004).

4.4 Classification Results

The classification was performed on the A901 deep H-band source catalogue, optimum results were obtained with the 20 colours listed in Tab. 3.6. A classification has been achieved for all objects of the A901-field catalogue. This consists of 31747 objects classified into 29492 galaxies, 169 QSOs, 1871 stars and 215 strange objects. The histogram of the photometric redshift distribution for 12023 galaxies with H<21.5 is shown in Fig. 4.1, the sharp peak centred at z=0.165 indicate the super cluster A901/A902, composed of ∼800 members. The performance of the classification itself is beyond the scope of this thesis since it requires Monte-Carlo simulation to understand the behaviour of the classification for very faint H-band selected sources. Here we assume that the classification is reliable for all objects down to an observed magnitude of H=21.7, which is our 5-σ magnitude limit for point sources.

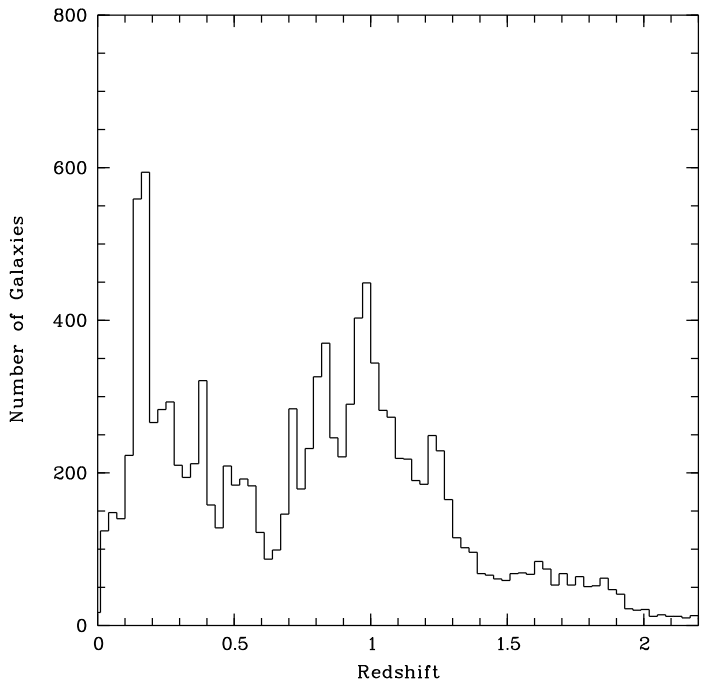

Figure 4.1: Histogram of the photometric redshift distribution for 12023 galaxies with H<21.5 between 0<z<2 in the A901-field.

The distribution of the different galaxy SED types of the catalogue as a function of redshift is shown in Fig. 4.2. We see an overdensity caused by the A901 cluster centred at z=0.165 forming a vertical line. The cluster includes galaxies of almost all SED types. We also see that the average SED for galaxies located between 1.5<z<2 is around SED #30. This SED #30 is composed of 83% of old stars and 17% of young star which are younger than 250 Myr according to our 2 burst model, more details about template SED will be available in Meisenheimer et al. (in prep 2009).

In Figure 4.2 we also see the lack of star forming blue galaxies with SED type between 1 to 20 at z>1 (below the blue dotted line) due to our H-band selected catalogue biased towards red objects. The red dotted line in Figure 4.2 shows a natural cut in the old SED template with redshift, as redshift increases we find less and less old red galaxies.

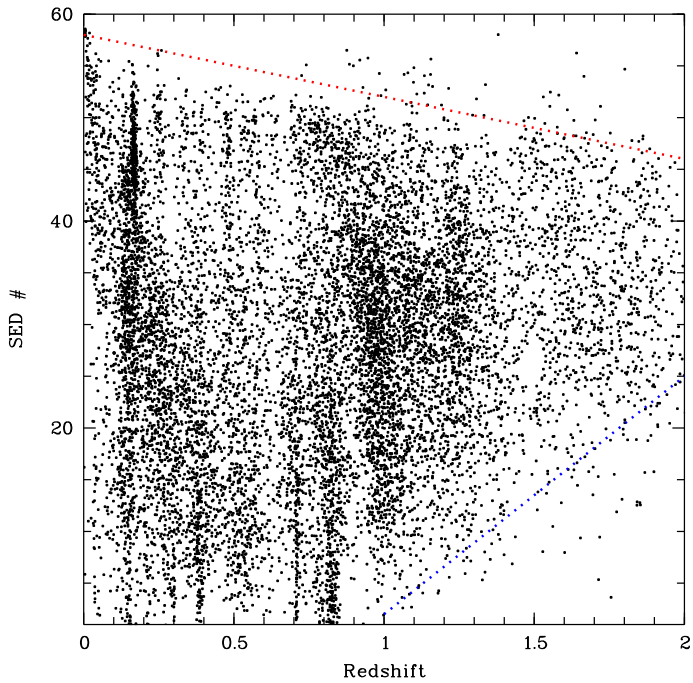

Figure 4.2: SED types as a function of redshift for galaxies with H<21.5 between 0<z<2. The Y axis goes from SED template #1 for young stellar population starburst to SED #60 for old stellar population elliptical.

4.4.1 Comparison of the COMBO-17 Catalogue with the COMBO-17+4 Catalogue

The photometric redshift distribution obtained with the H-band selected catalogue (red) is compared with the one previously obtained with the optical R-band catalogue (black) in Fig. 4.3. The histograms show for both catalogues the redshift distribution for galaxies located in the subfield A, B and C of the A901-field. The left panel shows the entire redshift distribution between 0<z<2, with the black line representing 14697 galaxies with R<24.5 from the R-band catalogue and the red line representing 12023 galaxies with H<21.5 from the H-band catalogue. One sees that the main cosmological structures can be recognized in both catalogues. The right panel in Fig. 4.3 shows a close-up view of the redshift distribution between 1<z<2, we clearly see the benefit of the addition of the NIR bands at high redshift. While the number of objects in the optical catalogue decreases drastically between 1<z<1.35 the number of objects in the H-band catalogue decreases smoothly. Between 1<z<2 the optical catalogue contains

2157 galaxies with R<24.5 while the optical plus NIR catalogue contains 3821 galaxies and since the redshift determination for z>1.1 in the optical data set is very uncertain, we have gained more than ∼1600 objects between 1<z<2 by using a combination of optical+IR data.

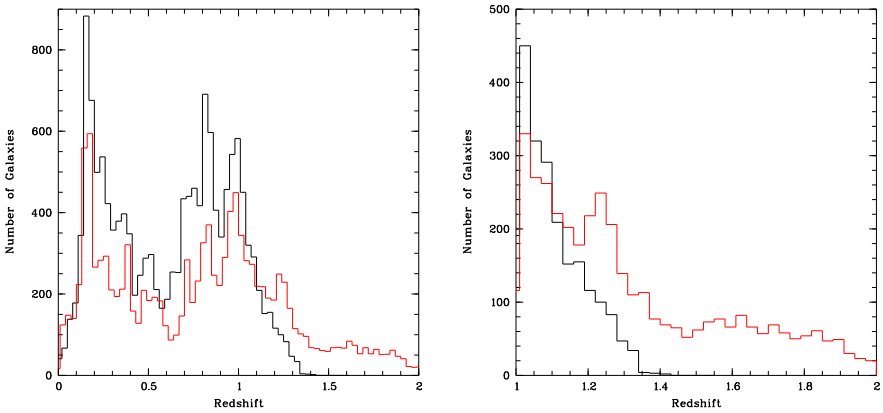

Figure 4.3: Left: Histogram of galaxy photometric redshift distribution between 0<z<2. Comparison between R-band selected catalogue R<24.5 (black) and the H-band selected catalogue H<21.5 (red), only objects present in both catalogues are compared. Right: Histogram of galaxy photometric redshift distribution between 1<z<2. The gain in number of objects with the NIR catalogue compared to the optical catalogue is substantial.

It is interesting to compare the distribution of the different galaxy SED templates type in the R-band selected catalogue with the one in the H-band selected catalogue. Figure 4.4 shows two histograms of the number of objects having a certain SED type, from young stellar population starburst (SED #1) to old stellar population elliptical (SED #60). One sees that for the low redshift slice between 0<z<1 the H-band catalogue is biased toward redder SED types, the catalogue contains much less star forming blue galaxies with 1<SED#<30 than the R-band selected catalogue. For intermediate galaxy templates between 30<SED#<40 both catalogues are equivalent but for redder galaxies with 40<SED#<50 the H-band catalogue contains much more objects. The number of very red and old galaxies with SED>#50 follows the same decreasing trend in both catalogues. At higher redshift, between 1<z<2, Figure 4.4 right panel, the gain of redder objects with SED>#20 in the H-band selected catalogue is clearly visible; while the number of galaxies with SED#>20 drops in the R-band catalogue, it increases in the H-band catalogue reaching a peak around SED#30. The H-band selected catalogue which contains much more red galaxies than the optical R-band selected catalogue allows us to better trace the old stellar population in galaxies.

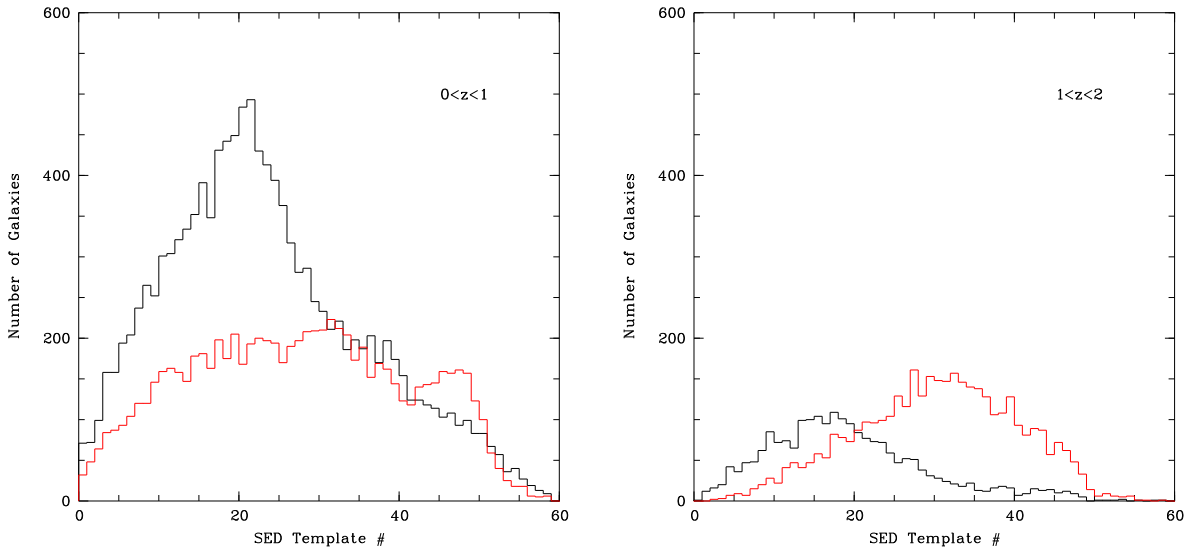

Figure 4.4: Comparison between different SED types in the A901 R-band catalogue (black) and the H-band catalogue (Red) for two different redshift slice. SED #1 refer to Starburst and SED #60 refer to Elliptical.

4.5 Low Flux Count and Redshift Focusing

In photometric redshift determination, it important to avoid any redshift focusing which could lead to erroneous scientific results. A redshift focusing occurs when many objects are assigned systematically to the same given redshift due to one or more wrong colours. For objects having high flux in a given band, the colours have been calculated using magnitude as described by Eq. 4.3. When objects have low flux or even negative flux in a given band the magnitude as been calculated using the Asinh magnitude (Lupton et al. 1999). The Asinh magnitude is a modified magnitude system which replaces the logarithm in the conventional definition of a magnitude with an inverse hyperbolic sine function. For high flux values (S/N>5) the function is logarithmic but in the low flux regime (S/N<5) the Asinh magnitude is a linear approximation of the conventional magnitude and thus avoids having negative magnitude. This prescription is useful when considering the colours of faint objects, since the difference of two Asinh magnitudes measures the usual flux ratio for bright objects and avoids the problems caused by dividing two very uncertain values for faint objects. Unfortunately this redefinition of the magnitude system has lead to redshift focusing in our case since we are using classification colours which are calculated using a mix of broad- and medium-bands. The medium-bands data are less deep than the broad-band data and thus the magnitude at which the Asinh magnitude system starts to be linear will be different for the medium band compared to the broad-band. As a consequence, it could be that a colour is calculated using on one side the Asinh magnitude for the medium-band flux measurement and the other side the conventional magnitude for the measurement in the broad band. The result is that the medium

band will appear brighter that it is in reality introducing wrong colours to the classification process and creating a redshift focusing at a given redshift, see Fig. 4.5. To avoid the redshift focusing created by the use of the Asinh magnitude we have used the upper-limit magnitude system introduced by Meisenheimer et al. (in prep 2009). The upper-limit magnitude system is a new magnitude definition for low flux level which is approximately given by:

$$m = 20 - 2.5log(F_{phot} + 2\sigma) + 2\sigma(mag) \tag{4.5}$$

where σ are the errors in flux and in mag. In Eq. 4.5 the upper limit starts to be effective for objects which have a S/N of 0.5 instead of S/N of 5 in the Asinh magnitude avoiding low flux objects from the medium-band having erroneously high calculated value.

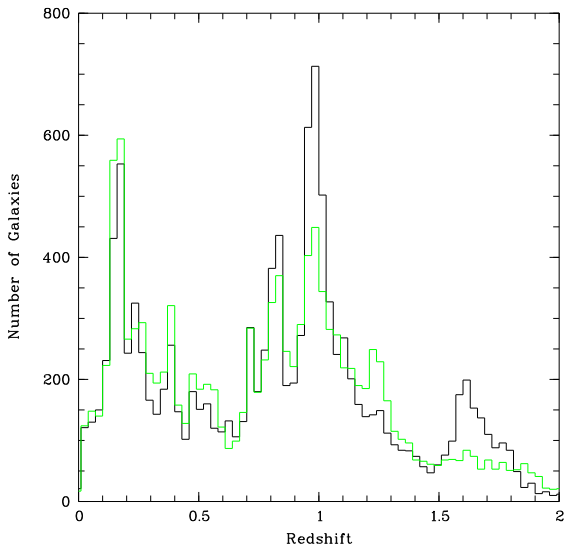

Figure 4.5: Distribution of redshift resulting from a classification using Asinh magnitude (black) compared to upper-limit magnitude (green), a redshift focus appears at z∼1 and z∼1.6 when using the Asinh magnitude system, the objects create two artificial peaks at those redshifts.

4.6 Improving Photometric Redshift with NIR Data

The implementation of NIR data to the optical COMBO-17 survey allowed a considerable improvement in the determination of photometric redshift for objects which were at the limit of the classification reliability in the R-band catalogue derived by the optical COMBO-17 . Figure 4.6 shows the comparison between the photometric redshifts z_{opt} based on the 17 optical bands against the ones on optical plus NIR data $z_{opt+NIR}$ for 7682 galaxies common in both catalogues. We see that the majority of the galaxies form a diagonal branch up to z∼1.4 (black dots). A small spread for z_{opt}<0.7 means that the redshifts are determined by the

optical data only and are equivalent in both catalogue. For z_{opt}>0.7 the diagonal become broader indicating the redshift discrepancy between redshifts based on optical data only and the ones based on extended NIR data. It is interesting to see how much the determination of the photometric redshift is improved by extending the wavelength coverage from the optical to the NIR. In Fig. 4.6 one can sees one prominent group off the diagonal branch located between 0.7<z_{opt}<1.1 (red dots). For these objects we obtained a significantly higher redshift from the measurements based on the extended data set when compared with the results obtained with optical data only. This group contained 753 out of 7682 galaxies meaning that about 10% of the studied population has a significant improvement in the redshift determination when one supplements the optical bands with the NIR bands. Another group of galaxies (blue dots) are classified at high redshift between 1.5<$z_{opt+NIR}$<2 with the optical plus NIR data while they were classified at low redshift between 0<z_{opt}<0.4 with the optical only data set. This group contains 39 out to 7682 galaxies representing 0.5% of the sample and have very faint magnitude R>22 and large errors in the optical photometry, the redshift determination is not accurate in both catalogues. Figure 4.6 also shows that the diagonal is broader at all redshifts and a group of 99 objects (in green) which represent 1.2% of the sample is classified at lower redshift by the use of the NIR compared to the optical data. This effect could be due to the classification using the new galaxy templates in the case of the optical plus NIR data.

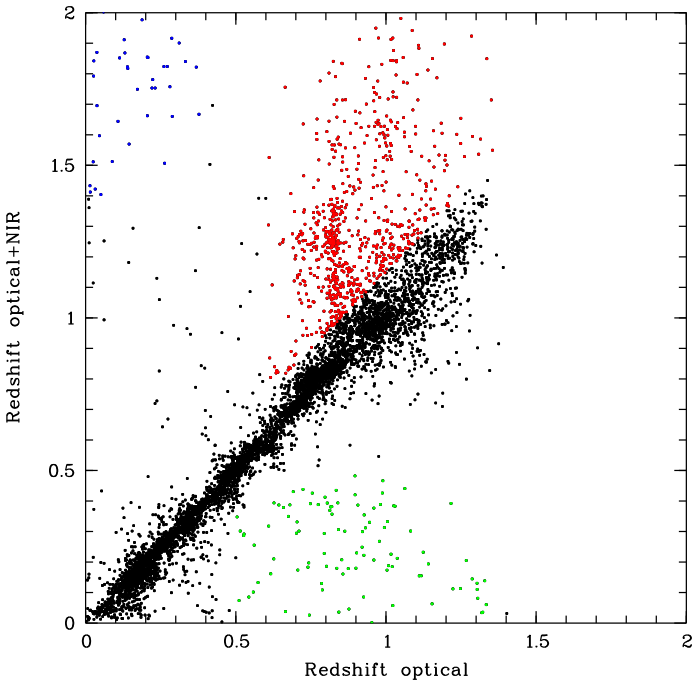

Figure 4.6: Photometric redshift comparison between optical data only and optical+NIR data for 7682 galaxies located in the subfield A, B and C of the A901-field. The magnitude cut for the optical COMBO-17 catalogue is R<24.5 and H<21.5 for the optical plus NIR COMBO-17+4 catalogue.

Three example of SEDs of galaxies classified with the optical data in 17 filters compared to a classification with optical plus NIR data (21 filters) are shown in Fig. 4.7, Fig. 4.8 and Fig. 4.9 . Those galaxies are good example of the galaxies belonging to the group in red dots in Fig. 4.6. On the bottom panel of each figures one sees that the photometric redshift assigned to those galaxies by the classification using only optical data was in the range 0.7<z<1.1 while they are in reality at much higher redshift, in the range of 1.2<z1.5, when the NIR are added, top panels.

For example in Fig. 4.7 while using the optical data only (bottom panel) the classification estimates the redshift of the galaxy to be z=0.73 because the 4000Å break is thought to be around λ=6900Å. With the addition of the NIR data points, we now see that the 4000Å break is in reality around λ=9200Å (top panel) resulting in a redshift of z=1.3. In Fig. 4.8 (bottom panel) the galaxy is classified at redshift z=0.8 using the optical data only when in reality this object is at z=1.28 (top panel) with the 4000Å break located around λ=9100Å. In Fig. 4.9 (bottom panel) the galaxy is thought to be around z=1.1 but in fact the 4000Å break is in the NIR at λ=10120Å resulting in a redshift of z=1.53 for this galaxy. By comparing the two SEDs in Fig. 4.7, 4.8 and 4.9 we see that the optical data in fact reaches only the beginning of the 4000Å break for such objects and that the classification using only the optical data is mistaken.

The redshift accuracy has been checked for the A901 galaxy cluster. In Figure 4.10 we compare the photometric redshift obtained for the cluster members with the optical data (R<23.5) and the photometric redshift obtained with the full optical plus NIR data set (H<21.5). Based on spectroscopy, the A901 galaxy cluster is centred at z=0.165 with a dispersion of 0.155<z<0.175. In Figure 4.10, the left panel shows the comparison of the photometric redshift obtained for the A901 cluster with the COMBO-17 versus the COMBO-17+4 data set, the *blue* diagonal indicates the z_{opt}=$z_{opt+NIR}$ line. If both data sets had produced the exact same redshift all objects would have been on the *blue* diagonal line. Instead the data points follow the *red* line with an offset of ∼0.005, meaning that the new redshift derived with the optical plus NIR data set is 0.005 lower than the one obtained with the optical data set. This result is very good since the redshift determined by the photometric redshift based on optical data for the A901 cluster were by ∼0.005 to high compared to spectroscopy. The right panel in Fig. 4.10 shows an histogram of the number of objects as a function of redshift for the A901 galaxy cluster with the optical data set (shown in *blue*) peaking at z=0.17+/- 0.03(1+z) and the optical plus NIR in *red* peaking at z=0.165+/- 0.03(1+z) which is the spectroscopic redshift. Fig. 4.10 shows that the redshift accuracy obtained with the photometric redshift using the optical plus NIR data is excellent and comparable to spectroscopy for low redshift galaxies.

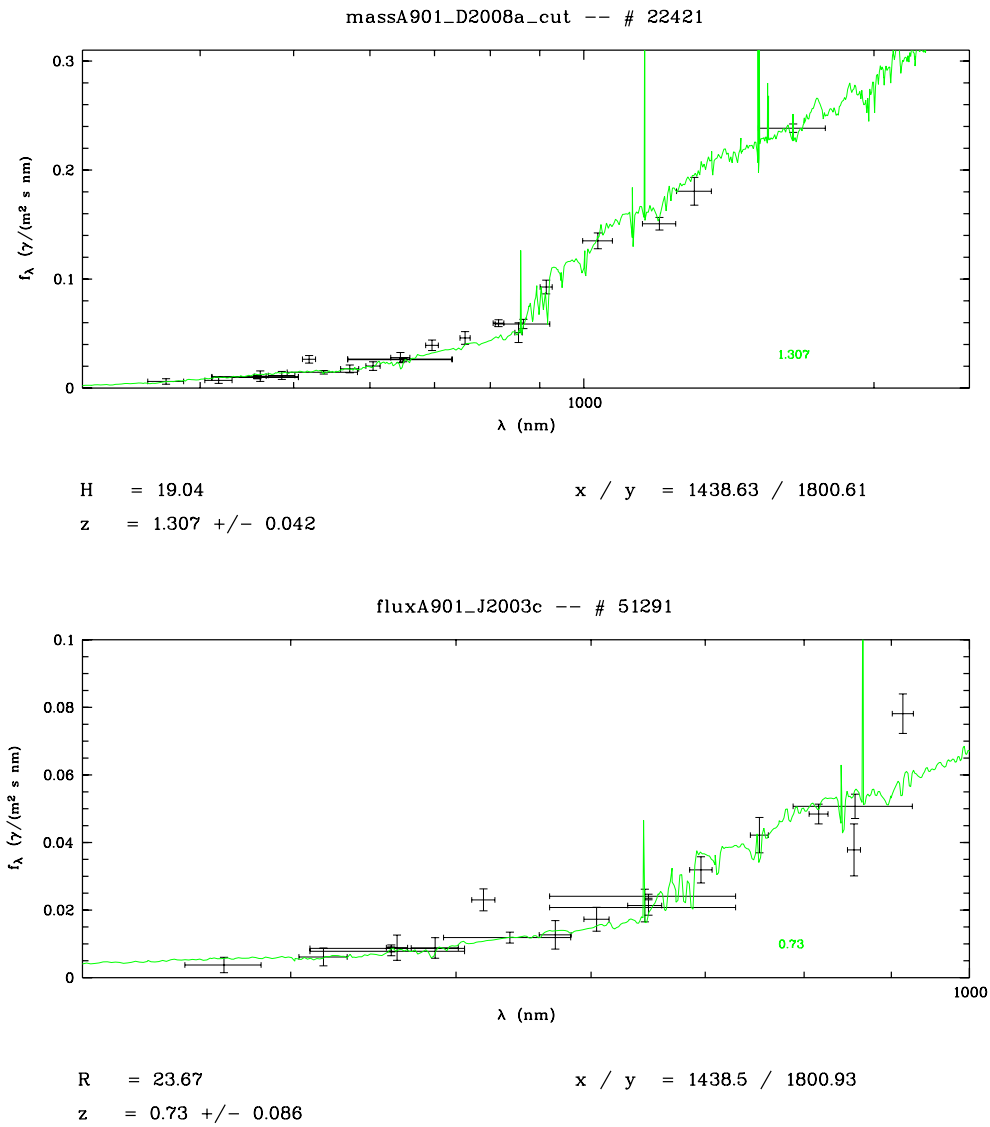

Figure 4.7: Spectral energy distribution in $photons/(m^2 \cdot s \cdot nm)$ for a galaxy classified with 17 optical plus 4 NIR bands (top) compared to a classification with 17 optical bands only (bottom). The data points are shown in black, the galaxy template in green. Redshift z, magnitude H or R and x,y world coordinates are given.

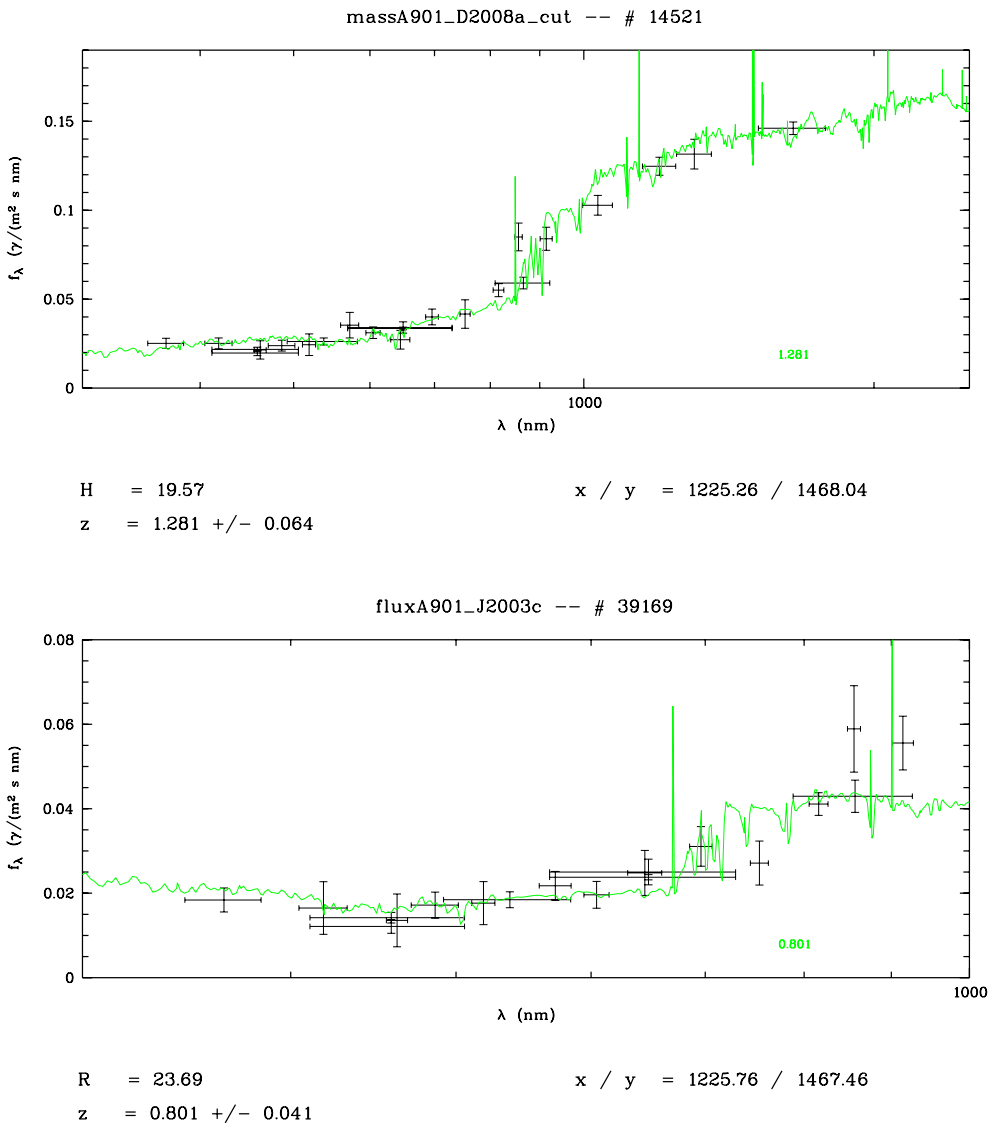

Figure 4.8: Spectral energy distribution in $photons/(m^2 \cdot s \cdot nm)$ for a galaxy classified with 17 optical plus 4 NIR bands (top) compared to a classification with 17 optical bands only (bottom). The data points are shown in black, the galaxy template in green. Redshift z, magnitude H or R and x,y world coordinates are given.

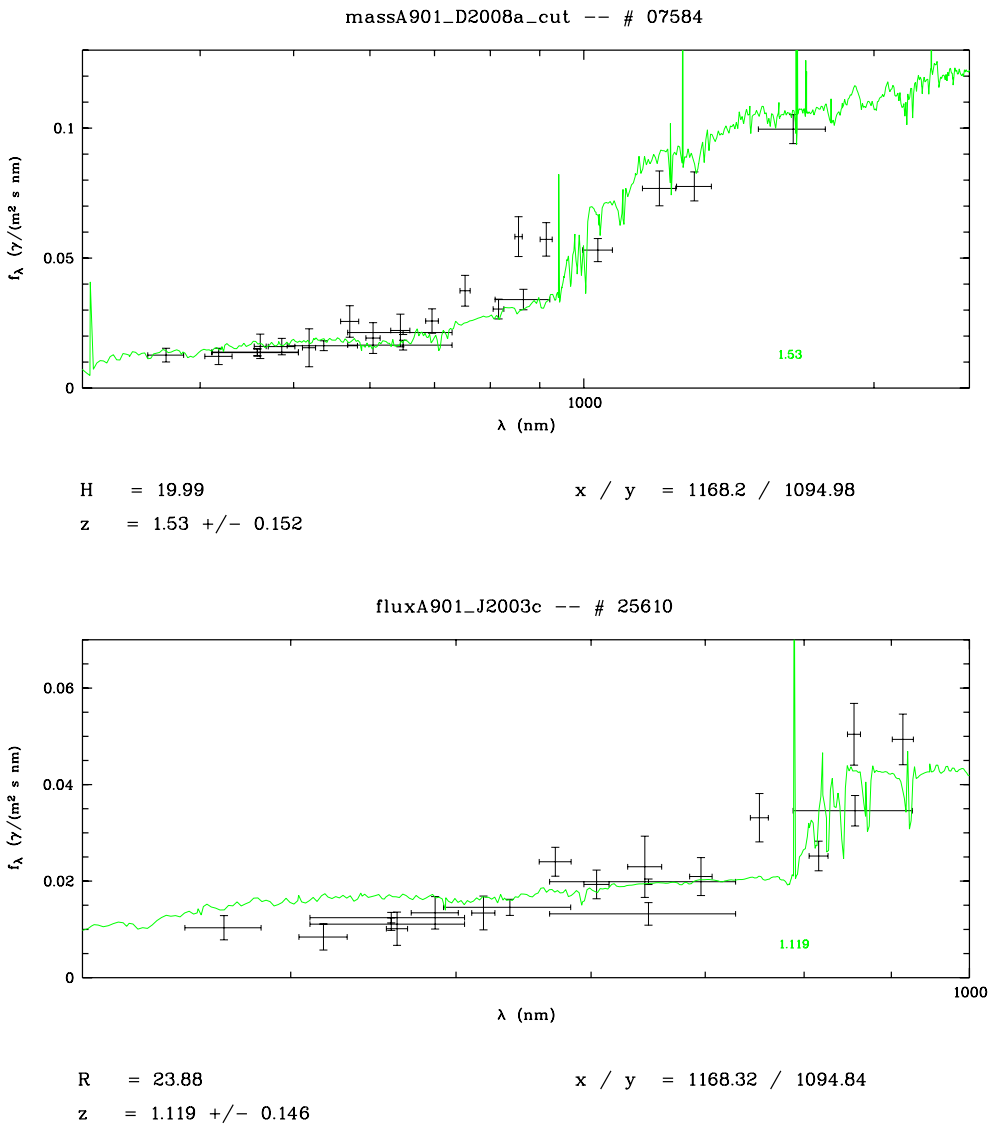

Figure 4.9: Spectral energy distribution in $photons/(m^2 \cdot s \cdot nm)$ for a galaxy classified with 17 optical plus 4 NIR bands (top) compared to a classification with 17 optical bands only (bottom). The data points are shown in black, the galaxy template in green. Redshift z, magnitude H or R and x,y world coordinates are given.

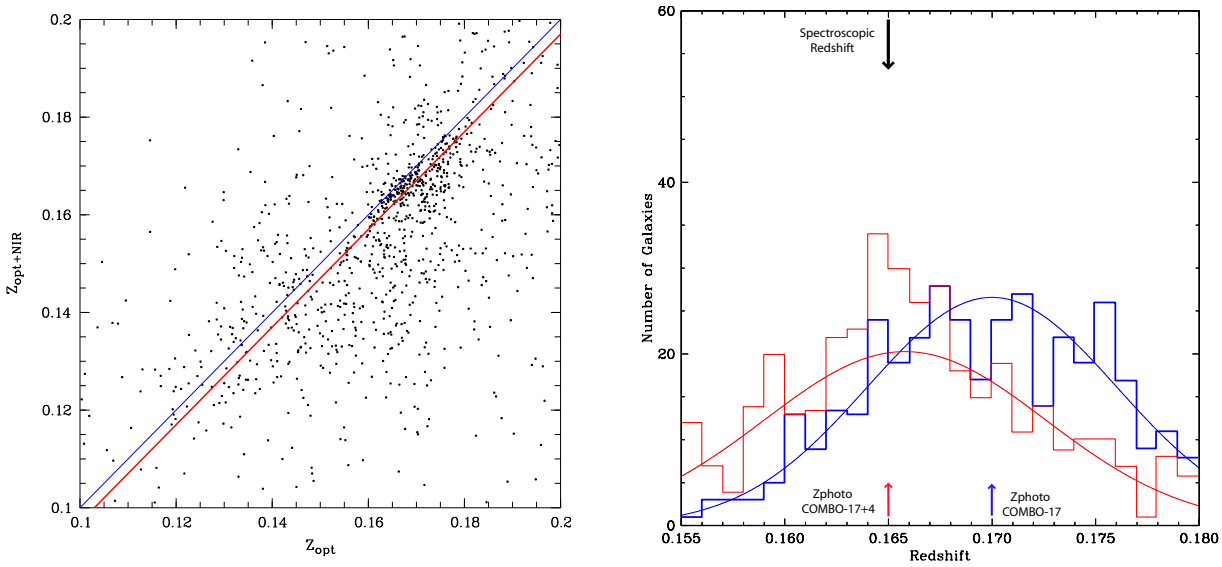

Figure 4.10: Left: Comparison of photometric redshift obtained with optical data set and optical plus NIR for the A901 galaxy cluster. Right: Redshift distribution for the A901 cluster R-band selected catalogue (in blue) and the H-band selected catalogue (in red). Photometric redshift obtained for each catalogue and spectroscopic redshift are indicated.

Chapter 5

Galaxy Bimodality Through Cosmic Time

This chapter investigates the bimodality of galaxies through cosmic time. For this aim the rest-frame magnitudes and the rest-frame colours are computed and colour-magnitude diagrams as well as colour distributions are analysed. This analysis leads to the determination of a colour-magnitude relation evolving with redshift to separate the red galaxies from the blue ones out to z=2. By separating the star forming blue galaxies from the red evolved galaxies, it is possible to separately study the evolution of the two populations through cosmic time. Throughout this chapter the cosmological parameters Ω_m=0.3, Ω_λ=0.7 and H_0=70.7 km/s/Mpc are assumed and all magnitudes are given in the Vega system.

5.1 Rest-Frame Magnitudes and Colours

Rest-frame luminosities have been calculated from the observed photometry which covers the wavelength range from the U- to the H-band. For comparison with other work, rest-frame luminosities have been obtained for several passbands in different photometric systems including the classic U-, B- and V- bands in the Johnson system as well as the u-, g-, r- and i- bands from the Sloan Digital Sky Survey (SDSS), and finally a synthetic UV continuum band, named U_{280}, centred at $\lambda = 280nm$ with $FWHM = 40nm$ and a *top-hat* transmission curve. The rest-frame luminosities and colours are calculated in three steps:

•As seen in §1.3 the rest-frame features in a galaxy spectrum move through our observed bands with redshift, see Fig. 1.3. In the first step, the flux in the rest-frame band of interest has to be calculated from the observed flux in the closest broad-band filter. This is done by using a *k-correction colour table*, which is derived from the templates in the spectral galaxy library. The k-correction colour table contains observed versus rest-frame colours for the entire set of observed broad bands and the above set of rest-frame bands on a grid of 360 template SEDs (60 SED types × 6 extinction levels) and 240 redshift steps in the range $0 < z < 2.3$. For each observed galaxy the *observed* magnitude in the rest-frame band is derived with respect

to the nearest observed broad-band. Table 5.1 gives the range of wavelengths in which each of the observed broad-band filters U, B, V, R, I, J1 and H is used to derive the *observed* magnitude in the rest-frame band (centred on λ_c) shifted to $\lambda_o = (1+z)\ \lambda_c$. As an example, for a galaxy at z=0.5, the rest-frame flux in the V Johnson filter centred at $\lambda_c = 550\,\mathrm{nm}$ is observed at a wavelength of $\lambda_o = (1+z)\ \lambda_c = 825\,\mathrm{nm}$. According to Tab.5.1 the rest-frame V flux of this object is based on the flux observed in the I-band which is used for the range $760 < \lambda_o < 1050\,\mathrm{nm}$. In this step the interstellar extinction $A_{\lambda_{obs}}$ towards Abell 901 in the observed broad-band centred on λ_{obs} is taken into account.

λ_{min} (nm)	Filter	λ_{max} (nm)	A_λ
280	U	400	0.29
400	B	500	0.22
500	V	570	0.18
570	R	760	0.15
760	I	1050	0.11
1050	J1	1400	0.07
1400	H	2600	0.05

Table 5.1: Broad-band filters used to calculate rest-frame luminosities. For each filter the wavelength range is given in which the filter is used to calculate the flux in a rest-frame band, the central wavelength λ_c of which is shifted to $\lambda_o = (1+z)\ \lambda_c$, that is $\lambda_{min} < \lambda_o < \lambda_{max}$. In addition, the assumed extinction values towards A901-field are listed.

•Second, for each galaxy, the absolute magnitude defined by Eq. 1.5 is calculated from the *observed* rest-frame magnitude and the luminosity distance as defined by Eq. 1.6. In this step also the correction between "aperture magnitudes" which are used in the photometric flux table and the total (integrated) magnitude of a galaxy has to be taken into account. The correction Δm_{tot} is derived from the total magnitude MAG-BEST derived by SExtractor on the deep H-band image and calibrated for each of our subfield A, B and C such that for stars (aperture = total magnitude) and $\Delta m_{tot} = 0$.

The luminosity errors include three components added in quadrature: the error of the magnitude of the observed broad-band filter closest to the redshifted rest-frame band, the error of MAG-BEST and a minimum error of 0.03 to take into account redshift errors and overall calibration uncertainties.

•Third, from the absolute magnitudes in the rest-frame, the rest-frame colours are calculated straightforwardly. The error in rest-frame colour is the quadratic addition of the errors of the two involved broad-band filters plus a minimum error which ranges between 0.05 and 0.1 depending on the location of the two rest-frame bands involved in typical galaxy spectra (that

is: rest-frame colours between two smooth regions of galaxy spectra get a smaller minimum error).

To investigate the bimodality of galaxy colours we use the U_{280}-V rest-frame colour because the U_{280} band provides a cleaner measure of the flux short-wards of the 4000Å break than the Johnson U-band which partly overlaps with the break and thus is strongly affected even by very small uncertainties in the redshift determination. Moreover, these two photometric rest-frame bands are bracketed by our observed bands in the entire redshift range of interest $0.3 < z < 2$ which is most essential for our present study and contains the bulk of galaxies in our sample. So, in using U_{280}-V we do not rely on any SED extrapolation.

Before investigating the bimodality of galaxies it is interesting to analyse the distribution of galaxies in the rest-frame magnitude redshift plane for the rest-frame magnitude used to calculate the U_{280}-V colour. The left panel in Fig. 5.1 shows the redshift as a function of the rest-frame magnitude in the Johnson V-band. The magnitude limit H<21.7 of the survey appears at the faint end of the distribution as a parabola shape. The horizontal features represent overdensities, clearly showing the A901 cluster at z=0.165 which spreads over almost all the magnitude range. The distribution reaches fainter magnitudes for objects located below z=0.38 due to the fact that at those redshift the rest-frame M_V is calculated from the flux emitted in the observed R-band which is our deepest optical data. The Fig. 5.1 right panel shows the redshift as a function of the rest-frame $M_{U_{280}}$, showing a step between 1<z<1.7 in the faint end of the distribution. In this redshift range the rest-frame $M_{U_{280}}$ is calculated from the flux observed in the deep R-band and thus allows us to see galaxies at fainter magnitudes. The two redshifts associated with the beginning and the end of the step in the distribution indicate at which redshift the rest-frame flux in the U_{280} passes from an observed band to another one, just below z=1 the rest-frame U_{280} flux comes from the observed V-band, while above z=1.7 it comes from the I-band.

The U_{280}-V colour and its error as a function of redshift are plotted in Fig. 5.2. By plotting the colour as a function of redshift, Fig. 5.2 left panel, shows the same trends as discussed previously for Fig. 4.2 which shows the SED types as a function of redshift. This is due to the colour of a galaxy being directly linked to its spectral type. A star forming galaxy is called blue because it has more flux at shorter wavelength sampled here by the U_{280} filter than at longer wavelength sampled here by the V filter. This means that star forming blue galaxies have smaller U_{280}-V colours than later type elliptical galaxies and are located in the lower part of both figures Fig. 5.2 left panel and Fig. 4.2.

The U_{280}-V colour errors have been plotted as a function of redshift in the right panel of Fig. 5.2. This plot shows the cut created by the minimum error threshold of $0^m.1$ applied

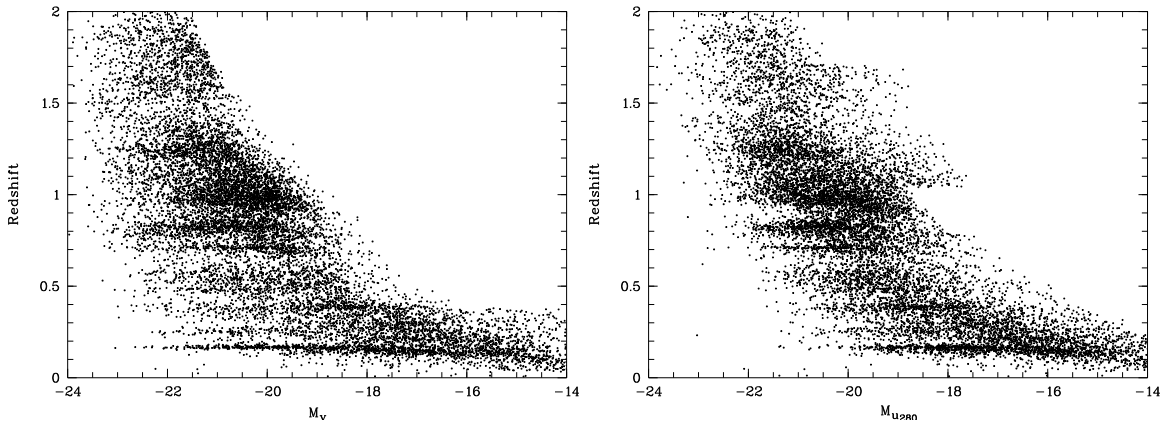

Figure 5.1: Absolute magnitude M_V (left) and $M_{U_{280}}$ (right) as a function of redshift. On the right panel we see that the faint end of the distribution is not smooth but shows a step between 1<z<1.7 due to the observed flux from our deep R-band which is used to calculate the rest-frame $M_{U_{280}}$ in that redshift range.

in the calculation of the colour error. We also see that the colour accuracy is very good for objects located at low redshift z$\lesssim$0.6 where most of the objects have a colour error close to the minimum threshold of $0^m.1$. The large scatter between $0.9\lesssim z \lesssim 1.2$ is caused by the magnitude error σM_V in the V-band which is larger than the magnitude error $\sigma M_{U_{280}}$ in the U_{280}-band for that redshift range. This is due to the fact that for this redshift range M_V is calculated using the flux observed in the narrow-band J1 while $M_{U_{280}}$ is calculated based on the flux in the deep R-band. The J1 filter being narrow and not as deep as the R-band, the uncertainties associated to the magnitude in this band are larger than in the deep R-band. In Fig. 5.2 we also see that the colour uncertainties are larger at z>1.5 due to the error in the rest-frame $M_{U_{280}}$ caused by the large error in the shallow I-band flux.

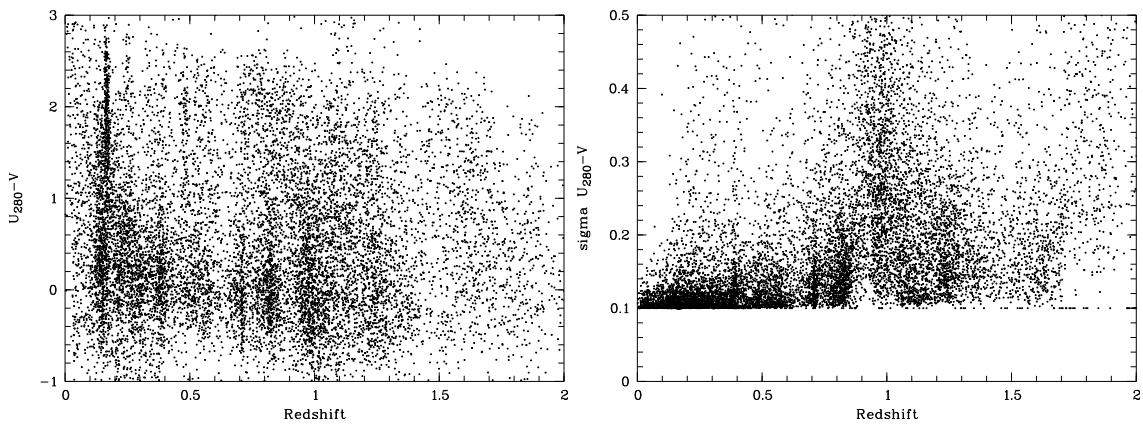

Figure 5.2: Rest-frame U_{280}-V colour (left) and his error (right) as a function redshift.

5.2 Rest-frame Colour Bimodality

A magnitude limited sample of 14286 galaxies with magnitude H<21.7 (Vega) has been used to investigate the colour bimodality of galaxies through cosmic time. This magnitude limit corresponds to the 5$-\sigma$ detection limit in the H-band in the aperture flux.

In the literature, colour-magnitude and colour-colour diagrams as well as colour histograms are generally used to separate the star forming blue galaxies from the red galaxies since the two galaxy populations lie in predefined regions of those plots, examples are shown in Fig. 5.7 and Fig. 5.8. The top left panel in Figure 5.7 shows the U_{280}-V versus M_V colour-magnitude diagram (CMD) for the A901 galaxy cluster. For a galaxy cluster like A901, a red sequence is clearly visible in the CMD. However, it could be difficult to see a clear separation between the red sequence and the blue cloud for a sample of galaxies located in a less dense environment or for a sample of galaxies in the field, see Fig. 5.8. Moreover, the colour errors could produce a large scatter in the CMD making it difficult to visually distinguish a well defined red sequence. As we have seen in the previous section, the errors in the U_{280}-V measurements are larger above z$\sim$1, making it difficult to investigate the bimodality in a CMD for a high redshift galaxy sample. To investigate the galaxy colour bimodality through cosmic time, we have developped a new method based on error weighted histograms in which each galaxy is represented by its gaussian probability distribution ($p \sim e^{-(c-c_0)^2/2\sigma_c}$) where σ_c is the colour error and the p is normalized so that $\int pde$=1. Using this definition, a galaxy with a small error have a gaussian distribution with a more pronounced peak that a galaxy having a large error and having a flatter distribution. The error weighted histograms are created by summing all the gaussian distributions at a given colour for a given redshift bin. The galaxy having a small error contributes more significantly to the overall distribution than a galaxy having a large error. To investigate the galaxy bimodality we have used the U_{280}-V colour. However in order to better disentangle the red sequence from the blue cloud we have tilted the U_{280}-V colour in the colour-magnitude plane using $M_V = -20$ as the pivot point Eq. 5.1. That is, the measured $U_280 - V$ of each individual galaxy is projected along the slope of the red sequence (as determined in the A901 cluster CMD, see Fig. 5.7 top left) to the pivotal magnitude $M_V = -20$. This new method allows us to investigate the distribution of the galaxies in many thin redshift slices of about Δz$\sim$0.1 throughout our full redshift range between 0<z<2.

$$(U_{280} - V)_{Mv=-20} = (U_{280} - V) + 0.3(M_V + 20) \tag{5.1}$$

Some examples of the distribution of galaxies in different thin redshift slices are shown in Figure 5.3. The redshift interval and mean as well as the number of objects in the entire redshift slice are indicated on each panel. In each panel we see two distinct peaks appearing due to the galaxy bimodality. On each histogram the right peak represents the distribution of the red galaxies while the left peak represents the distribution of the star forming blue

galaxies. As a reference we see the A901 cluster in the top left panel, a clear red sequence peak is visible and the contribution of the blue cloud galaxies forms a double peak due to the contribution of only few blue galaxies. Our results show a clear galaxy bimodality at z<1, see Fig. 5.3 top right and bottom left panels, as also demonstrated by Bell et al. (2004b) using the COMBO-17 data for the combined A901, A226 and S11 fields. The bimodality has been found at z<1 by many other surveys including SDSS (Strateva et al. 2001) and DEEP (Weiner et al. 2005). Moreover, the depth of our survey allows us to extend the detection of the galaxy bimodality up to z=1.6 which is the z_{mean} of our highest redshift interval where we can still detect two distinct distribution peaks. Beyond z=1.6 it is not possible to confirm a galaxy colour bimodality since the number of objects available for our analysis drops considerably between 1.6<z<2, see Fig. 5.6. Figure 5.4 bottom panel shows the distribution for 198 galaxies in the redshift interval 1.65<z<1.75, the distribution is clearly not bimodal. However this does not mean that the red sequence does not exist beyond z=1.6, here we can only argue that due to the small area surveyed and the low number of objects in our sample at z>1.6 our data does not allow us to confirm or refute the presence of a red sequence beyond z=1.6. Our results are consistent with other studies which confirm a galaxy colour bimodality at high redshift, up to z∼1.2 by the MUSYC survey (Taylor et al. 2008) and up to z∼1.5 by the VVDS survey (Franzetti et al. 2006). While the COMBO-17+4 survey allows us to increase the redshift limit of the colour bimodality detection compared to those later studies, it does not allow us to see a defined galaxy red sequence at z=2 as found by Kriek et al. (2008) using NIR spectroscopy. Williams et al. (2008) using UKIDDS Ultra-Deep Survey photometric data have also found a bimodality up to z=2 in rest-frame U-V versus V-J colour-colour plots.

Astonishingly, while investigating the galaxy bimodality in different redshift slices of the Universe for our A901-field, we have found that for some redshift slices even at low redshift (e.g. z_{mean}=0.25) and intermediate redshift (e.g. z_{mean}=0.99) a red sequence is absent, see Fig. 5.4 top panel left and right. This result seems to contradict the results obtained by Bell et al. (2004b) who found a galaxy bimodality at all redshifts up to z∼1. In fact Bell et al. (2004b) derived his results from a sample of ∼ 5000 galaxies derived from the combination of the A901, A226 and S11 fields which are three COMBO-17 fields while our data includes only the 3/4 of the entire A901-field. Consequently, our data are much more sensitive to large scale structures. Hence, the A901-field has in some redshift intervals voids where no red sequence appears. This was not observed by Bell et al. (2004b) since those results, by combining several fields together, averaged the galaxies bimodality distribution in a given redshift range. Our results show that a pronounced red sequence strongly depends on the surveyed part of the Universe. This is a new result which never has been demonstrated in the literature before and need certainly more investigation. Further studies should investigate what the density of the galaxy environment has to be in order for a red sequence to emerge.

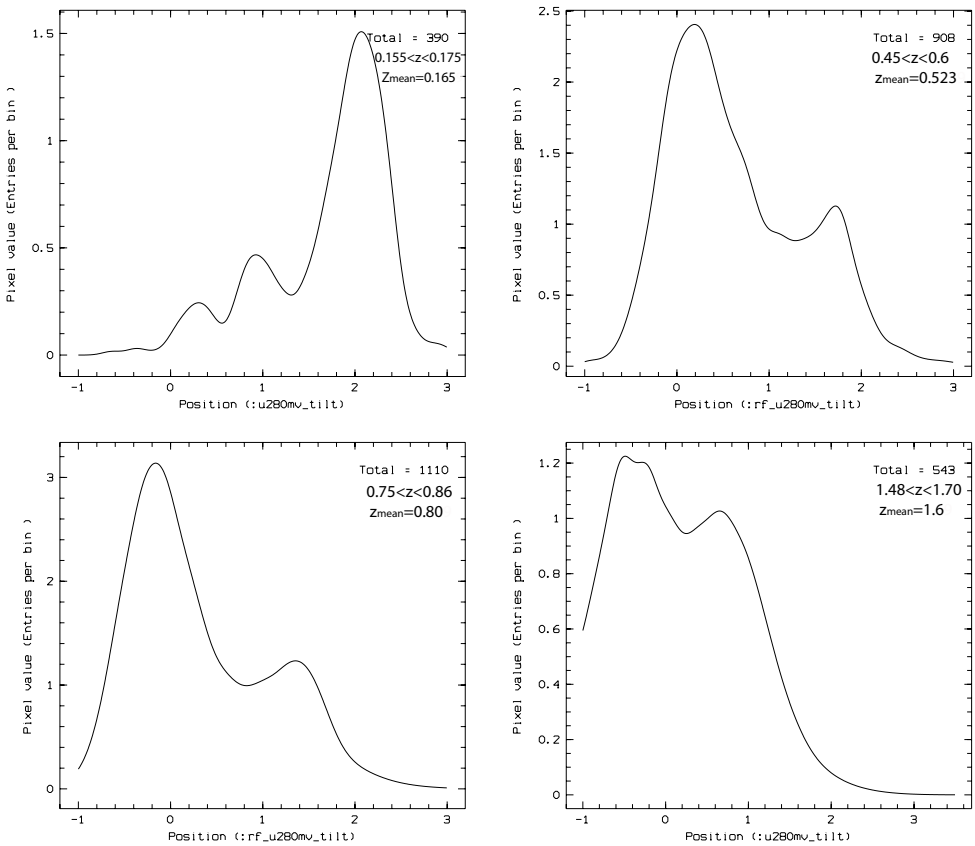

Figure 5.3: Rest-frame $(U_{280} - V)_{Mv=-20}$ colour distribution for galaxies in different redshift slices. In each panel, the histogram is built by the addition of all single galaxies which are represented by their gaussian probability distribution based on their colour error. The total number of galaxies used to produce the histogram (top right in each panel) represents the integral of the distribution over the colour range. In each histogram we see a bimodality, the right peak represents the red sequence galaxies and the left peak represents the blue cloud galaxies. The top left panel shows the colour distribution for the cluster A901 at z=0.165 the red sequence forms a sharp peak while the few galaxies belonging to the blue cloud forms a double peak.

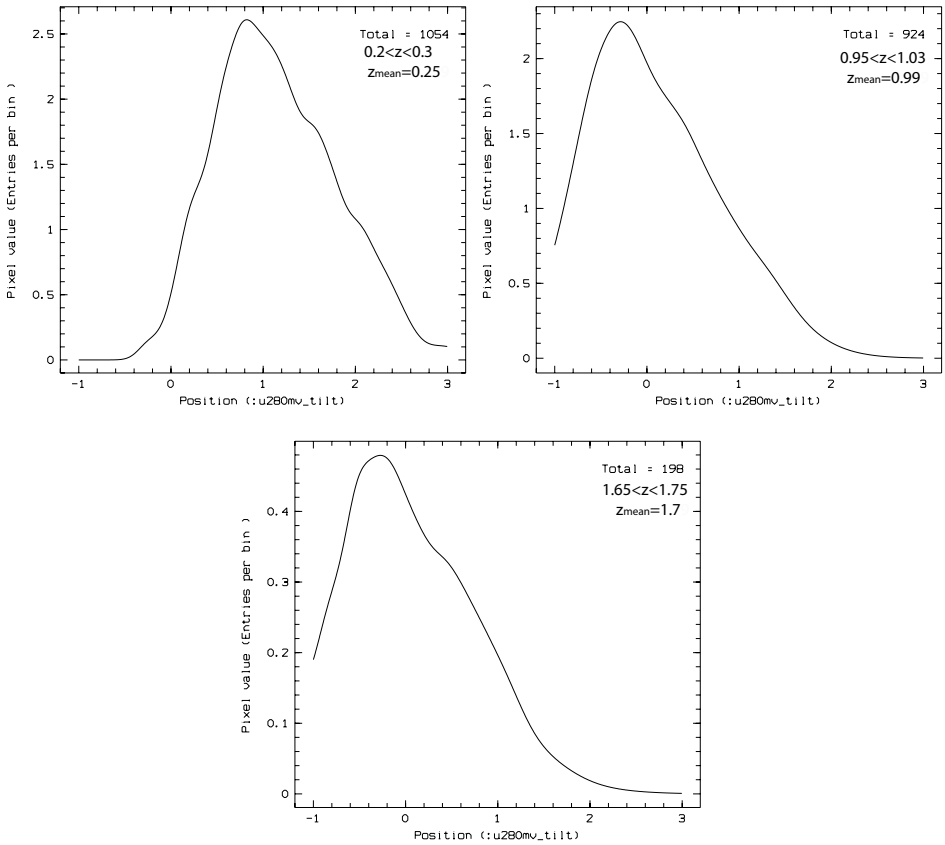

Figure 5.4: Rest-frame $(U_{280} - V)_{Mv=-20}$ colour distribution for galaxies in different redshift slices, see also caption Fig. 5.3. The number of galaxies included in the distribution as well as the redshift interval and mean redshift are given in the top right of each panel. The distribution of galaxies does not show a clear bimodality in those redshift intervals, neither at low $z_{mean} = 0.25$ (top left panel) nor at intermediate $z_{mean} = 0.99$ (top right) as compared to high $z_{mean} = 1.7$ (bottom) redshift.

5.3 Colour Magnitude Relation

Since the red sequence is missing in the redshift interval 1.6<z<2, our data allow us to derive an evolving colour-magnitude relation to separate the red galaxies from the blue ones up to z=1.6. Using error weighted histograms for many thin redshift slices, the $(U_{280} - V)_{Mv=-20}$ colour position of the red galaxies distribution peak has been followed from z=0 to z=1.6. Using the mean redshift z_{mean} of each redshift slice, the corresponding lookback time has been calculated using Eq. 1.4. Figure 5.5 shows the rest-frame colour $(U_{280} - V)_{Mv=-20}$ as a function of lookback time, showing that the colour evolves linearly with time by:

$$(U_{280} - V)_{Mv=-20} = 2.57 - 0.195 \times t_{lookback} \tag{5.2}$$

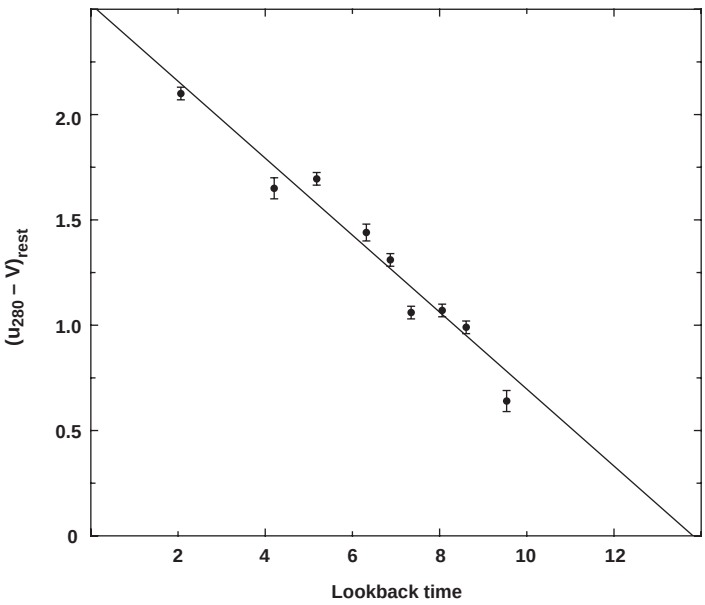

Figure 5.5: Evolution of the red sequence bright end colour $(U_{280} - V)_{Mv=-20}$ with lookback time in Gyrs.

Accordingly, the $(U_{280}-V)_{Mv=-20}$ colour positions of the red sequence as a function of lookback time have been linearly fitted and using the approximation $t_{lookback} \simeq 15Gyrs \cdot z/(1+z)$ a redshift evolving colour-magnitude relation has been established for the position of the red sequence distribution peak. This is the first time that a linear evolution of the red sequence with time has been derived, previous studies due to large uncertainties in the red sequence position were unable to derive such a meaningful relation.

Having determined this relation, we chose a parallel relation which is 0.47 mag bluer in order to separate the red and blue galaxy populations. The derived redshift evolving colour-

magnitude relation to separate the red galaxies from the blue galaxies is defined as:

$$(U_{280} - V)_{limit} = 2.10 - 0.3(M_V + 20) - 2.92z/(1 + z) \tag{5.3}$$

From Eq. 5.3 we define a galaxy to be red if its colour is $(U_{280} - V) > (U_{280} - V)_{limit}$ and a galaxy is defined as blue if its colour is $(U_{280} - V) < (U_{280} - V)_{limit}$. The evolving colour-magnitude relation Eq. 5.3 has been compared with the one derived by Bell et al. (2004b) with a sample of galaxies up to z=1 from the COMBO-17 optical data. In order to compare our results the relation Eq. 5.3 has been expressed as a function of redshift instead of lookback time such as $(U_{280} - V)_{limit} = 1.70 - 0.3(M_V + 20) - 1.03z$ and using the colour relation $(U - V) = 0.28 + 0.43(U_{280} - V)$ from our galaxy templates we have $(U - V)_{limit} = 1.01 - 0.13(M_V + 20) - 0.44z$. Our result is very close to the one derived by Bell et al. (2004b) where $(U - V)_{limit} = 1.15 - 0.08(M_V + 20) - 0.31z$, our relation is slightly steeper than the one derived by Bell et al. (2004b), but its translated into a minor colour difference of <0.1 mag in the galaxies relevant magnitude range -23<M_V<-18.

Using the evolving colour-magnitude relation Eq. 5.3 the red galaxies which have $(U_{280} - V)>(U_{280} - V)_{limit}$ can be extracted of our galaxy sample. The histogram in Fig. 5.6 shows the redshift distribution of the red sequence galaxies among all types of galaxies of our sample having a limited magnitude H<21.7. There are 3943 red galaxies out of 14286 between 0<z<2 in our sample and 1122 red galaxies out of 4640 between 1<z<2. Our sample consists of an unprecedented large sample of red galaxies between 1<z<2 allowing us to investigate their evolution from high redshift to the present day.

5.4 Colour-Magnitude Diagrams up to z=2

Having in hand a robust method to separate the red galaxies from the blue one as a function of lookback time, it is possible to see how both galaxy populations evolve in colour and magnitude since z=2 by plotting CMDs for different redshift slice of the Universe. The colour-magnitude diagrams $(U_{280} - V)$ versus M_V for ten redshift slices are shown in Fig. 5.7 and Fig. 5.8. On each panel the green line indicates the bimodality separation derived from Eq. 5.3, since the mean redshift of the slice is used to plot the separation line, some galaxies above the green line belong to the blue cloud while some galaxies below the line belong to the red sequence, the real separation is represented by the colour of the data points. The top left panel in Fig. 5.7 shows the CMD for the A901 cluster centred at z=0.165, such a dense environment shows a clear red sequence on the CMD and is given as a reference. The red sequence is not as sharp and easy to visually distinguish in CMDs beyond z=1 especially in the redshift slice 1.07<z<1.19 due to the scatter caused by the relatively large colour uncertainties, see Fig.

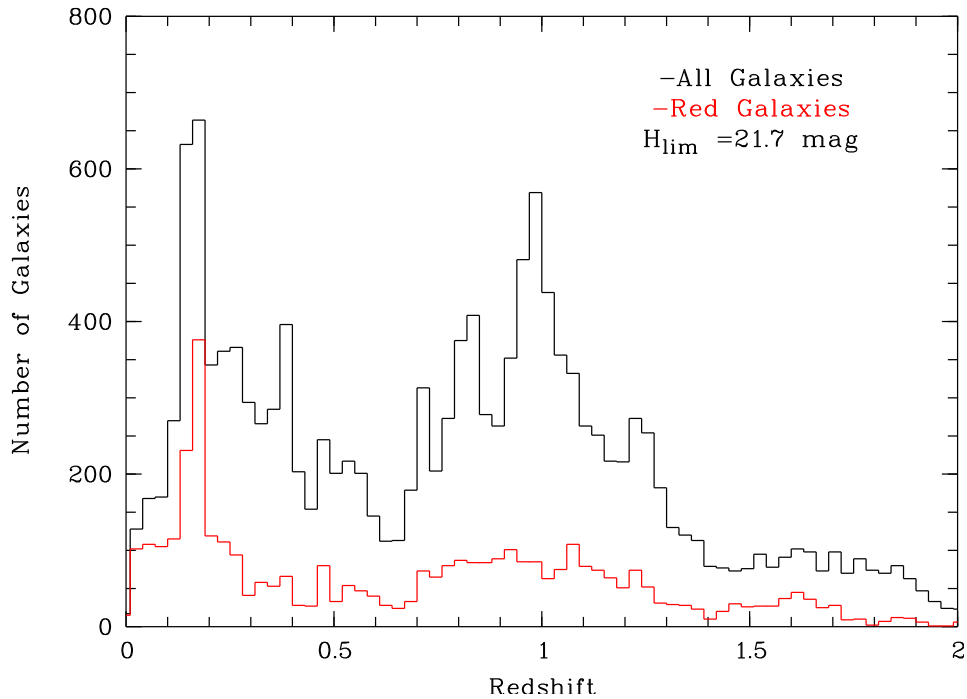

Figure 5.6: Histogram showing the distribution of galaxies between 0<z<2 in the A901-field. In black the distribution of all morphological type galaxies. In red, the distribution of red galaxies having $(U_{280} - V) > (U_{280} - V)_{limit}$, see Eq. 5.3. The red sequence galaxies belonging to the A901 cluster forms a sharp peak at z=0.165. The A901-field contains only few red galaxies beyond z$\sim$ 1.6.

5.2 left panel. In order to investigate how the red sequence and the blue cloud evolved with redshift in a CMD, we have divided our galaxy sample into 9 redshift slices starting at z=0.2 to avoid the A901 cluster in our lowest redshift slice. The redshift slices have been chosen to be equal comoving volumes up to z=1.3, the three last redshift slices enclose a comoving volume 2.5 times larger than the other slices in order to include a substantial amount of galaxies in those high redshift slices. Figures 5.7 and 5.8 show the evolution of the red sequence through the different CMDs at different increasing redshift intervals, we see that the bright end of the red sequence is a few tenths of a magnitude bluer at z=2 than at z=0.2. The CMDs show that for a given magnitude both galaxy populations were bluer in the past. We also see that starting at z$\sim$1 as we go back in time there is an increasing population of galaxies which are bright M_V<-22 and blue $(U_{280} - V) \lesssim 1$. To better quantify the evolution through cosmic time of the characteristic absolute magnitude for the red and the blue galaxy population, the luminosity function has been calculated for each galaxy population in different redshift slices of the Universe and are presented in the next chapter.

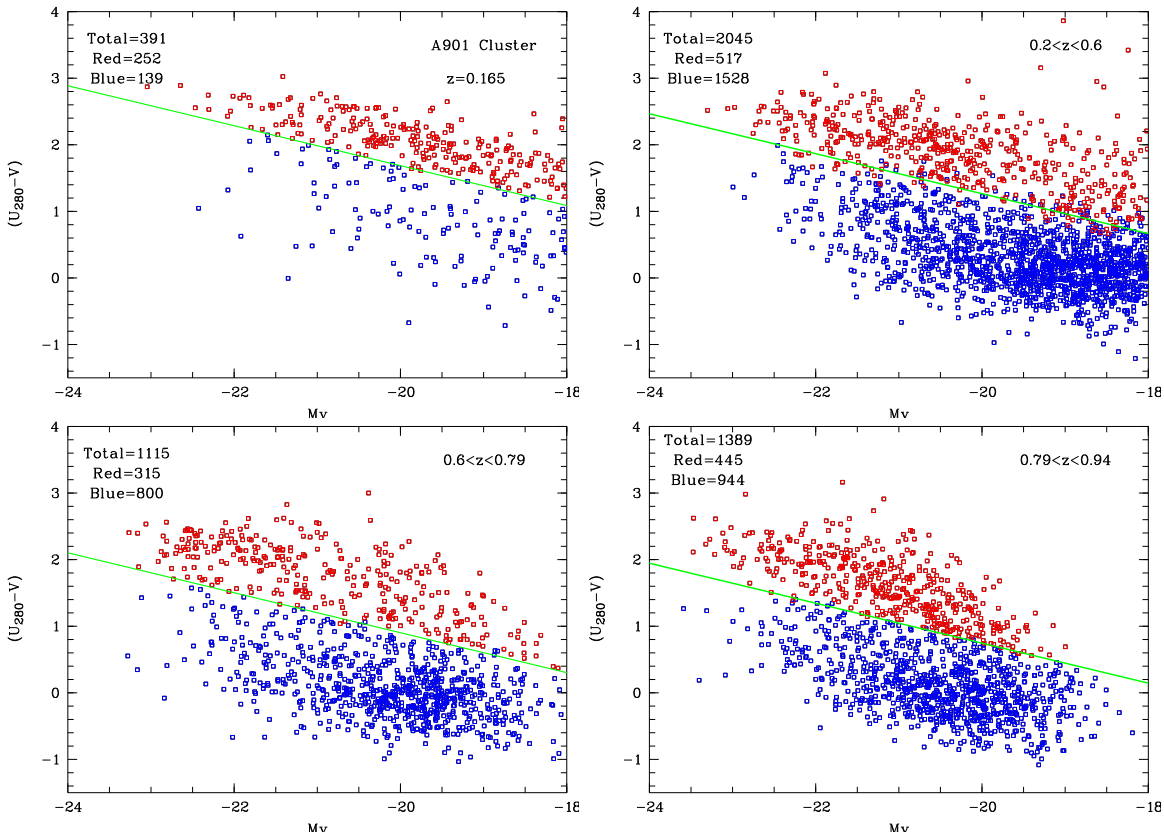

Figure 5.7: CMD for galaxies with H<21.7 mag in different redshift slices as given in top right of each panel. The green line indicates the bimodality separation as described by Eq. 5.3, the mean redshift of each bin has been use to plot the line. Red galaxies lie above the line, blue galaxies below the line. Top left panel shows the A901 cluster as a reference. The total number of objects included in each diagram as well as the blue and red fraction are given in the top left of each panel. Except for the A901 panel all redshift bins are equal comoving volumes.

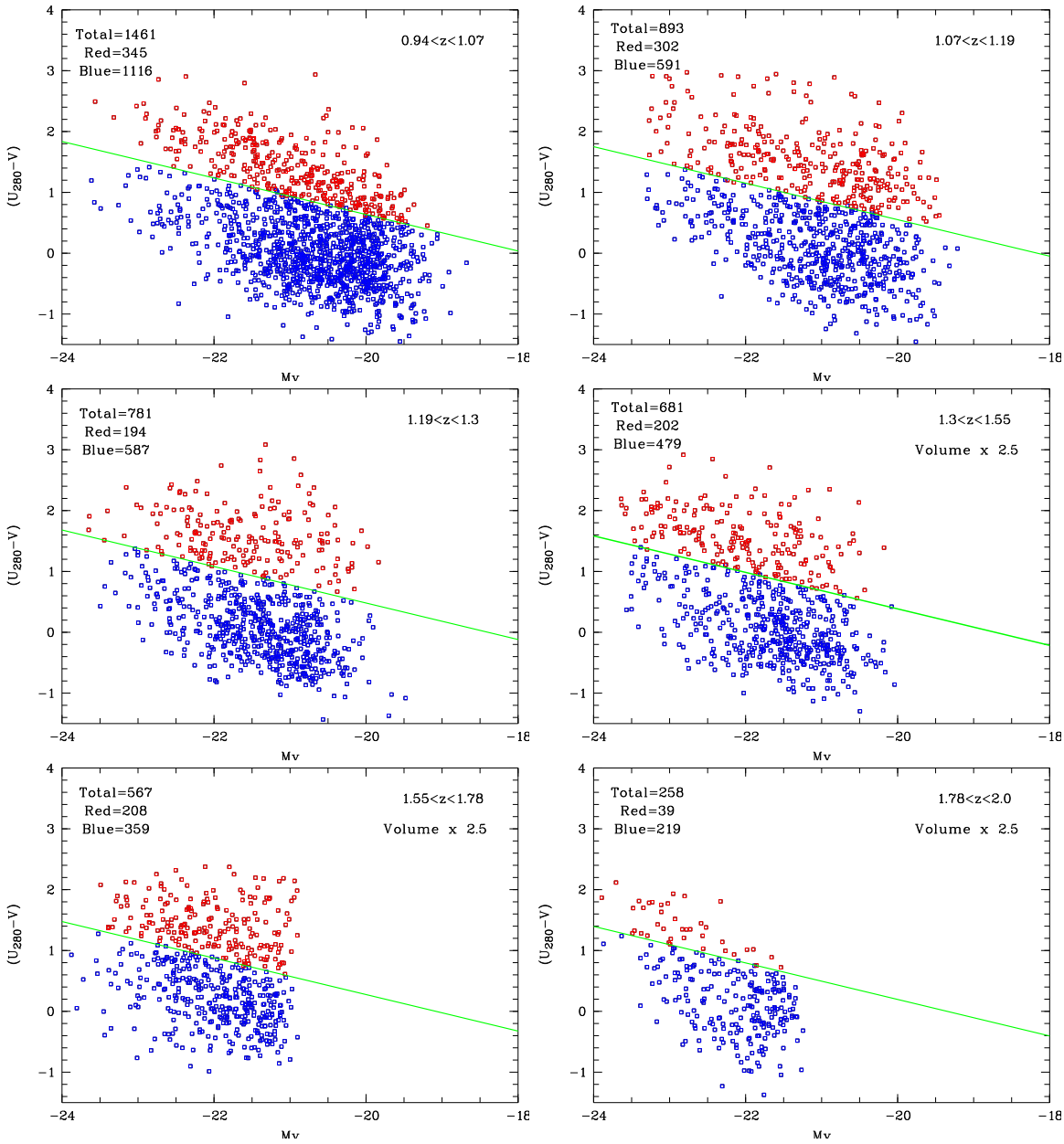

Figure 5.8: CMD for galaxies with H<21.7 mag in different redshift slices as given in the top right of each panel. The green line indicates the bimodality separation as described by Eq. 5.3, the mean redshift of each bin has been use to plot the line. Red galaxies lie above the line, blue galaxies below the line. The three highest redshift bins enclose a comoving volume 2.5 times more than the lower redshift bins. The total number of objects included in each diagram as well as the blue and red fraction are given in the top left of each panel. The magnitude limit of the survey affect both galaxy populations in the CMD for the redshift slice 1.55<z<1.78 (bottom left panel) the data form almost a vertical line at the faint end, in that redshift range the rest-frame M_V is shifted in the observed H-band.

Chapter 6

Evolution of the Luminosity Function

This chapter investigates the evolution of the luminosity function through cosmic time for the red and the blue galaxy populations. A description of the methodology used to calculate the luminosity function is presented followed by our results. The evolution through cosmic time of the characteristic luminosity M* and the number density ϕ^* are discussed.

6.1 Definition of the Luminosity Function

In order to study the evolution of galaxies through cosmic time, one naturally has to study how their luminosity evolves with time since the luminosity of a galaxy is directly linked to its stellar population and reflects its star formation history. It is meaningful to derive a luminosity function (LF) for different epochs of the Universe and for different galaxy populations to see how galaxy populations have evolved since z=2 to the present day. The galaxy luminosity function is defined as the number of galaxies in a range of luminosities [L, L+dL] or absolute magnitudes [M, M+dM] per volume and is generally expressed in units of galaxies/Mpc^3. Using the formalism from Binney & Merrifield (1998), the function is normalized so that:

$$\int_{-\infty}^{\infty} \Phi(M) dM = \nu \tag{6.1}$$

where ν is the total number of galaxies per unit volume and $\Phi(M)$ is the number density of galaxies in the magnitude range [M, M+dM]. While plotting the LF $\Phi(M)$ as a function of magnitude M, the resulting LF has a curved shape due to the number of galaxies decreasing monotonically with increasing magnitude. From the faint end to the bright end, the LF $\Phi(M)$ decreases along a power law reaching a knee at a characteristic magnitude M^* and cuts off at bright magnitudes. The behaviour of the LF can be parameterized by the Schechter function expressed in magnitude as follows:

$$\Phi(M) = (0.4ln10)\Phi^* 10^{0.4(\alpha+1)(M^*-M)} exp(-10^{0.4(M^*-M)}) \tag{6.2}$$

where Φ^* is the normalization of galaxy density at the fiducial magnitude M^* and α is the slope at the faint end. Those three parameters are interconnected, they can all be set as free parameters or the slope for example can be fixed in order to better fit the data. In principle, calculating the LF consists only in counting the number of galaxies in different magnitude bins in a certain volume. However, with a magnitude limited sample of galaxies, we have to take into account that faint galaxies could escape our survey.

6.2 Luminosity Function Estimator

The non-parametric $1/V_{max}$ estimator (Schmidt 1968) has been used to calculate the luminosity function in different redshift slices. This method allows to take into account the effect due to the survey incompleteness and corrects for the galaxies which are too faint to be observed within a given redshift slice. Also due to our limited magnitude sample of H<21.5 our ability to trace the faint end of the LF decreases with redshift. The $1/V_{max}$ method has the advantage in simultaneously giving the shape and the normalization of the LF but has the disadvantage of being sensitive to the density fluctuation since the method assumes that galaxies are uniformly distributed in the Universe (Willmer 1997). Other methods exist to calculate the luminosity function namely the STY (Sandage et al. 1979) method which is a parametric maximum-likelihood estimator often used in the current literature. Testing different LF estimators is a laborious task which is beyond the scope of this thesis, a description of different LF estimators as well as their associated results are discussed by Willmer (1997). For this work we used the $1/V_{max}$ estimator for its simplicity since it directly gives us the galaxy density in each magnitude bin and thus the normalization parameter Φ^* (assuming a uniform distribution). The differential luminosity function is given as the sum of the density contributions of each galaxy in a given magnitude/redshift/SED-type bin:

$$\Phi(M)dm = \sum_i \frac{1}{V_i(M, z, SED)} \tag{6.3}$$

where $V_i(M, z, SED)$ is the total comoving volume in which the galaxy i could be detected in our sample. The comoving volume is delimited by the redshift boundaries z_{lower} and z_{upper} of our redshift slice of interest. The comoving volume $V_i(M, z, SED)$ is defined as:

$$V_i(M, z, SED) = V_{shell} = \Delta\Omega \int_{z_{lower}}^{z_{upper}} \frac{dV}{d\Omega dz} dz \left\{ \quad \text{for } z_{max} \geq z_{upper}, \right.$$

$$V_i(M, z, SED) = \Delta\Omega \int_{z_{lower}}^{z_{max}} \frac{dV}{d\Omega dz} dz \left\{ \quad \text{for } z_{max} < z_{upper}, \right.$$

where $\Delta\Omega$ is the effective solid angle of the survey, V_{shell} is the total comoving volume enclosed in a shell delimited by the boundaries z_{lower} and z_{upper} and z_{max} is the maximum redshift that a galaxy having (z,M,SED) can have to still be included in our limited magnitude sample. The $1/V_{max}$ method means that if a galaxy is bright enough to be seen within all the redshift slices (if $z_{max} \geq z_{upper}$) then for a certain ΔM we would have $1galaxy/V_{shell}$ but if the galaxy cannot be seen within all the redshift slice (if $z_{max} < z_{upper}$) then for a given ΔM we would count $1galaxy/V_i(M, z, SED)$ where the comoving volume $V_i(M, z, SED)$ is enclosed between $z_{lower}<z<z_{max}$.

To determine the errors σ_ϕ for $\phi(M)dM$ we take only into account the statistical Poisson noise from the galaxy counts, thus $\sigma_\phi = \sqrt{\sum_i 1/V_i^2(M, z, SED)}$. In order to calculate the maximum redshift z_{max} that a galaxy could have we need a k-correction since a galaxy at z_{max} would have a rest-frame magnitude B (for a B-band LF) coming from an observed magnitude which is different than the one observed if that galaxy were at redshift z. Moreover each galaxy has a different SED and an associated k-correction. Ideally, a k-correction should be calculated for each individual SED. To simplify this task we used a common SED type to calculate the k-correction. The SED type #30 has been used (Fig. 6.1) since that is the average SED of our galaxy distribution (see §4.4 and Fig. 4.2 right panel). The maximum redshift z_{max} for each galaxy has been calculated by Bartelmann (priv. communication). First, using the SED#30, a normalised H-band k-correction as a function of redshift has been computed so that K(z=0)=0, see Fig. 6.4. Then, the rest-frame B-H colour has been calculated from the SED#30 and have been used to convert our derived B-band absolute magnitude M_B into an absolute H-band magnitude M_H in a straightforward way by H=B-(B-H). Then, having the absolute magnitude M_H for each galaxy, the luminosity distance D_{Lmax} for which the galaxy should drop below our detection limit has been calculated using Eq. 6.4 in which m_H=21.5 and K(z) as given by Fig. 6.2.

$$M_H = m_H - 5log\frac{D_{Lmax}}{10pc} - K(z) \tag{6.4}$$

From the luminosity distance D_{Lmax} the maximum redshift z_{max} is calculated using the definition of the D_L defined by Eq.1.6.

6.3 Galaxy Sample Division

A galaxy sample of 12023 having a magnitude limit H<21.5 has been separated into blue and red galaxy populations since the evolution of the characteristic luminosity M^* and density ϕ^* depends strongly on the galaxy type (Wolf et al. 2003). The redshift evolving colour-magnitude relation Eq. 5.3 has been used to divide the sample into these two populations. The galaxy sample has been additionally divided into redshift slices of nearly equal comoving volumes,

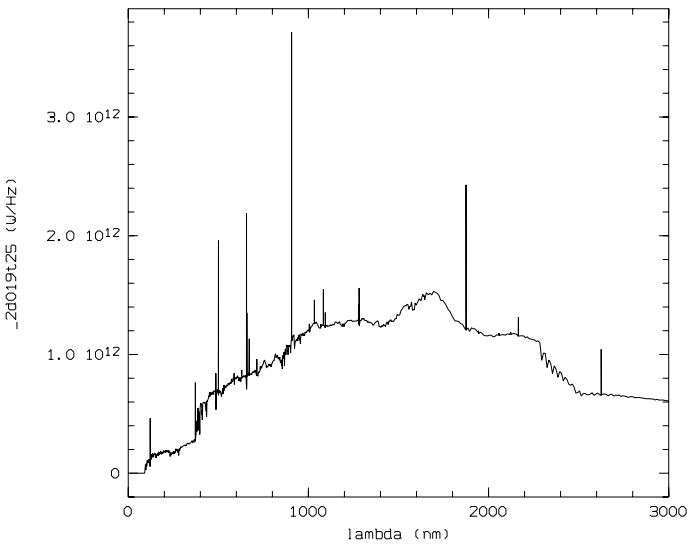

Figure 6.1: SED #30 used to calculate the k-correction in order to determine the boundary z_{max} in the determination of the comoving volume $V_i(M, z, SED)$ at which a galaxy could be located and included in our sample.

see Figure 6.3. The same redshift slices used to plot the CMDs in Fig.5.7 and Fig. 5.8 are used except that we have split the lower redshift slice from 0.2<z<0.6 into two slices since it contains many more galaxies than the other slices. We divided this slice at z=0.48 because this redshift falls between two peaks in the redshift distribution of galaxies, see Fig. 5.6. Exactly as for the CMDs the three highest redshift slices contain 2.5 times the comoving volume of the other slices.

6.4 Evolution of the Luminosity Function

The evolution of the luminosity function for the blue and the red galaxies throughout ten different redshift slices of the Universe is presented in Figures 6.4 and Fig. 6.5. A Schechter function has been fitted to our data points in order to obtain the characteristic magnitude M^* and the number density ϕ^* for each galaxy population in each redshift slice. At first glance, we see that for all redshifts the blue galaxies show a steeper faint end slope α compared to the red galaxies, which is why we have used a different slope in the Schechter fit for each galaxy population. Since our data are magnitude limited it is not possible to accurately determine the slope of the luminosity function. Since α, M^* and ϕ^* are correlated we decided to fix the parameter α in order to obtain meaningful values for M^* and ϕ^*. As a consequence, we have used a fixed slope of α=-0.5 for red galaxies and α=-1.3 for blue galaxies. These slope values are adopted from Faber et al. (2007) who derived the LF in the B-band for red and blue galaxies up to z=1 using the spectroscopic DEEP2 data set for 1 square degree in the sky. In their paper, Faber

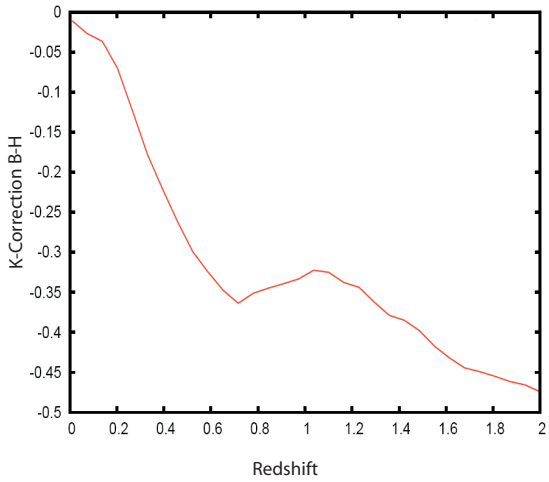

Figure 6.2: K-correction as a function of redshift for B-H normalized such that K(z=0)=0, from Matthias Bartelmann. This k-correction is used in Eq. 6.4.

et al. (2007) also compared the DEEP2 LF parameters with the ones obtained by the optical COMBO-17 survey for the 3 fields A901, A226 and S11 which represent 0.78 square degrees in the sky and concluded that the results agree. Adopting the same slope values from Faber et al. (2007) allows us to easily compare our values of M^* and ϕ^* up to z=1 with the literature .

The dotted vertical lines in Figures 6.4 and Fig. 6.5 indicate the magnitude limit for the Schechter function fit, data points fainter than the dotted line are not included in the fit because at that magnitude our sample is certainly incomplete. This limit is determined considering three factors. First, we choose the limit which corresponds to a magnitude where the number density Φ starts to decline on each LF plot due to the incompleteness of the survey whereby less and less faint objects are seen at fainter magnitude with increasing redshift. This limit can be recognized as the faint end of the rest-frame M_B magnitude versus redshift distribution due to our survey detection limit of H<21.5 (see Fig. 6.3) . Using the $1/V_{max}$ LF estimator, we noticed that the delimiting dotted lines in Figures 6.4 and Fig. 6.5 also correspond to a magnitude where more than 30% of the galaxies are in half of the comoving volume of any given redshift slice.

Figure 6.5 shows that the bright end of the LF is dominated by blue galaxies since z=2 up to z∼1 which has also been observed from z=1.75 to z=1 by Cirasuolo et al. (2007) using a K-band LF for UKIDSS data. Inversely, at lower redshifts between 0.6<z<0.94 (Fig. 6.4 bottom panels), the bright end is dominated by red galaxies. In the two lower redshift slices (Fig. 6.4 top panels) the bright end of the LF is populated by both red and blue due to two phenomena. On the one hand, a B-band LF creates a selection effect towards the blue galaxies

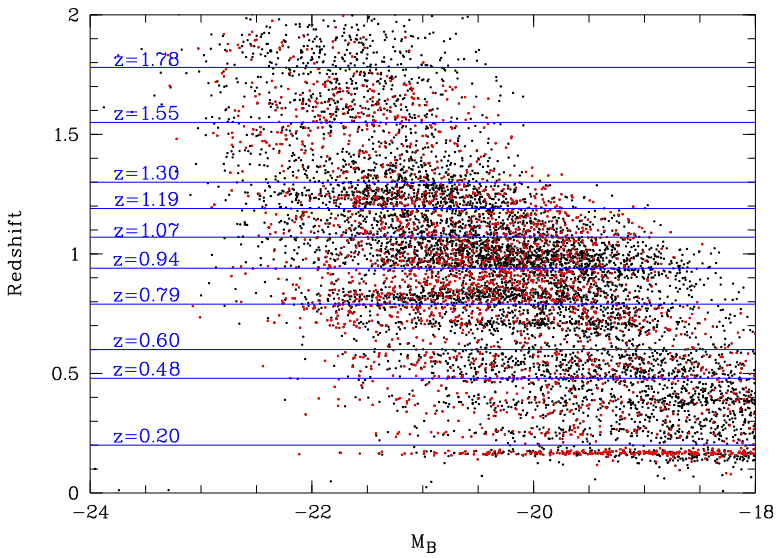

Figure 6.3: Redshift as a function of the rest frame M_B. The horizontal blue lines delimitate the redshift boundaries used to calculate the comoving volumes. The faint end of the distribution creates a fuzzy boundary due to the incompleteness of the survey beyond H=21.5. The colour of the data points represent the red galaxy population in red and the blue galaxy population in black.

which look brighter in B-band and on the other hand, the A901-field has a low number of red galaxies in those two redshift slices, see Fig. 5.6.

The best-fit parameters obtained for the Schechter function are listed in Tab. 6.1 separately for the red and the blue galaxy populations. The characteristic magnitude M^* for the blue and the red population has been compared with the one obtained by Faber et al. (2007) for the DEEP2 survey. Our values of M^* are consistent within the error bars with the M^* derived by Faber et al. (2007) for the blue and the red galaxies, however the number density ϕ^* is hardly comparable since our results are derived from a single field of an area of only 0.2 square degrees in the sky and are subject to large uncertainties due to cosmic variance. Consequently, our analysis focuses first on the evolution of the characteristic magnitude M^*. Our data show that both galaxy populations dimmed considerably from z=2 to z=0.2, the red galaxies having dimmed by ∼1.7 mag and the blue galaxies having dimmed by ∼1.2 mag in the B-band in that redshift interval. There is no direct comparable study in the literature on the LF for red and blue galaxies in the B-band in that redshift interval since we are the first team to have accomplished this task. As a comparison in a similar redshift interval, Ilbert et al. (2005) have derived the *global* LF which includes all galaxy types using VVDS data and found that the M_B^* has dimmed by a range of 1.7-2.4 mag between 2>z>0.05 in the B-band. Also, Cirasuolo et al. (2007) derived a K-band LF for blue and red galaxies and found that the red galaxies dimmed by M_K^* ∼0.5 mag and the blue galaxies dimmed by M_K^* ∼0.7 mag between

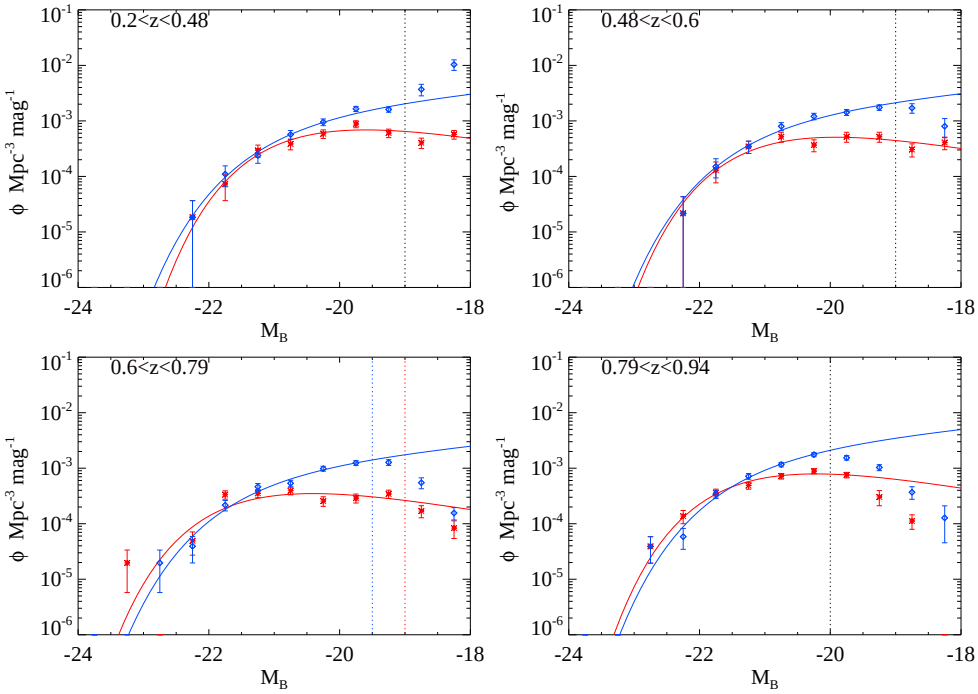

Figure 6.4: Luminosity function for the blue galaxies (blue solid line) and red galaxies (red solid line) in different redshift slices. The vertical lines indicate the faint absolute magnitude limits considered in the $1/V_{max}$ estimator for the blue (blue dashed line), the red (red dashed line) or both (black dashed line) galaxy populations.

1.75>z>0.25. The small evolution of M_K^* observed by Cirasuolo et al. (2007) in the K-band is expected since the decrease of the star formation rate by a factor $\sim$ 10 since z=1 (see Fig. 1.5) affects M_B^* much more than M_K^*, the B-band being much more sensitive to the new born stars.

Between 1>z>0.3 our data show that the red galaxies have dimmed by $\sim$0.5 mag and the blue galaxies have dimmed by $\sim$0.6 mag, consistent with Faber et al. (2007) (see Fig. 6.6) for the red galaxies in that redshift interval, but a little less for the blue galaxies compared to DEEP2. Nevertheless, our ΔM_B^* value for the blue galaxies is consistent with the result obtained with the optical COMBO-17 data between 1>z>0.3, indicating that even the M^* evolution may depend on the surveyed part of the Universe. At higher redshift between 1.9>z>1 the red galaxies have dimmed by $\sim$1.2 mag while the blue galaxies have dimmed by $\sim$0.7 mag. These results have to be interpreted with care since our sample is not complete above z$\sim$1.3 as the data points in the LF start to be incomplete before reaching the faint end slope of the distribution which affects the resulting M_B^* and ϕ^*. As a comparison, Ilbert et al. (2005) found that the *global* B-band LF dimmed by $\sim$0.4 mag between 1.65>z>0.9.

Figure 6.6 right panel shows the evolution of the number density ϕ^* as a function of redshift.

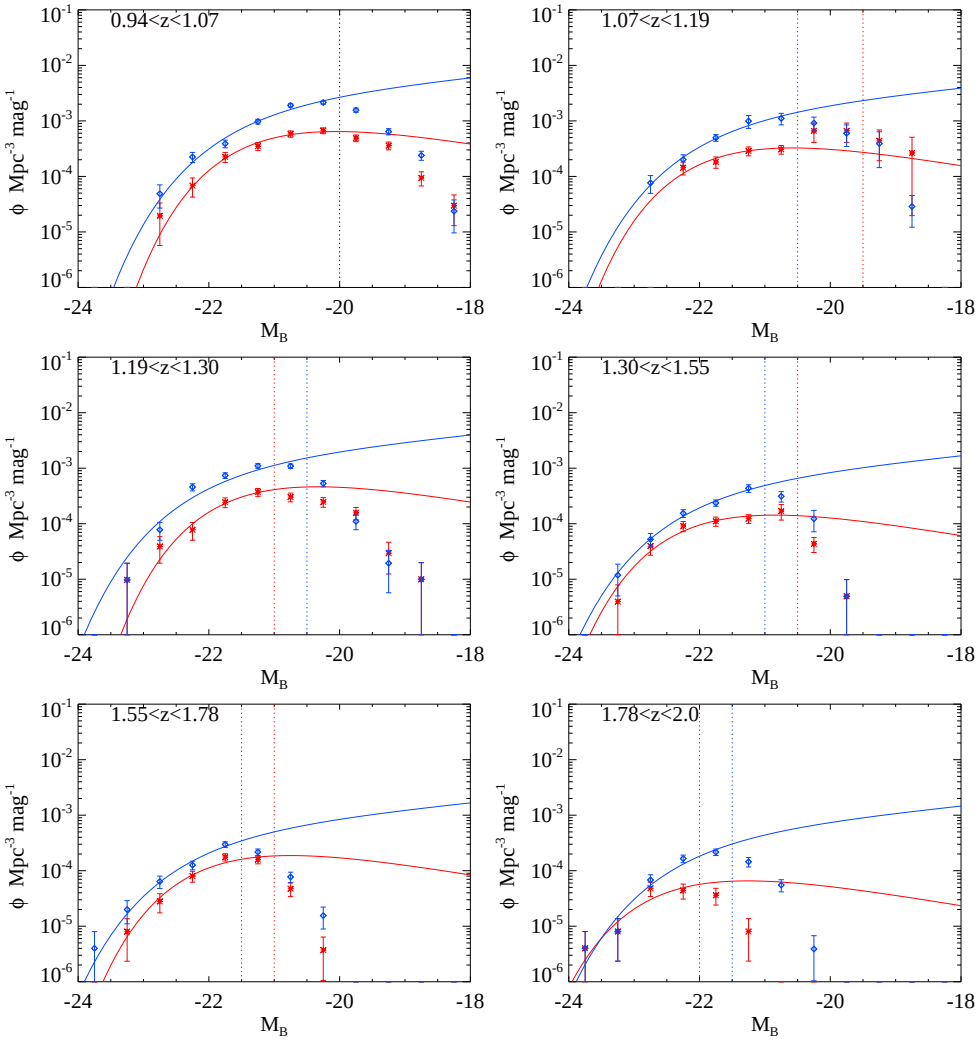

Figure 6.5: Luminosity function for the blue galaxies (blue solid line) and red galaxies (red solid line) in different redshift slices. The vertical lines indicate the faint absolute magnitude limits considered in the $1/V_{max}$ estimator for the blue (blue dashed line), the red (red dashed line) or both (black dash line) galaxy populations.

As a global behaviour, we see that the distribution varies unevenly due to the cosmic variance. In particular we see a high peak in the distribution between $0.7 \gtrsim z \gtrsim 1.1$ due to the fact that the A901-field seems to have a great amount of objects in this redshift interval, especially blue galaxies, see Fig. 5.6 and Tab. 6.1. As a general trend we see that the number density of red galaxies increases by a factor $\sim$10 between 1.9>z>0.3 while for the blue galaxies it increases more mildly by a factor $\sim$3. The trend in the evolution of ϕ^* in our A901-field can not be considered as the average behaviour of the number density for the red and the blue galaxy populations as a function of redshift in our Universe as the surveyed volume is rather small and thus subject to large variations due to large scale structures.

z	N galaxies	M_B^*	$\phi^*(\times 10^{-4}$ Gal. Mpc$^{-3})$	α_{fixed}
RED				
0.20-0.48	325	-20.34±0.11	17.43± 1.70	-0.50
0.48-0.60	192	-20.67±0.13	12.86± 1.39	-0.50
0.60-0.79	315	-21.16±0.11	8.84±0.68	-0.50
0.79-0.94	445	-20.97±0.09	12.00±1.63	-0.50
0.94-1.07	345	-20.80±0.10	16.30±1.62	-0.50
1.07-1.19	302	-21.33±0.20	8.25±1.161	-0.50
1.19-1.30	194	-21.09±0.16	11.72±2.61	-0.50
1.30-1.55	202	-21.60±0.12	3.62±0.48	-0.50
1.55-1.78	208	-21.50±0.13	4.75±0.68	-0.50
1.78-2.0	39	-22.02±0.27	1.66±0.64	-0.50
BLUE				
0.20-0.48	987	-20.76±0.13	16.51± 2.02	-1.30
0.48-0.60	541	-20.96±0.13	15.83±1.88	-1.30
0.60-0.79	800	-21.21±0.12	11.71±1.33	-1.30
0.79-0.94	944	-21.09±0.10	24.39±2.89	-1.30
0.94-1.07	1116	-21.31±0.09	27.12±2.58	-1.30
1.07-1.19	591	-21.66±0.17	15.92±4.03	-1.30
1.19-1.30	587	-21.84±0.09	15.30±1.58	-1.30
1.30-1.55	479	-21.91±0.15	6.33±1.30	-1.30
1.55-1.78	359	-22.00±0.17	6.15±1.57	-1.30
1.78-2.0	219	-22.00±0.16	5.37±1.24	-1.30

Table 6.1: Best-fitted Schechter function parameters for the red and blue galaxy populations; the characteristic magnitude M_B^* as well as the number density ϕ^* are given with their 1 sigma error, the slope α from Faber et al. (2007) has been kept fixed.

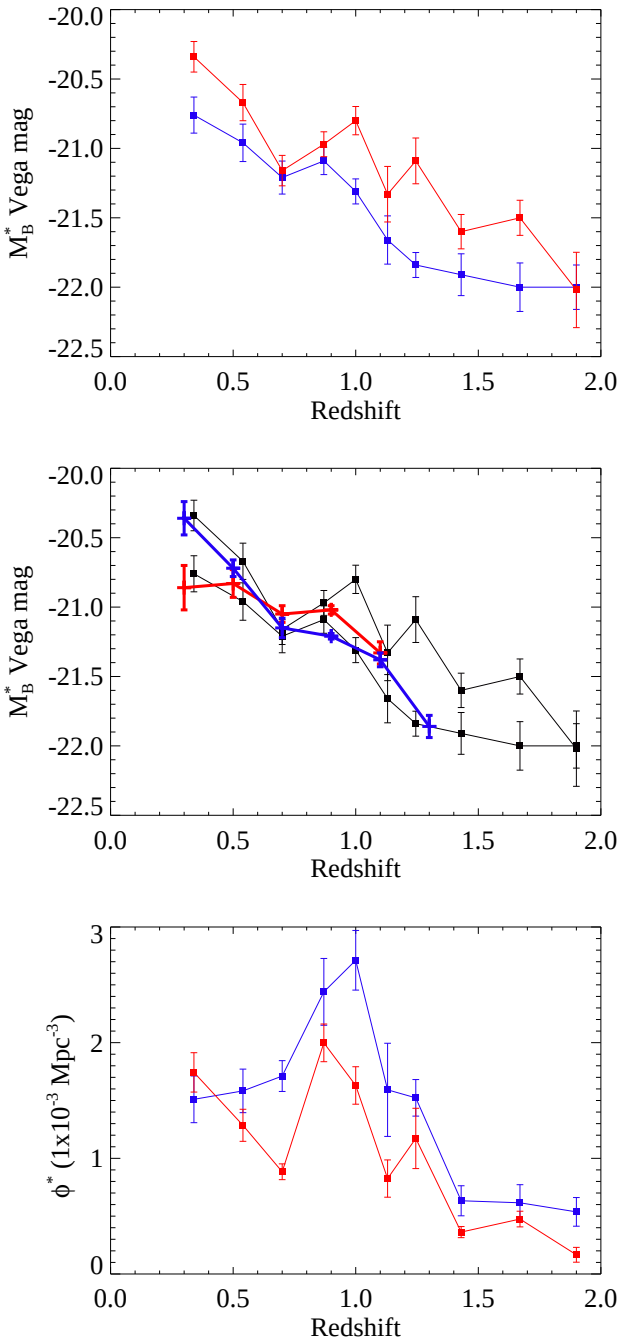

Figure 6.6: Top: Evolution of the characteristic magnitude M_B^* for the red (in red) and the blue (in blue) galaxy populations as a function of redshift. Middle: Our values of M_B^* for the blue and the red populations (in black) are compared to the values obtained by Faber et al. (2007) from the spectroscopic survey DEEP2. The red population follows the trend of the red line and the blue population the trend of the blue line. Bottom: Evolution of our number density ϕ^* values for the red and the blue galaxies as a function of redshift.

Chapter 7

Evolution of the Mass Function

This chapter traces the evolution of the stellar mass of the red and blue galaxy populations through cosmic time. The method to derive the galaxy masses is first described followed by an analysis of several colour-mass and mass function diagrams for different epochs of the Universe. Finally, some example of very massive high redshifted objects from our galaxy sample are shown.

The most intriguing questions about galaxy evolution is how the galaxy stellar mass is assembled and how the red sequence mass is build-up. The mass function (MF), analogous to the luminosity function, is a useful tool to study the stellar mass distribution among galaxies. Colour-mass diagrams (CM_*D) are also used to investigate the stellar mass distribution since the red and the blue galaxy populations lie in preferential places in such diagrams. The evolved galaxies having an old stellar population trends to be more massive and redder than galaxies having mainly a new born stellar population which only dominate the flux. The colour and the mass of a galaxy are directly related to its star formation history. In order to see how the galaxy populations' masses evolve we have used the same sample as used to investigate the LF in the last chapter. The sample consists of 12023 galaxies having a magnitude down to $H<21.5$. The sample has been divided into the red and the blue galaxy population using Eq. 5.3 derived in §5.3 and has also been divided into quasi equal volume slices as described to calculate the LF in the previous chapter, see §6.3.

7.1 Mass Determination

In order to trace the evolution of the stellar masses for the blue and the red galaxy populations it is necessary to first derive the mass for each galaxy. The galaxy masses are calculated from the stellar mass-to-light ratio (M_*/L) obtained from the galaxy templates which are derived from the population synthesis model PEGASE (Projet d'Étude des GAlaxies par Synthèse Évolutive) (Fioc & Rocca-Volmerange 1997). This way, we obtain the mass for each galaxy

which is a direct representation of its star formation history. As also described in §4.3.2 the galaxy templates are generated by the PEGASE code in which gas with half solar metallicity (Z/Z_0=0.5) and a Kroupa IMF serve as input in a closed box model. We further assume a two burst star formation history scenario in which the SFR follows two exponential declines, the first burst occurred several billion years ago with an e-folding time of 1 Gyr and a second burst started 2750 Myr after the first burst with an e-folding of 0.1 Gyr, see Meisenheimer et al. (in prep 2009) for more details. This two burst model gives a better approximation of the galaxies star formation histories than the one burst model, which cannot reproduce the stellar population of for example spiral galaxies like the Milky Way which contains both an old stellar population and ongoing star-formation activity. In order to obtain the masse of a galaxy we first derive the galaxy luminosity L_V from its rest-frame magnitude M_V in the V-band as described by Eq. 7.1, then the mass is derived by multiplying the M_*/L in units of $M_\odot$ and $L\odot$ by the luminosity as described by Eq. 7.2.

$$\frac{L_V}{L_{\odot V}} = 10^{-0.4(M_V - M_{\odot V})} \tag{7.1}$$

$$M_{*V} = \left(\frac{M_*}{L}\right) \times L_V \tag{7.2}$$

Here the rest-frame V-band is used in order to compare our results with the literature. The V-band is generally used in the literature since many studies derive stellar masses using a direct measurement of the luminosity in the V-band and convert it into mass. Our approach differs in that we use the direct information of the star formation history of each galaxy template to derive its mass. The galaxy SED templates colours ($U_{280} - V$) are plotted as a function of their stellar mass-to-light ratios M_*/L in Fig. 7.1. We clearly see a trend in which the galaxy templates having higher M_*/L have redder colour. This trend directly connect the colour of a galaxy with its mass in the sense that red galaxies are massive and blue galaxies are less massive unless they are affected by dust extinction and look redder.

7.2 Colour-Mass Diagrams up to z=2

Using the mass for each galaxy, colour-stellar mass diagrams (CM$_*$D) for the red and the blue galaxy population have been created for ten different redshift slices of the Universe and are shown in Fig. 7.2 and Fig. 7.3. The red galaxy population is shown in red and the blue galaxy population is shown in black. By analyzing the CM$_*$Ds we see the general trend that for a fixed mass both galaxy populations were bluer in the past. This result is analogue to the evolution of the LF derived in the previous chapter where for a fixed magnitude both galaxy populations were bluer in the past. This result is expected since the masses are calculated using the galaxies luminosities, accordingly for a fixed M_*/L brighter galaxies would be more massive. Figure

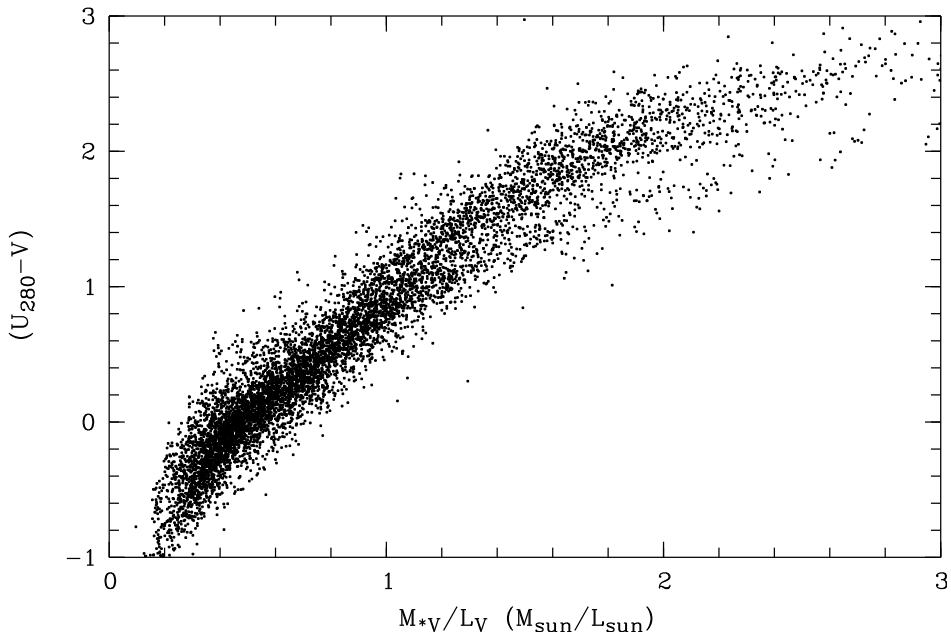

Figure 7.1: Colour $(U_{280} - V)$ as a function of the stellar mass-to-light ratio M_*/L from our galaxy SED templates. Galaxies having red colours $(U_{280} - V) \gtrsim 1$ have a high M_*/L ratio while galaxies having bluer colour $(U_{280} - V) \lesssim 1$ have a smaller M_*/L.

7.2 shows that since $z \sim 1$ the massive galaxies are dominated by the red galaxy population while Figure 7.3 shows that there is a growing population of massive ($M_* \gtrsim 10^{11}$) and blue $(U_{280} - V) \lesssim 1$ galaxies as we go back in time. This blue and massive galaxy population seems to have no analogue in the local Universe since massive blue galaxies are rare at low redshift. The grey line on each panel in Fig. 7.2 and Fig. 7.3 indicates the effect of our magnitude limited sample at H=21.5, above which objects escape our sample.

7.3 Evolution of the Mass Function

To better quantify the galaxy populations' stellar masse evolution through cosmic time, mass functions have been derived for the blue and the red galaxy populations in the same thin redshift slices as used for the CM_*D. The mass function is a mass version of the luminosity function and is defined as the number of objects in a stellar mass interval $[M_*, dM_*]$ in a volume V_i described by the $1/V_{max}$ formalism, see §6.2. The differential stellar mass function is:

$$\Phi(M_*)dM_* = \sum_i \frac{1}{V_i} dM_* \tag{7.3}$$

The mass function derived in ten redshift slices of the Universe for our two galaxy pop-

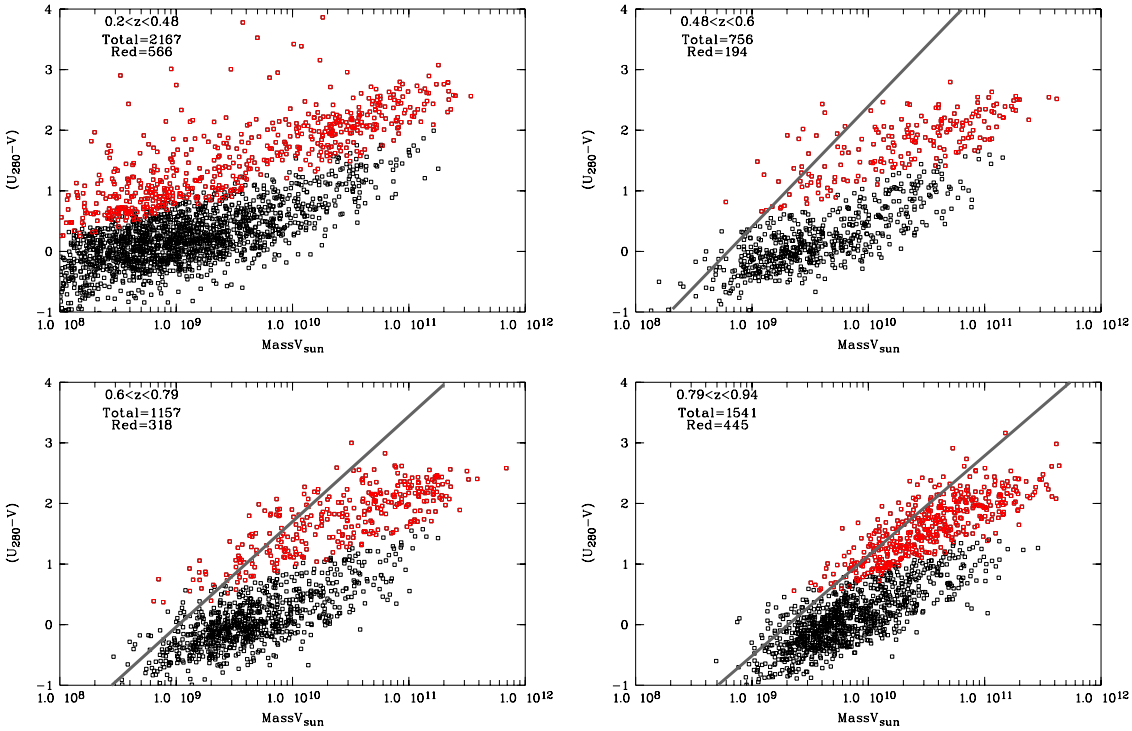

Figure 7.2: Colour-stellar-Mass Diagrams for different redshift slices of the Universe. The red galaxy population is colour coded in red and the blue galaxy population is colour coded in black. The grey line, if present, represents the effect of our survey completeness which is the apparent magnitude H=21.5. The total number of objects as well as the number of red galaxies in the redshift slice are indicated on the top left corner of each panel.

ulations of interest are shown in Fig. 7.4 and Fig. 7.5. On each panel the vertical red and blue lines indicates the completeness of our survey respectively for the red and the blue galaxy populations, the data points fainter that the lines are incomplete. These completeness lines are determined based on the completeness grey line plotted on each CM_*D in Fig. 7.2 and Fig. 7.3 from which we determined at which mass most of the galaxy lie below the grey line. Figures 7.5 shows that between $0.3 \lesssim z \lesssim 0.9$ the red galaxy population dominates the massive end of the mass function while the blue galaxy population dominates the low mass end. This has also been observed by Borch et al. (2006) who derived the mass function for the red and the blue galaxy populations since z=1 using the optical COMBO-17 data set for the A901, A226 and S11 fields. Even if our data contains only 3/4 of the A901-field and are subjects to large scale structures, our results agree well with Borch et al. (2006). Since our galaxy sample is H-band selected our completeness limit for the red galaxy population reaches smaller masses than Borch et al. (2006). Inversely, our blue galaxy population is less complete than the R-band selected galaxy sample from Borch et al. (2006).

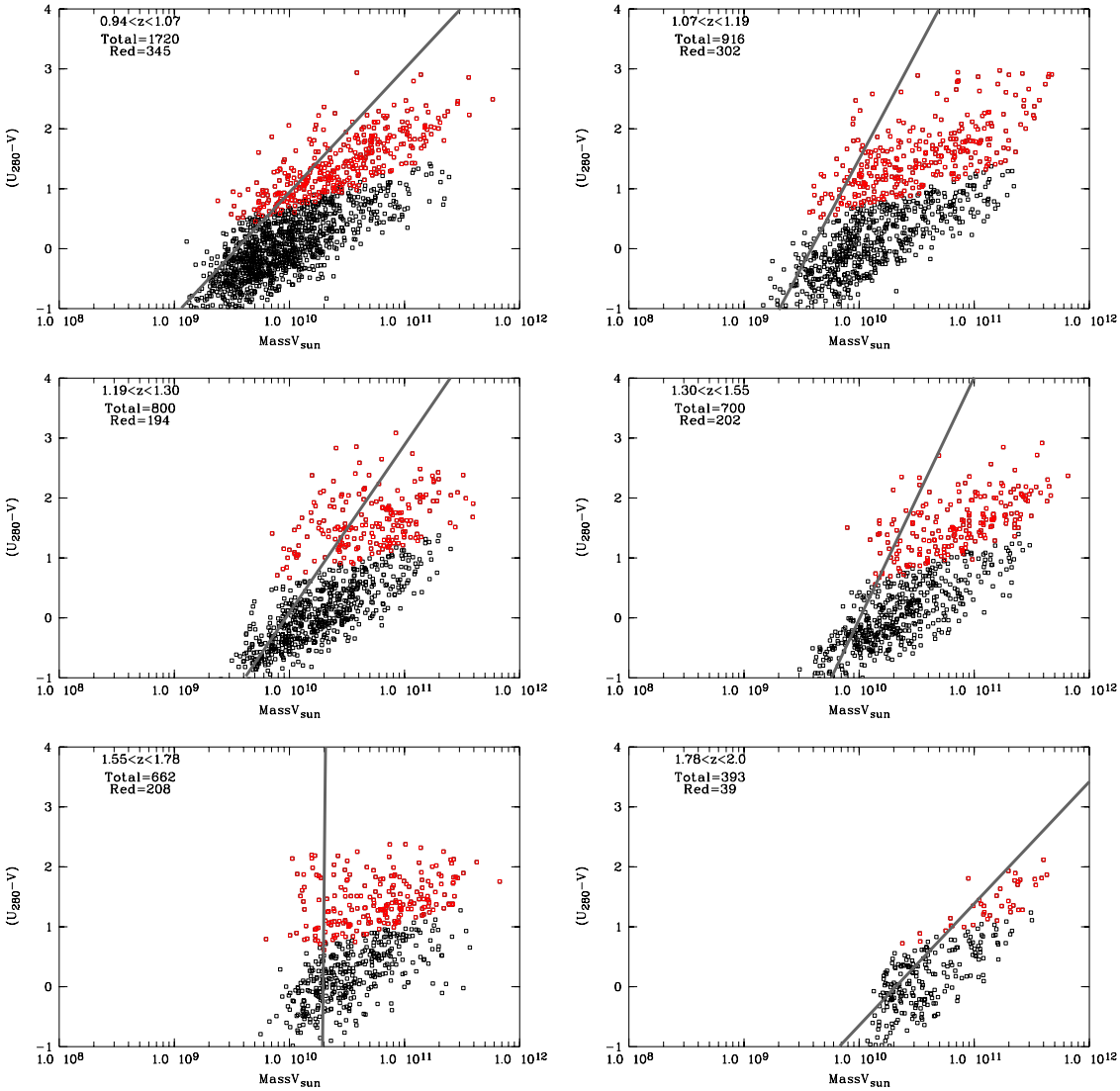

Figure 7.3: Colour-Mass Diagrams for different redshift slices of the Universe. The red galaxy population is colour coded in red and the blue galaxy population is colour coded in black. The grey line represents the effect of our survey completeness which is the apparent magnitude H=21.5. The total number of objects as well as the number of red galaxies in the redshift slice are indicated on the top left corner of each panel.

The Figure 7.6 shows the red and the blue galaxy populations' mass function in different redshift slices for the Universe above z$\sim$ 1. We see that between 1$\lesssim$z$\lesssim$1.6 the massive part of the mass function is populated by red and blue galaxies while the low mass end is dominated by blue galaxies as in the low redshift Universe. As for the luminosity function those results have to be interpreted with care because our small field can be influence by large scale structures. Nevertheless, our data seems to tell us that both massive star forming blue and quiescent red galaxies were in place at z$\sim$1.6. The galaxy mass assembly is currently a matter of debate and

most of the studies concern the Universe below z=1. Only few studies have investigated the mass assembly between 1<z<2. Among them, Arnouts et al. (2007) using the SWIRE-VVDS-CFHT survey showed that between 2≥ z ≥1.2 the quiescent galaxy population as strongly increases their stellar mass by a factor ∼10 while the star-forming galaxy population only increases its mass by a factor ∼2.5. The results from Arnouts et al. (2007) shows that between 2≥ z ≥1.2 galaxies undergo mass assembly, in contrast to the present day where most of the galaxies are in place. In addition, Vergani et al. (2008) derives a MF for early and late type galaxies up to z=1.3 and found that the stellar mass function shows an increasing relative contribution of massive early type galaxies and a decreasing relative contribution of late type galaxies with cosmic time.

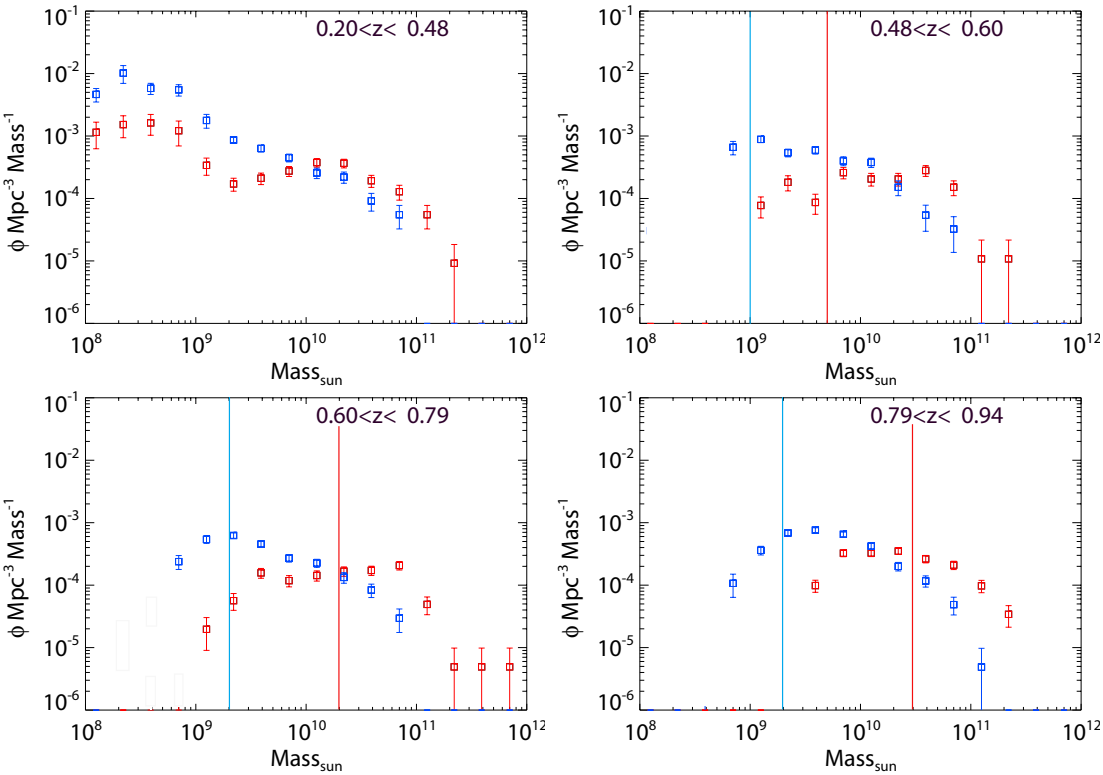

Figure 7.4: Mass function in different redshift slices for the red (red data points) and the blue (blue data points) galaxy populations. The vertical lines indicates our survey completeness for the red (in red) and the blue (in blue) galaxy populations.

7.4 Massive Distant Galaxies

The last redshift slice Fig. 7.5 bottom right is shown only as a reference since the red galaxy population is incomplete through all of the redshift slice. Nevertheless, this plot shows the presence of very massive red galaxies in that redshift interval. The two *red* data points above

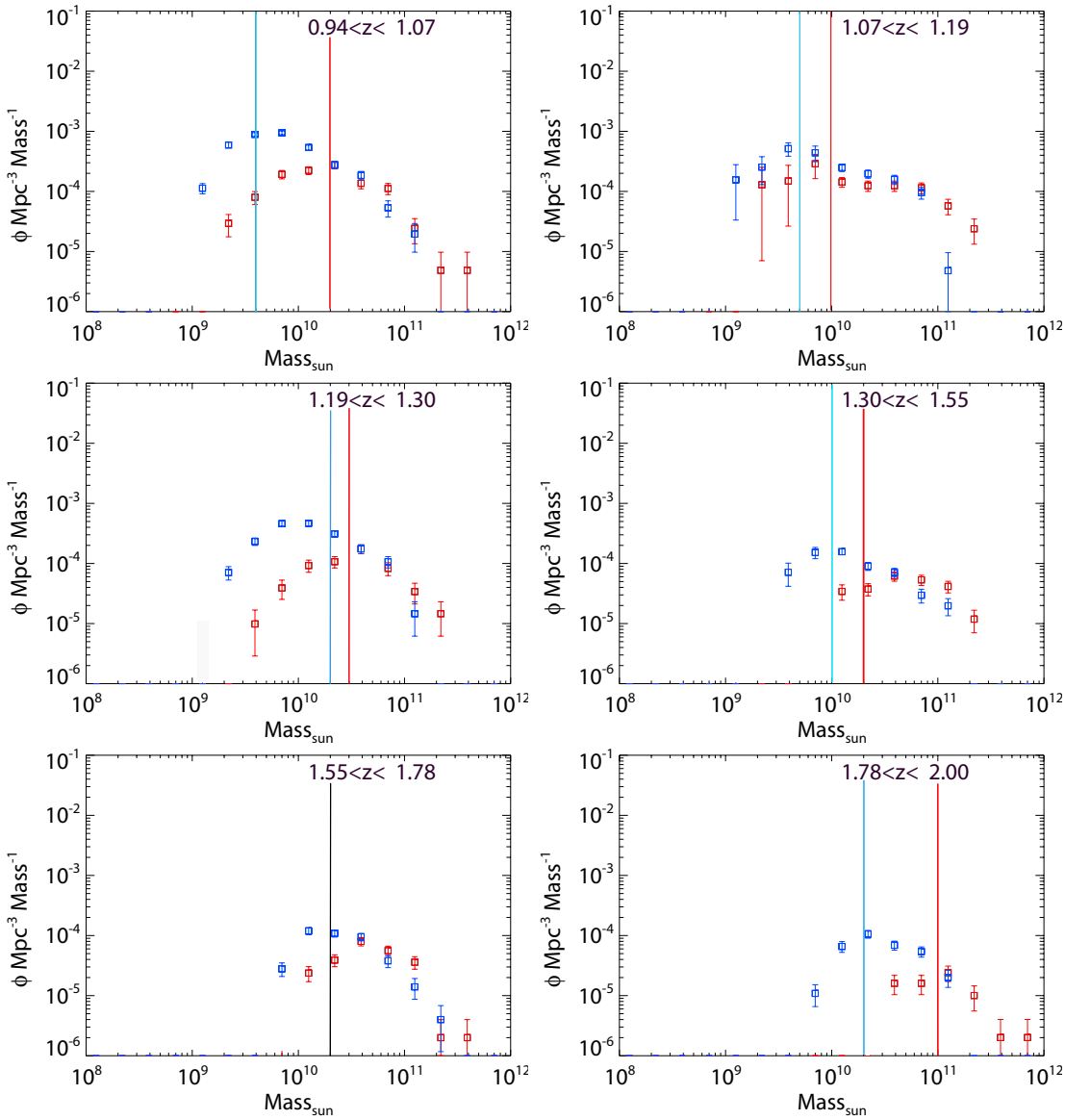

Figure 7.5: Mass function in different redshift slices for the red (red data points) and the blue (blue data points) galaxy populations. The vertical lines indicates our survey completeness for the red (in red), the blue (in blue) or both (in black) galaxy populations.

M $>3\times10^{11}M_{\odot}$ consist of 5 very massive objects. We have further investigated those objects to understand their nature. Fig. 7.6 to Fig. 7.10 show each of them, on each Figure an H-band image is shown on the top and the best-fitted SED at the bottom. Figure 7.6 shows an object at z=1.848 with a stellar mass of M_*=3.4×10^{11}. This object shows a red colour of $(U_{280}-V)$=1.7 and is very bright with an absolute magnitude M_V=-23.48. By the aspect of the image and the SED this object seems to be a massive red evolved elliptical galaxy. Figure 7.7 shows a galaxy at z=1.859 having an absolute magnitude M_V=-23.71, a stellar mass M_*=4.0×10^{11}

and a colour $(U_{280} - V)$=2.12, making it the reddest object of our sample. The photometric data points indicate that the NIR flux is even higher than the best fitted template. This object seems to be a very red evolved elliptical galaxy. The surrounding objects in the image are at much lower redshift. Figure 7.8 show an other object at z=1.862, this object has an absolute magnitude M_V=-23.40, a stellar mass M_*=3.84×10^{11} and a colour $(U_{280} - V)$=1.8. The SED corresponds to an evolved red galaxy but the image shows a blob just below this object which could belong to it while the other objects in the image are at much lower redshift. Figure 7.9 shows a massive object at z=1.832, this galaxy has an absolute magnitude M_V=-23.89, a stellar mass of M_*=4.27×10^{11} and a red colour $(U_{280} - V)$=1.87. The SED seems to correspond to an evolved red galaxy and our photometric data points indicate even higher NIR flux. The other object in the image is a galaxy at z=0.6. Figure 7.10 shows an object at z=1.885. This galaxy has an absolute magnitude M_V=-23.23, a stellar mass of M_*=3.36×10^{11} and a colour $(U_{280} - V)$=1.79. The photometric data points indicate that the NIR flux is even higher than the best-fitted template. Moreover maybe the object has some emission lines as the two narrow-bands photometric data points around 900 nm seem to indicate but our best fitted SED suggests that this object is a red evolved elliptical galaxy. On the image we also see a star in the bottom right corner.

7.5 The Most Massive Distant Galaxy

Fig. 7.11 shows the most massive object found in our sample which is located at z=1.87 and has a stellar mass M_*=1.01×10^{12}. This object has the brightest rest-frame absolute magnitude of our sample with M_V=-24.75 and its colour is $(U_{280} - V)$=1.85. On the H-band image the object seems to be a single source due to the limited resolution of the deep H-band image (1.3" FWHM). On the image taken by the ACS on HST (observed wavelength $\lambda_{obs} = 606\,\mathrm{nm}$, i.e. $\lambda_{rest} = 211\,\mathrm{nm}$ in the UV) we can see that the source seems to split in several patches. Most likely, this is an ongoing merger of two galaxies (similar to the Antennae galaxy in the local Universe). Thus, most of the star formation is obscured by dust and the UV light can only escape through holes of low extinction. The SED reveals a considerable amount of flux in the NIR (rest-frame optical) which supports the presence of high dust obscuration. In this object we seem to witness a gas-rich merger at a redshift close to $z = 2$. Note that the very red SED of the object might push our photometric classification technique to its limits. Thus, we cannot exclude that obscuration with $A_V > 1.5$ (that is the upper limit in our template library) leads to an over-estimate of the M_*/L ratio. For a better understanding of such systems we have to rely on spectroscopic observations in the NIR, which will not only determine the strength of the 4000 Å break more accurately (old stars) but also should detect the emission lines contained in our template spectrum (see Fig. 7.11). The future is promising since newly developped NIR spectrometers like LUCIFER at the Large Binocular Telescope will soon be able to provide spectra for such interesting systems.

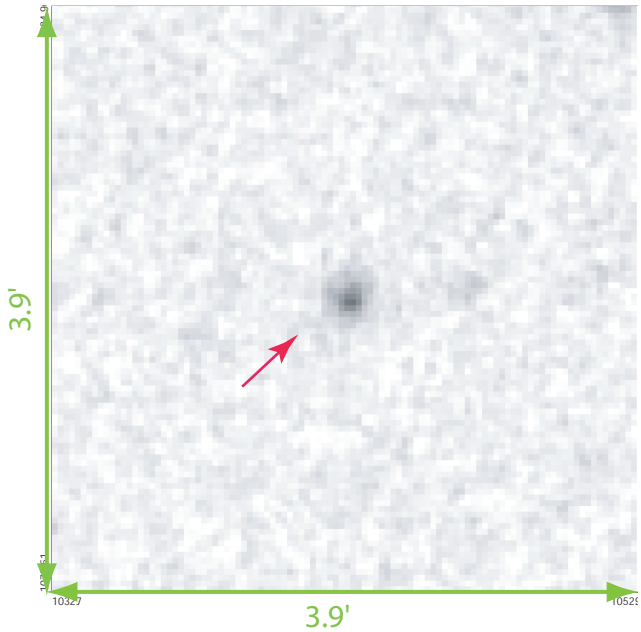

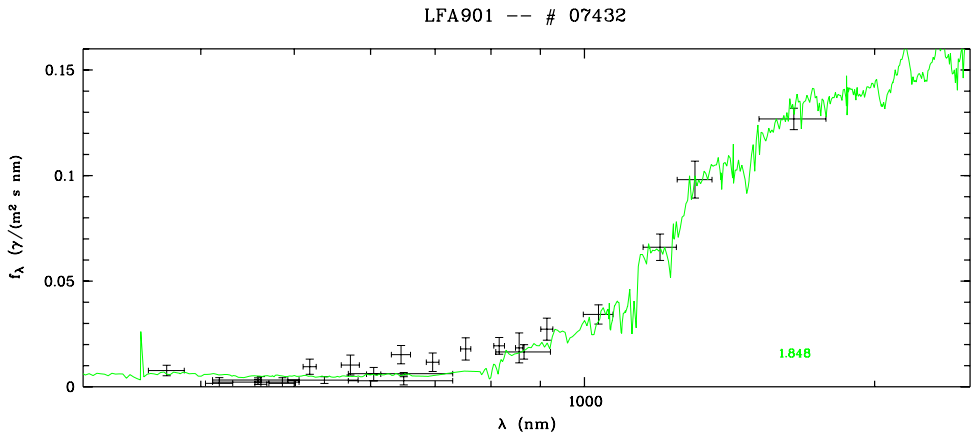

H = 19.72 x / y = 1042.98 / 1083.64

z = 1.848 +/- 0.068

Figure 7.6: Massive object at z=1.848. Top: Deep H-band image. Bottom: best-fitted SED the photometric data points are shown in black and the template is shown in green. The H-band observed magnitude, the redshift and its error as well as the position in world coordinates are given below the SED.

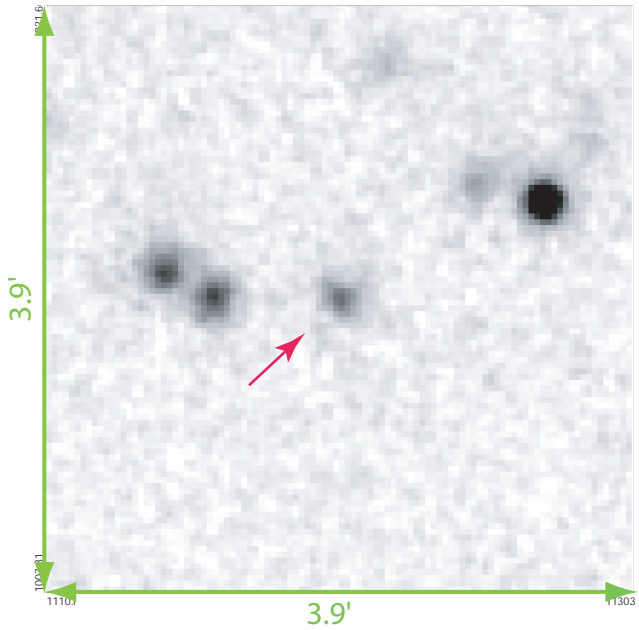

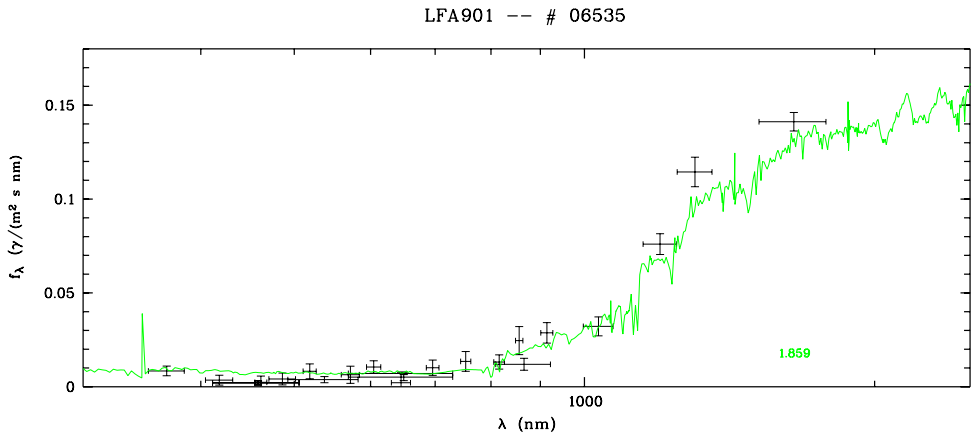

H = 19.61 x / y = 1120.32 / 1017.47

z = 1.859 +/- 0.065

Figure 7.7: Massive object at z=1.859. Top: Deep H-band image. Bottom: best-fitted SED, the photometric data points are shown in black and the template is shown in green. The H-band observed magnitude, the redshift and its error as well as the position in world coordinates are given below the SED.

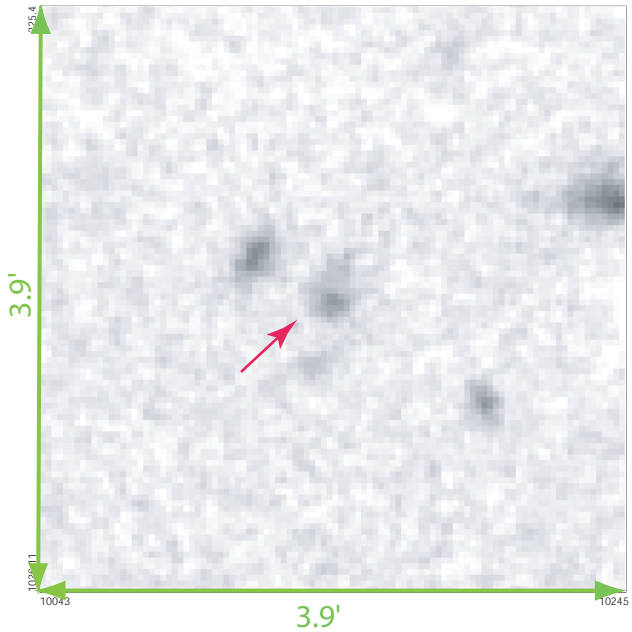

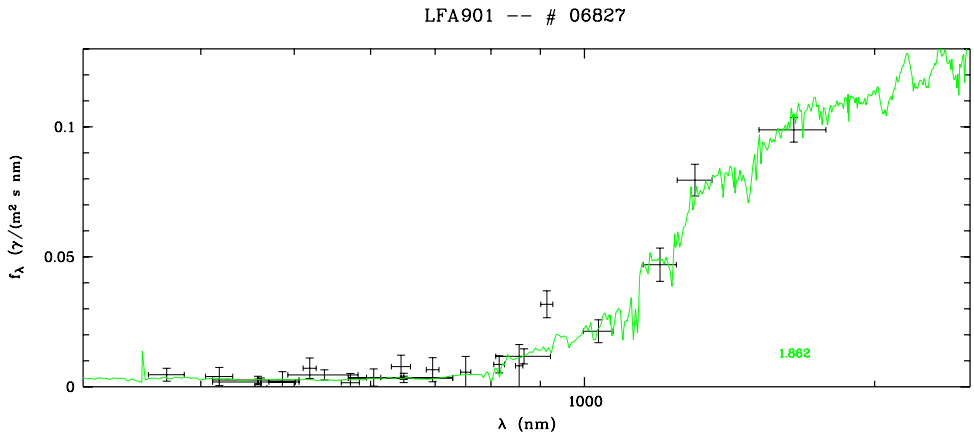

H = 19.99 x / y = 1014.44 / 1036.3

z = 1.862 +/- 0.088

Figure 7.8: Massive object at z=1.862. Top: Deep H-band image. Bottom: best-fitted SED, the photometric data points are shown in black and the template is shown in green. The H-band observed magnitude, the redshift and its error as well as the position in world coordinates are given below the SED.

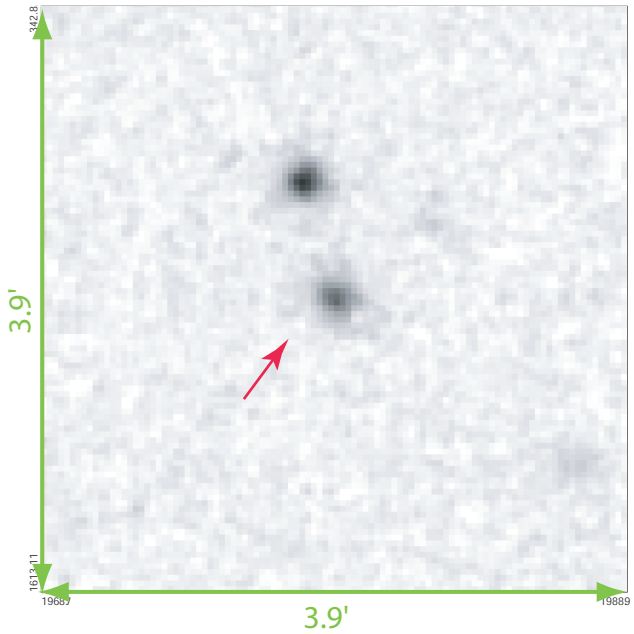

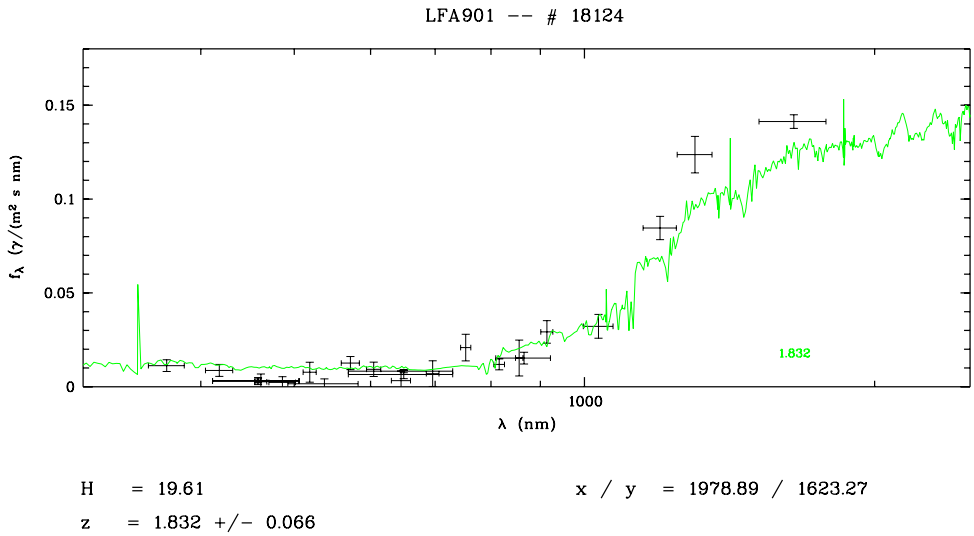

Figure 7.9: Massive object at z=1.832. Top: Deep H-band image. Bottom: best-fitted SED, the photometric data points are shown in black and the template is shown in green. The H-band observed magnitude, the redshift and its error as well as the position in world coordinates are given below the SED.

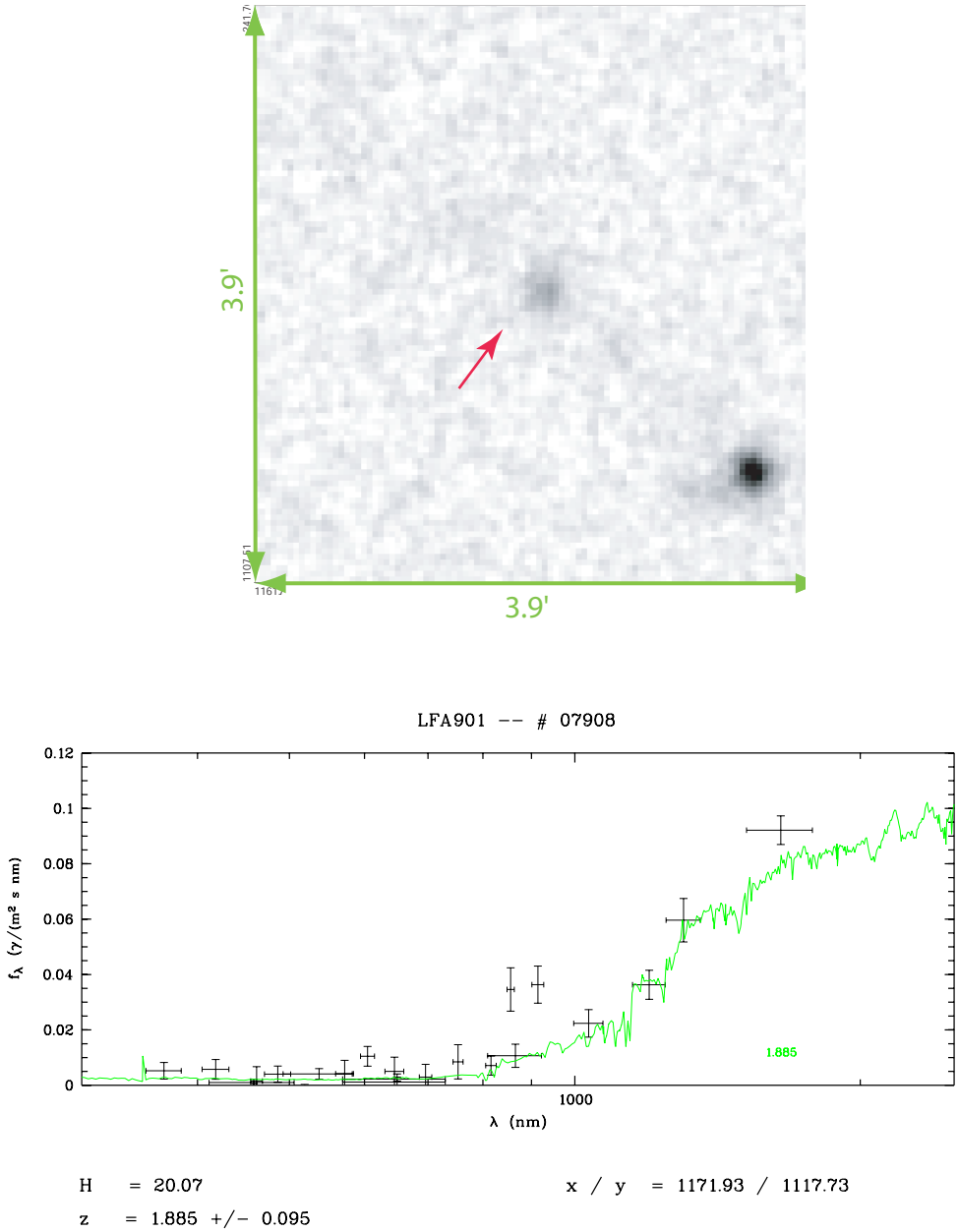

Figure 7.10: Massive object at z=1.885. Top: Deep H-band image. Bottom: best-fitted SED, the photometric data points are shown in black and the template is shown in green. The H-band observed magnitude, the redshift and its error as well as the position in world coordinates are given below the SED.

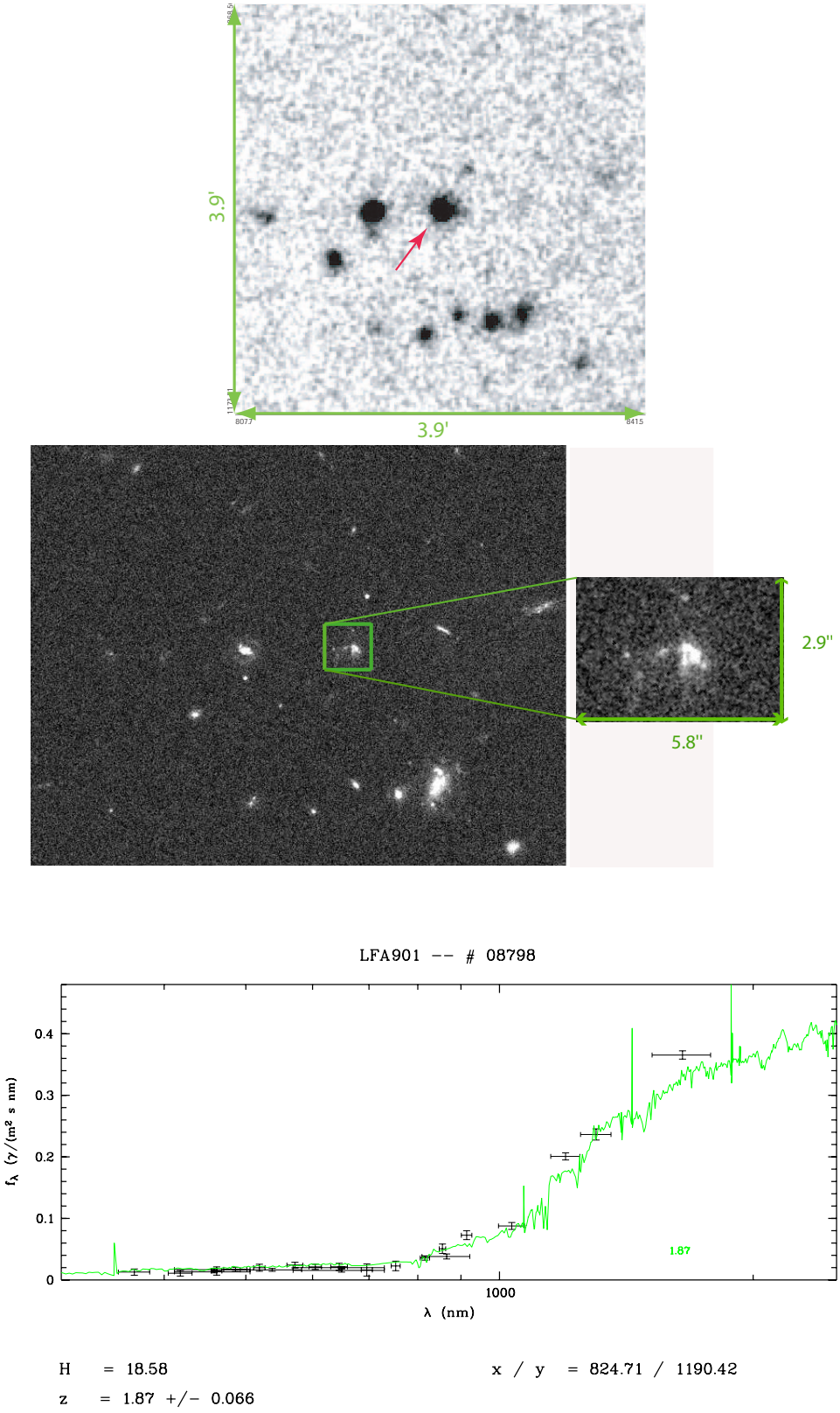

Figure 7.11: The most massive object found in our galaxy sample for the A901-field. Top: H-band image. Middle: Rest-frame UV image at λ_{rest} = 211nm taken with ACS on the Hubble Space Telescope (scale: 8.3 kpc/arcsec). Bottom: Best fitted SED template. The observed H-band magnitude, the redshift and its error and the position of the object in world coordinates are given below the SED.

Summary & Conclusion

This thesis aimed at investigating how the red evolved galaxy and the blue star-forming galaxy populations have evolved in terms of luminosity and mass in the last 10 Gyr of the age of the Universe. To this end the optical COMBO-17 survey data set has been supplemented by NIR observations giving birth to the deep NIR COMBO-17+4 survey in order to access the high redshift Universe up to z=2. The COMBO-17+4 survey targets the three independent fields A901, A226 and S11 but due to repetitive bad weather only the NIR observations for 3/4 of the A901-field were available for this study. Nevertheless, the A901-field is an ideal target to probe galaxy evolution since it contains, in addition to the numerous field galaxies, the super cluster A901/A902 centred at z=0.165.

In the frame of this thesis the data reduction of the NIR observations for more than 1300 images in the Y, J1, J2 and H bands has been performed in order to obtain high quality images from which the photometry then has been derived. The deep H-band observations collected for the A901-field allowed us to reach a $5-\sigma$ detection limit down to H=21.7 mag and a deep H-band catalogue of 14286 galaxies has been derived. This galaxy sample has been used to investigate the bimodality of galaxies at high redshift. A new robust tool has been developed to overcome the difficulty of identifying a clear red sequence in colour-magnitude diagrams due to the large uncertainties in the colour determination for high redshift galaxies. The error weighted histograms allowed us to demonstrate that the galaxy bimodality clearly persists up to z=1.6. Due to the small volume surveyed of only 0.2 square degree and the low number of objects in the A901-field above z$\sim$1.6, we were not able to see a clear red sequence beyond z=1.6. Our investigation of the galaxy bimodality led to surprising results since we found out that, in contrary to the common thought, not all regions of the Universe out to $z = 1$ show signs of a red sequence. In some under-dense regions the red galaxies are missing.

Based on galaxy bimodality seen in several error weighted histograms in different redshift slices of the Universe, we have found that the average U-V colour of the red sequence (at M_V= -20) can well be described as a linear function of lookback time. Such a relation has never been realized before due to the large uncertainties in the red sequence position in previous studies and might open up a new way of understanding how the red sequence is built-up. In order to separate the blue star-forming from the red evolved galaxies a redshift evolving colour-magnitude relation has been derived. Accordingly, we extracted the red galaxies from our

catalogue and obtained a sample of 4640 red galaxies between 0<z<2 and an unprecedented large sample of 1122 red galaxies between 1<z<2 down to an observed magnitude of 21.7 mag in the H-band.

The B-band luminosity function for red and blue galaxies was established for different redshift slices of the Universe in order to study how the luminosity of both galaxy populations have evolved since z=2. Our results show that both galaxy populations have dimmed considerably in the last 10 Gyrs. The characteristic absolute magnitude M_B^* of the red and blue galaxy populations have dimmed respectively by ∼1.7 mag and ∼1.2 mag in the B-band between 2>z>0.2. Our results show that between 1.9>z>1 the red galaxy population has dimmed by ∼1.2 mag while the blue galaxy population has dimmed by ∼0.7 mag, however the incompleteness of our sample above z∼1.3 has lead us to consider our results as first hints only. Also, due to the small volume surveyed our results are affected by cosmic variance and prevent us from viewing our results as a cosmic average of the Universe.

In this thesis the evolution of the red and the blue galaxy populations' masses through cosmic time was also investigated. Mass functions for both galaxy populations in different redshift slices were derived. Our results show that the massive end of the mass function is dominated by red evolved galaxies at z<1 and above z=1 both red evolved and blue star forming galaxy populations contribute in similar numbers to the massive end of the mass function. However, due to the small volume surveyed the low mass end of the mass function for both galaxy populations begins to be incomplete in the still rising part of the distribution. Nevertheless, the mass function in our higher redshift bin between 1.78<z<2 reveals the presence of very massive red galaxies, showing that massive red galaxies are already in place at z∼1.8. As a conclusion, this thesis shows the potential of the COMBO-17+4 photometric survey with only 3/4 of one field surveyed. Even though our results are sensitive to the large scale structures we could demonstrate that photometric redshift is a working tool to study galaxy evolution by supplying a large sample of high redshift galaxies with accurate redshift in order to investigate galaxy bimodality as well as the evolution in luminosity and mass for different galaxy populations.

The future is promising for the COMBO-17+4 survey since NIR observations from two other fields A226 and S11 will soon be added to the A901-field. This will considerably reduce the cosmic variance which has greatly affected our results. Moreover, by combining all the sources from the different fields a catalogue on the order of ∼50000 galaxies between 0<z<2 will be derived from which an unparalleled catalogue of ∼12000 galaxies above z=1 will be obtained. Thus, it will be possible to better estimate the luminosity and mass function above z∼1.6 since the sample will contain much more objects which will further allow us to better quantify the galaxy mass assembly occurring in the transitional z<2 epoch of the Universe. Additionally, the new NIR multi-object spectrograph at the Large Binocular Telescope will provide a unique opportunity to perform spectroscopic follow-up of distant high redshift objects such as the ones identified in this study and reveal their nature.

Appendix A

Standard Stars SED

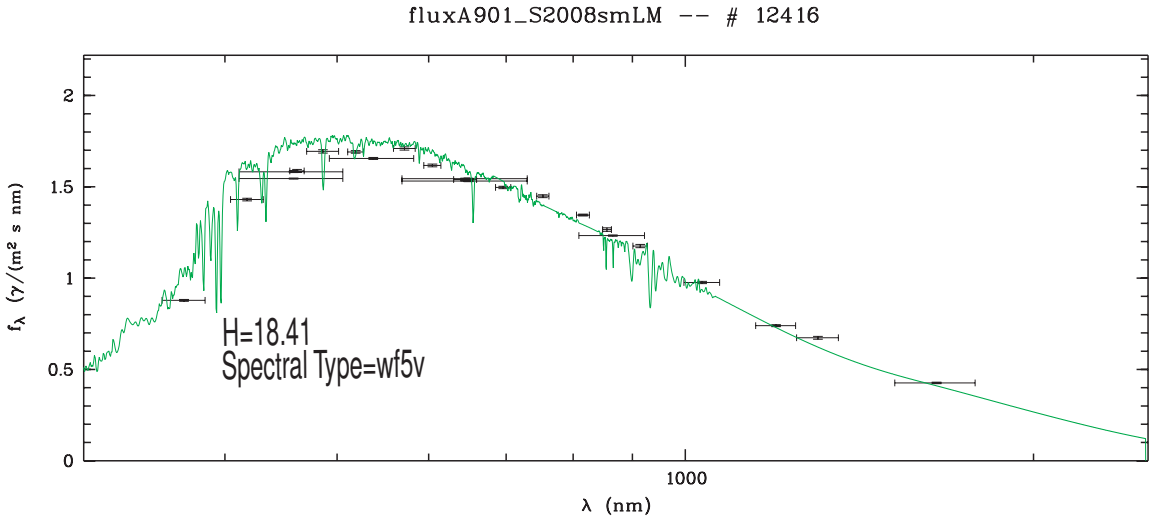
fluxA901_S2008smLM -- # 12416
H=18.41
Spectral Type=wf5v
f_λ (γ/(m² s nm))
λ (nm)
0
0.5
1
1.5
2
1000

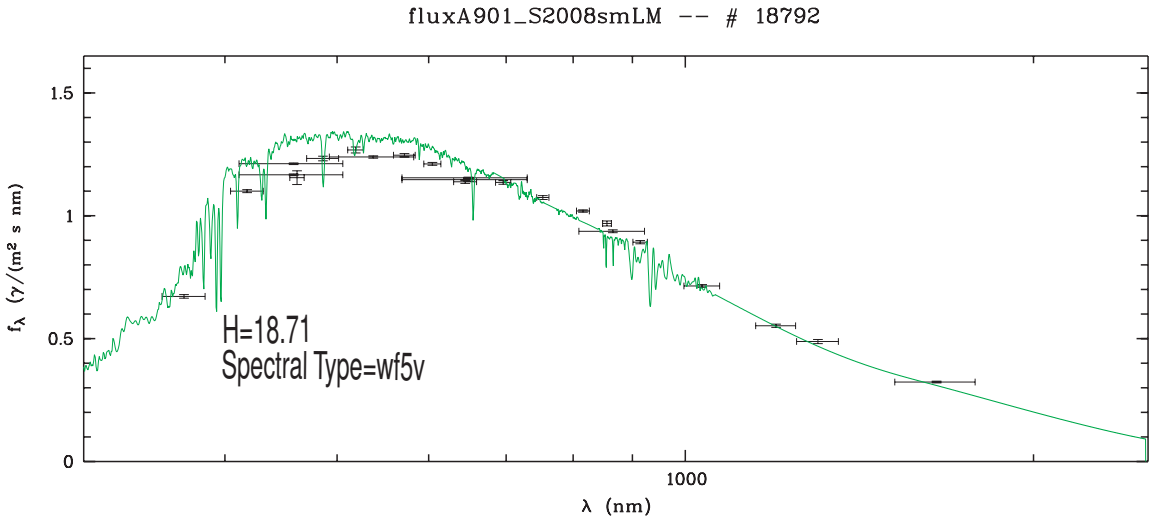
fluxA901_S2008smLM -- # 18792
H=18.71
Spectral Type=wf5v
f_λ (γ/(m² s nm))
λ (nm)
0
0.5
1
1.5
1000

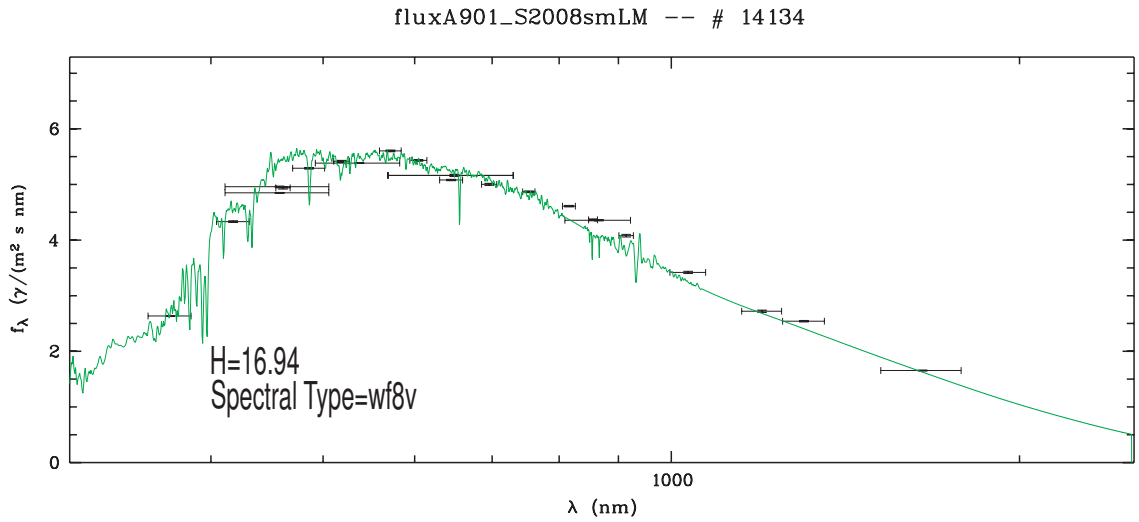
fluxA901_S2008smLM -- # 14134
H=16.94
Spectral Type=wf8v
f_λ (γ/(m² s nm))
λ (nm)
0
2
4
6
1000

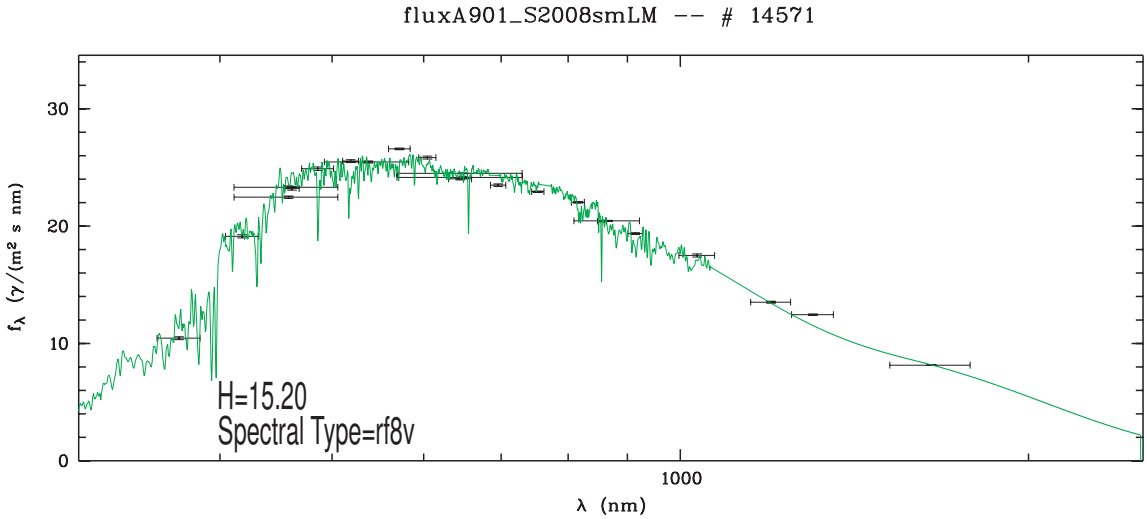
fluxA901_S2008smLM -- # 14571
H=15.20
Spectral Type=rf8v
λ (nm)
1000

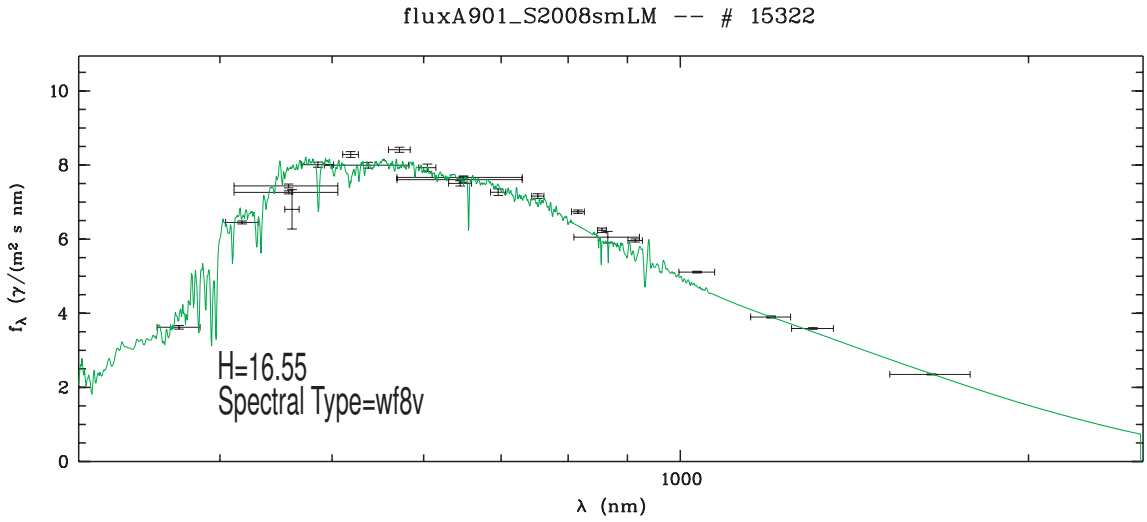
fluxA901_S2008smLM -- # 15322
H=16.55
Spectral Type=wf8v
λ (nm)
1000

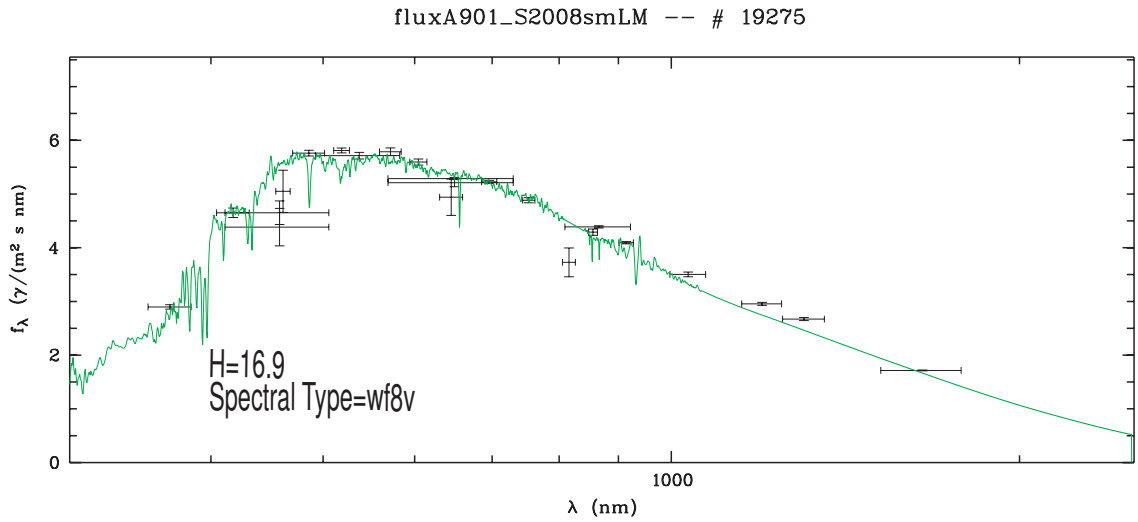
fluxA901_S2008smLM -- # 19275
H=16.9
Spectral Type=wf8v
λ (nm)
1000

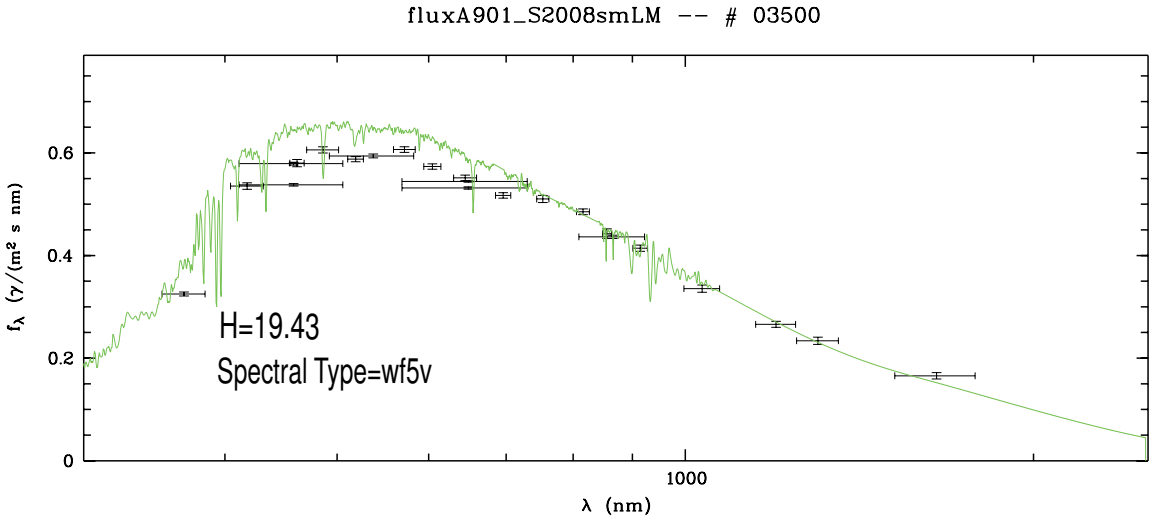
fluxA901_S2008smLM -- # 03500
0.6
0.4
0.2
0
1000
λ (nm)
f_λ (γ/(m² s nm))
H=19.43
Spectral Type=wf5v

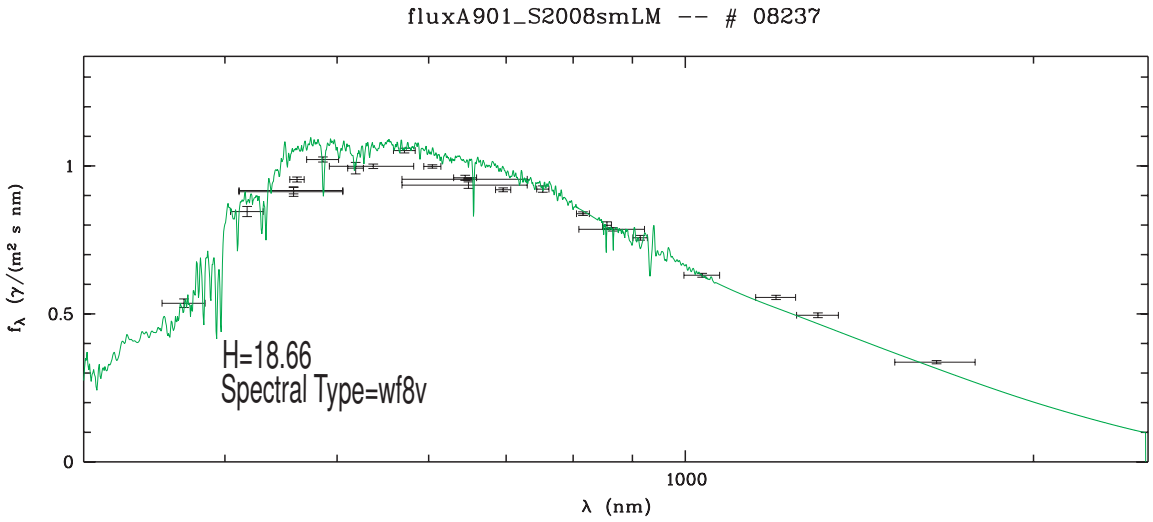
fluxA901_S2008smLM -- # 08237
1
0.5
0
1000
λ (nm)
f_λ (γ/(m² s nm))
H=18.66
Spectral Type=wf8v

Appendix B

Photometry Setup File

Setup file used to perform the photometry with EVALUATE routine from MPIAPHOT.

0	2	1				>	(TEST,CLEAN,POL),FIX_PSF,EFF_PSF
22	0	0.00	2.27	0.00	0.	>	SUM:(W_SUM,SUM),-,APERT, PSF: SX,SY,AL
0	20	1.00	0.0000			>	FIT:(yes/no),ITER,CHI_LIM,SATUR/1000.
1	21	3.00	0.0000			>	BACK:(FIT,L,HST),HW,S_LOC,B_OFF/1000.
1	2	1.30	4.00	0.00		>	PROF:(DIRT,EDGE),R_MIN, X,S_DIRT, -
11	20	3	0.00	0.00		>	MAXI:(FIX,FILT),ITER,RAD,X0,Y0, -

Bibliography

Arnouts, S., Walcher, C. J., Le Fèvre, O., Zamorani, G., Ilbert, O., Le Brun, V., Pozzetti, L., Bardelli, S., Tresse, L., Zucca, E., Charlot, S., Lamareille, F., McCracken, H. J., Bolzonella, M., Iovino, A., Lonsdale, C., Polletta, M., Surace, J., Bottini, D., Garilli, B., Maccagni, D., Picat, J. P., Scaramella, R., Scodeggio, M., Vettolani, G., Zanichelli, A., Adami, C., Cappi, A., Ciliegi, P., Contini, T., de la Torre, S., Foucaud, S., Franzetti, P., Gavignaud, I., Guzzo, L., Marano, B., Marinoni, C., Mazure, A., Meneux, B., Merighi, R., Paltani, S., Pellò, R., Pollo, A., Radovich, M., Temporin, S., & Vergani, D. 2007, A&A, 476, 137

Baumeister, H., Bizenberger, P., Bayler-Jones, C. A. L., Kovács, Z., Röser, H.-J., & Rohloff, R.-R. 2003, in Society of Photo-Optical Instrumentation Engineers (SPIE) Conference Series, Vol. 4841, Society of Photo-Optical Instrumentation Engineers (SPIE) Conference Series, ed. M. Iye & A. F. M. Moorwood, 343–354

Bell, E. F., McIntosh, D. H., Barden, M., Wolf, C., Caldwell, J. A. R., Rix, H.-W., Beckwith, S. V. W., Borch, A., Häussler, B., Jahnke, K., Jogee, S., Meisenheimer, K., Peng, C., Sanchez, S. F., Somerville, R. S., & Wisotzki, L. 2004a, ApJ, 600, L11

Bell, E. F., Wolf, C., Meisenheimer, K., Rix, H.-W., Borch, A., Dye, S., Kleinheinrich, M., Wisotzki, L., & McIntosh, D. H. 2004b, ApJ, 608, 752

Bertin, E. & Arnouts, S. 1996, A&AS, 117, 393

Binney, J. & Merrifield, M. 1998, Galactic astronomy (Galactic astronomy / James Binney and Michael Merrifield. Princeton, NJ : Princeton University Press, 1998. (Princeton series in astrophysics) QB857 .B522 1998 ($35.00))

Borch, A., Meisenheimer, K., Bell, E. F., Rix, H.-W., Wolf, C., Dye, S., Kleinheinrich, M., Kovacs, Z., & Wisotzki, L. 2006, A&A, 453, 869

Cassata, P., Cimatti, A., Kurk, J., Rodighiero, G., Pozzetti, L., Bolzonella, M., Daddi, E., Mignoli, M., Berta, S., Dickinson, M., Franceschini, A., Halliday, C., Renzini, A., Rosati, P., & Zamorani, G. 2008, A&A, 483, L39

Cirasuolo, M., McLure, R. J., Dunlop, J. S., Almaini, O., Foucaud, S., Smail, I., Sekiguchi, K., Simpson, C., Eales, S., Dye, S., Watson, M. G., Page, M. J., & Hirst, P. 2007, MNRAS, 380, 585

Cox, A. N. 2000, S&T, 100, 010000

Daddi, E., Dickinson, M., Chary, R., Pope, A., Morrison, G., Alexander, D. M., Bauer, F. E., Brandt, W. N., Giavalisco, M., Ferguson, H., Lee, K.-S., Lehmer, B. D., Papovich, C., & Renzini, A. 2005, ApJ, 631, L13

Faber, S. M., Willmer, C. N. A., Wolf, C., Koo, D. C., Weiner, B. J., Newman, J. A., Im, M., Coil, A. L., Conroy, C., Cooper, M. C., Davis, M., Finkbeiner, D. P., Gerke, B. F., Gebhardt, K., Groth, E. J., Guhathakurta, P., Harker, J., Kaiser, N., Kassin, S., Kleinheinrich, M., Konidaris, N. P., Kron, R. G., Lin, L., Luppino, G., Madgwick, D. S., Meisenheimer, K., Noeske, K. G., Phillips, A. C., Sarajedini, V. L., Schiavon, R. P., Simard, L., Szalay, A. S., Vogt, N. P., & Yan, R. 2007, ApJ, 665, 265

Fassbender, R. 2003, Diploma. Thesis, University of Heidelberg

Fioc, M. & Rocca-Volmerange, B. 1997, A&A, 326, 950

Franzetti, P., Scodeggio, M., Maccagni, D., Garilli, B., & the VVDS collaboration. 2006, Memorie della Societa Astronomica Italiana Supplement, 9, 297

Gabasch, A. 2004, PhD thesis, Galaxy Evolution in the Fors Deep Field.

Gray, M. E., Wolf, C., Barden, M., Peng, C. Y., Häußler, B., Bell, E. F., McIntosh, D. H., Guo, Y., Caldwell, J. A. R., Bacon, D., Balogh, M., Barazza, F. D., Böhm, A., Heymans, C., Jahnke, K., Jogee, S., van Kampen, E., Lane, K., Meisenheimer, K., Sánchez, S. F., Taylor, A., Wisotzki, L., Zheng, X., Green, D. A., Beswick, R. J., Saikia, D. J., Gilmour, R., Johnson, B. D., & Papovich, C. 2009, MNRAS, 393, 1275

Herbst, T. M. 1994, PASP, 106, 1298

Hinshaw, G., Weiland, J. L., Hill, R. S., Odegard, N., Larson, D., Bennett, C. L., Dunkley, J., Gold, B., Greason, M. R., Jarosik, N., Komatsu, E., Nolta, M. R., Page, L., Spergel, D. N., Wollack, E., Halpern, M., Kogut, A., Limon, M., Meyer, S. S., Tucker, G. S., & Wright, E. L. 2008, ArXiv e-prints

Hippelein, H., Maier, C., Meisenheimer, K., Wolf, C., Fried, J. W., von Kuhlmann, B., Kümmel, M., Phleps, S., & Röser, H.-J. 2003, A&A, 402, 65

Hogg, D. W. 1999, ArXiv Astrophysics e-prints

Hopkins, A. M. 2004, ApJ, 615, 209

Ilbert, O., Tresse, L., Zucca, E., Bardelli, S., Arnouts, S., Zamorani, G., Pozzetti, L., Bottini, D., Garilli, B., Le Brun, V., Le Fèvre, O., Maccagni, D., Picat, J.-P., Scaramella, R., Scodeggio, M., Vettolani, G., Zanichelli, A., Adami, C., Arnaboldi, M., Bolzonella, M., Cappi, A., Charlot, S., Contini, T., Foucaud, S., Franzetti, P., Gavignaud, I., Guzzo, L., Iovino, A., McCracken, H. J., Marano, B., Marinoni, C., Mathez, G., Mazure, A., Meneux, B., Merighi, R., Paltani, S., Pello, R., Pollo, A., Radovich, M., Bondi, M., Bongiorno, A., Busarello, G., Ciliegi, P., Lamareille, F., Mellier, Y., Merluzzi, P., Ripepi, V., & Rizzo, D. 2005, A&A, 439, 863

Kovács, Z. 2006, PhD thesis, PhD Thesis, Combined Faculties for the Natural Sciences and for Mathematics of the University of Heidelberg, Germany. 167 pp. (2006)

Kriek, M., van der Wel, A., van Dokkum, P. G., Franx, M., & Illingworth, G. D. 2008, ApJ, 682, 896

Lilly, S. J., Le Fevre, O., Hammer, F., & Crampton, D. 1996, ApJ, 460, L1+

Lupton, R. H., Gunn, J. E., & Szalay, A. S. 1999, AJ, 118, 1406

Madau, P., Ferguson, H. C., Dickinson, M. E., Giavalisco, M., Steidel, C. C., & Fruchter, A. 1996, MNRAS, 283, 1388

McGrath, E. J., Stockton, A., & Canalizo, G. 2007, ApJ, 669, 241

Meisenheimer, K., Beckwith, S., Fockenbrock, H., Fried, J., Hippelein, H., Huang, J., Leinert, C., Phleps, S., Roser, H.-J., Thommes, E., Thompson, D., Wolf, C., & Chaffee, F. 1998, in Astronomical Society of the Pacific Conference Series, Vol. 146, The Young Universe: Galaxy Formation and Evolution at Intermediate and High Redshift, ed. S. D'Odorico, A. Fontana, & E. Giallongo, 134–+

Meisenheimer, K., Wolf, C., & Nicol, M.-H. in prep 2009

Oke, J. B. 1990, AJ, 99, 1621

Pei, Y. C. 1992, ApJ, 395, 130

Pickles, A. J. 1998, PASP, 110, 863

Röser, H.-J. 2006, MPIA

Röser, H.-J. & Meisenheimer, K. 1991, A&A, 252, 458

Sánchez, S. F., Thiele, U., Aceituno, J., Cristobal, D., Perea, J., & Alves, J. 2008, PASP, 120, 1244

Sandage, A., Tammann, G. A., & Yahil, A. 1979, ApJ, 232, 352

Schmidt, M. 1968, ApJ, 151, 393

Springel, V., White, S. D. M., Jenkins, A., Frenk, C. S., Yoshida, N., Gao, L., Navarro, J., Thacker, R., Croton, D., Helly, J., Peacock, J. A., Cole, S., Thomas, P., Couchman, H., Evrard, A., Colberg, J., & Pearce, F. 2005, Nature, 435, 629

Strateva, I., Ivezić, Ž., Knapp, G. R., Narayanan, V. K., Strauss, M. A., Gunn, J. E., Lupton, R. H., Schlegel, D., Bahcall, N. A., Brinkmann, J., Brunner, R. J., Budavári, T., Csabai, I., Castander, F. J., Doi, M., Fukugita, M., Győry, Z., Hamabe, M., Hennessy, G., Ichikawa, T., Kunszt, P. Z., Lamb, D. Q., McKay, T. A., Okamura, S., Racusin, J., Sekiguchi, M., Schneider, D. P., Shimasaku, K., & York, D. 2001, AJ, 122, 1861

Taylor, E. N., Franx, M., van Dokkum, P. G., Bell, E. F., Brammer, G. B., Rudnick, G., Wuyts, S., Gawiser, E., Lira, P., Urry, C., & Rix, H.-W. 2008, ArXiv e-prints

Tody, D. 1993, in Astronomical Society of the Pacific Conference Series, Vol. 52, Astronomical Data Analysis Software and Systems II, ed. R. J. Hanisch, R. J. V. Brissenden, & J. Barnes, 173–+

Vanden Berk, D. E., Richards, G. T., Bauer, A., Strauss, M. A., Schneider, D. P., Heckman, T. M., York, D. G., Hall, P. B., Fan, X., Knapp, G. R., Anderson, S. F., Annis, J., Bahcall, N. A., Bernardi, M., Briggs, J. W., Brinkmann, J., Brunner, R., Burles, S., Carey, L., Castander, F. J., Connolly, A. J., Crocker, J. H., Csabai, I., Doi, M., Finkbeiner, D., Friedman, S., Frieman, J. A., Fukugita, M., Gunn, J. E., Hennessy, G. S., Ivezić, Ž., Kent, S., Kunszt, P. Z., Lamb, D. Q., Leger, R. F., Long, D. C., Loveday, J., Lupton, R. H., Meiksin, A., Merelli, A., Munn, J. A., Newberg, H. J., Newcomb, M., Nichol, R. C., Owen, R., Pier, J. R., Pope, A., Rockosi, C. M., Schlegel, D. J., Siegmund, W. A., Smee, S., Snir, Y., Stoughton, C., Stubbs, C., SubbaRao, M., Szalay, A. S., Szokoly, G. P., Tremonti, C., Uomoto, A., Waddell, P., Yanny, B., & Zheng, W. 2001, AJ, 122, 549

Vergani, D., Scodeggio, M., Pozzetti, L., Iovino, A., Franzetti, P., Garilli, B., Zamorani, G., Maccagni, D., Lamareille, F., Le Fèvre, O., Charlot, S., Contini, T., Guzzo, L., Bottini, D., Le Brun, V., Picat, J. P., Scaramella, R., Tresse, L., Vettolani, G., Zanichelli, A., Adami, C., Arnouts, S., Bardelli, S., Bolzonella, M., Cappi, A., Ciliegi, P., Foucaud, S., Gavignaud, I., Ilbert, O., McCracken, H. J., Marano, B., Marinoni, C., Mazure, A., Meneux, B., Merighi, R., Paltani, S., Pellò, R., Pollo, A., Radovich, M., Zucca, E., Bondi, M., Bongiorno, A., Brinchmann, J., Cucciati, O., de la Torre, S., Gregorini, L., Perez-Montero, E., Mellier, Y., Merluzzi, P., & Temporin, S. 2008, A&A, 487, 89

Weiner, B. J., Phillips, A. C., Faber, S. M., Willmer, C. N. A., Vogt, N. P., Simard, L., Gebhardt, K., Im, M., Koo, D. C., Sarajedini, V. L., Wu, K. L., Forbes, D. A., Gronwall, C., Groth, E. J., Illingworth, G. D., Kron, R. G., Rhodes, J., Szalay, A. S., & Takamiya, M. 2005, ApJ, 620, 595

Williams, R. J., Quadri, R. F., Franx, M., van Dokkum, P., & Labbe, I. 2008, ArXiv e-prints

Willmer, C. N. A. 1997, AJ, 114, 898

Wolf, C. 1998, PhD thesis, A Multicolor Classification in CADIS and the Search for Quasars.

Wolf, C., Gray, M. E., & Meisenheimer, K. 2005, A&A, 443, 435

Wolf, C., Meisenheimer, K., Kleinheinrich, M., Borch, A., Dye, S., Gray, M., Wisotzki, L., Bell, E. F., Rix, H.-W., Cimatti, A., Hasinger, G., & Szokoly, G. 2004, A&A, 421, 913

Wolf, C., Meisenheimer, K., Rix, H.-W., Borch, A., Dye, S., & Kleinheinrich, M. 2003, A&A, 401, 73

Wolf, C., Meisenheimer, K., & Röser, H.-J. 2001a, A&A, 365, 660

Wolf, C., Meisenheimer, K., Röser, H.-J., Beckwith, S. V. W., Chaffee, Jr., F. H., Fried, J., Hippelein, H., Huang, J.-S., Kümmel, M., von Kuhlmann, B., Maier, C., Phleps, S., Rix, H.-W., Thommes, E., & Thompson, D. 2001b, A&A, 365, 681

Zatloukal, M. 2008, PhD thesis, A search for distant clusters of galaxies in the COSMOS field.